RADIATION-DRIVEN, GEOMETRICALLY THICK, DUSTY OBSCURATION IN ACTIVE GALACTIC NUCLEI

by
Chi-Ho Chan

A dissertation submitted to the Johns Hopkins University
in conformity with the requirements for the degree of
Doctor of Philosophy

Baltimore, Maryland
October, 2016

Abstract

Substantial evidence points to dusty, geometrically thick tori obscuring the central engines of active galactic nuclei (AGNs), but so far no mechanism satisfactorily explains why cool dust in the torus remains in a puffy geometry. Near-Eddington infrared (IR) and ultraviolet (UV) luminosities coupled with high dust opacities at these frequencies suggest that radiation pressure on dust can play a significant role in shaping the torus. Here we explore this possibility with three-dimensional radiative magnetohydrodynamics simulations. Our code simultaneously solves the hydrodynamics equations, the time-dependent multi–angle group IR radiative transfer (RT) equation, and the time-independent UV RT equation. We find a highly dynamic situation. IR radiation is anisotropic, leaving primarily through the central hole. Since IR and UV radiative accelerations increase with latitude, our torus naturally settles into a steady state with inflow along the mid-plane and outflow near the inner surface. The covering fraction and column density distribution of our torus are stable over time and roughly agree with observations. The outflow has speed and mass loss rate close to observed values. Most importantly, our simulations demonstrate that isolated tori cannot exist indefinitely because outflow removes mass and radiative acceleration removes binding energy; this means realistic tori are determined by the rate of mass resupply from galactic scales, as well as stresses both internal to the tori and in the outflow.

Thesis Advisor	Professor Julian H. Krolik, Johns Hopkins University
Defense Committee Member	Professor Ethan T. Vishniac, Johns Hopkins University
Defense Committee Member	Professor Nadia L. Zakamska, Johns Hopkins University
Defense Committee Member	Doctor Timothy R. Kallman, NASA Goddard Space Flight Center
Defense Committee Member	Professor Shane W. Davis, University of Virginia

今天我　寒夜裏看雪飄過
懷着冷卻了的心窩飄遠方
風雨裏追趕　霧裏分不清影蹤
天空海闊你與我　可會變（誰沒在變）

多少次　迎着冷眼與嘲笑
從沒有放棄過心中的理想
一剎那恍惚　若有所失的感覺
不知不覺已變淡　心裏愛（誰明白我）

原諒我這一生不羈放縱愛自由
也會怕有一天會跌倒
背棄了理想　誰人都可以
那會怕有一天只你共我

仍然自由自我
永遠高唱我歌　走遍千里

Beyond，海闊天空

Author's note

Parts of Chapter 1, Chapter 2, and Chapter 3 have already been published in Chan & Krolik (2016). Chapters 4 and 5 contain material that will be included in a forthcoming paper.

The simulations were performed on the Johns Hopkins Homewood High-Performance Cluster and Maryland Advanced Research Computing Center.

Acknowledgments

> "It's just the same story as a doctor once told me," observed the elder. "He was a man getting on in years, and undoubtedly clever. He spoke as frankly as you, though in jest, in bitter jest. 'I love humanity,' he said, 'but I wonder at myself. The more I love humanity in general, the less I love man in particular. In my dreams,' he said, 'I have often come to making enthusiastic schemes for the service of humanity, and perhaps I might actually have faced crucifixion if it had been suddenly necessary; and yet I am incapable of living in the same room with anyone for two days together, as I know by experience. As soon as anyone is near me, his personality disturbs my self-complacency and restricts my freedom. In twenty-four hours I begin to hate the best of men: one because he's too long over his dinner; another because he has a cold and keeps on blowing his nose. I become hostile to people the moment they come close to me. But it has always happened that the more I detest men individually the more ardent becomes my love for humanity.'"
>
> Fyodor Dostoyevsky, *The Brothers Karamazov*

It would be extreme hubris on my part to dedicate this dissertation to humanity. This work is limited, flawed, feigning to be a genuine contribution to the collective knowledge of a once-proud species, which, in recent years, has been revealed to be equally limited and flawed. Everything written in the following pages will be forgotten in time, deemed unfashionable or outright untrue; but as of now, as of this very moment, this dissertation is the world to me, the excuse for my continued existence. I would not be writing these words were it not for the many kind souls who have helped me throughout my life, so I would like to express my gratitude to each one of them personally.

I am forever indebted to my advisor, Julian Krolik, for his steady hand in guiding me through these seven years of graduate school. My younger self did not imagine research would entail so many ambiguities and uncertainties, especially when working with something as deterministic as simulations: the code is not guaranteed correct beyond a handful test cases; concessions must be made to cope with hardware limitations; and the parameter space can only be sparsely sampled. In times of doubt, Julian would remind me that we are always probing a tiny corner of reality at a time, and it is only through incremental effort that we get a feeling of the overall picture. While combing through simulation results, desperately chasing down that one clever conclusion, it is tempting to make unwarranted assumptions that would transform the results into something

more interpretable and palatable. In such event, Julian would disabuse me of my preconceived notions and force me to justify every argument. His insistence on rigor is what I continually strive toward.

This work rests on the simulation code Athena and its radiative transfer module, which are written by Jim Stone, Yanfei Jiang, Shane Davis, Aaron Skinner, and many other collaborators. The authors have generously allowed this wonderful code to be used for this project; the fantastic results I am about to report could not have been obtained otherwise. The code was already in functional form when I started working on it; all I did was fixing several bugs and adapting the code to my problem.

I am fortunate that my parents are relatively hands-off toward my education. They have never pressured me to learn an instrument or to join a school team. They have never questioned my decision to major in physics or to pursue graduate studies abroad. If they were more meddling, I might have stayed in Hong Kong, made decent headway in a saner career as a physician, a lawyer, or a banker, and mastered playing the piano. Seeing how I am constantly worried about what to do with myself, their trust in me is entirely unwarranted.

My elder aunt have had immense influence on me from a young age. In kindergarten, I had to practice writing Chinese characters; when I made a mistake with a stroke, she would erase the entire character and force me to start from scratch. In primary school, I was often bored out of my mind after I was done with assignments; she would take me out to the public library for the afternoon. Little did she know at the time that an obsession for excellence and a habit of reading would go a long way.

My grandmother took care of me since I was born: she woke me up in the morning; she cooked for me; she washed me; she took me to school and picked me up after. When I switched to an all-English curriculum and could not catch up, my younger aunt helped me revise and found story books to help me with my reading. The fact that I was able to achieve anything at school is due in no small part to their efforts.

Graduate school was certainly no smooth ride. Ming-Chung Chu, Rosemary Wyse, and Eric Rose were there to hear me out when everything was coming apart at the seams, when I utterly questioned my beliefs and my decisions, when even I could not bear looking at myself. Their reassuring yet firm words gave me the strength to pick up the pieces and move forward. A special shout-out goes to Nadia Zakamska for her understanding and unwavering belief despite everything to the contrary, for invariably sensing if something was amiss, and for going out of her way to bring me comfort and confidence. The world gets ever colder, but a little touch of kindness, a little reassurance of hope, is already to me that clean, well-lighted place.

Roseanne Cheng and I share a sense of companionship in our similar struggles in academia and in coding. I especially appreciate how she, being much more sociable than I am, goes to great lengths to drag me out to meet people, something I have long since given up trying.

This dissertation is typeset with TEX, and figures contained herein are created with the Python package `matplotlib`. Despite my interminable complaints about how these systems offend my sensibilities and are

impossible to tweak, I cannot imagine working without them. For this, I thank TEX contributors for modernizing it with new engines and packages, and `matplotlib` contributors for creating a flexible tool that is not too painful to use.

Contents

1 Introduction **1**

1.1 Active galactic nuclei . . . 2

1.2 Dynamics of AGN tori . . . 9

1.3 Theory of accretion disks . . . 13

2 Methods **16**

2.1 Simulation code . . . 16

2.2 Ideal magnetohydrodynamics . . . 18

2.3 Radiative transfer . . . 19

2.3.1 Time-dependent IR radiative transfer . . . 19

2.3.2 Reduced speed of light approximation . . . 19

2.3.3 Improvement to treatment of scattering in Athena . . . 20

2.3.4 Reduction of numerical artifacts in advection of IR radiation in Athena . . . 22

2.3.5 Time-independent long-characteristics UV radiative transfer . . . 23

2.3.6 IR and UV opacities . . . 25

2.4 Simulation setup . . . 25

2.4.1 Central mass and reduced speed of light . . . 25

2.4.2 Normalization . . . 26

2.4.3 Ambient material . . . 27

2.4.4 Boundary conditions and numerical limits . . . 28

3 Radiative hydrodynamic AGN tori **29**

3.1 Simulation setup . . . 29

3.1.1 Initial condition . . . 29

3.1.2 IR initial condition . . . 31

3.1.3 Orbital velocity profile of a hydrostatic, radiation-supported torus . . . 31

3.1.4 Simulation parameters and simulation domain . . . 32
3.2 Results . . . 33
3.2.1 Qualitative description of gas motion . . . 33
3.2.2 Radial perturbation of the torus inner surface . . . 36
3.2.3 Anisotropy of IR radiation . . . 38
3.2.4 Mass, momentum, and kinetic energy loss rates . . . 40
3.3 Discussion . . . 42
3.3.1 Estimation of IR radiation energy density at the torus inner edge . . . 43
3.3.2 Variation of simulation parameters . . . 44
3.3.3 Scaling simulation results to more realistic parameters . . . 45
3.3.4 Balance between radiation-driven mass loss and mass resupply . . . 46
3.3.5 Radial perturbation of the torus inner surface . . . 47
3.4 Summary . . . 48

4 Radiative magnetohydrodynamic AGN tori **50**
4.1 Simulation setup . . . 50
4.1.1 Simulation strategy . . . 50
4.1.1.1 MHD stage . . . 51
4.1.1.2 UV-RMHD stage . . . 52
4.1.1.3 Reduction of angular momentum in UV-RMHD stage . . . 53
4.1.1.4 IR-RMHD stage . . . 54
4.1.2 Scaling properties . . . 55
4.1.3 Simulation parameters and domain . . . 56
4.2 Results . . . 56
4.2.1 Overview of UV-RMHD stage . . . 56
4.2.2 Parameter study of reduction of angular momentum in UV-RMHD stage . . . 59
4.2.3 Overview of IR-RMHD stage . . . 60
4.2.4 Support and gas dynamics in IR-RMHD stage . . . 64
4.2.5 IR radiation and temperature in IR-RMHD stage . . . 68
4.2.6 Magnetic field in IR-RMHD stage . . . 70
4.3 Discussion . . . 72
4.3.1 Observed temperature profiles in IR-RMHD stage . . . 72
4.3.2 X-ray, IR, and UV obscuration in IR-RMHD stage . . . 73

4.3.3 Extrapolating to realistic AGN tori . . . 74
4.3.3.1 Mass loss rate and wind terminal speed . . . 75
4.3.3.2 Morphology . . . 76
4.3.3.3 Temperature . . . 76
4.3.3.4 Obscuration . . . 77
4.3.3.5 Additional physics . . . 77
4.3.4 Comparison with other torus models . . . 78
4.4 Summary . . . 81

5 Conclusions **83**
5.1 Lessons from RHD and RMHD simulations . . . 83
5.1.1 Structure and dynamics of tori under irradiation . . . 84
5.1.2 Physics of tori under irradiation . . . 86
5.1.3 Variation of torus parameters . . . 87
5.1.4 Implications for realistic tori . . . 88
5.2 Future directions . . . 90
5.3 Final remarks . . . 92

Bibliography **93**

List of Tables

2.1 Derived fiducial quantities. 27

List of Figures

1.1 Schematic diagram of the straw person model of the AGN unification picture. 7

3.1 Poloidal plane of the $L_{\rm UV}/L_{\rm E} = 0.11$ and $L_{\rm UV}/L_{\rm E} = 0.14$ simulations, showing gas density and gas momentum density. 34

3.2 Mid-plane of the $L_{\rm UV}/L_{\rm E} = 0.11$, $L_{\rm UV}/L_{\rm E} = 0.12$, and $L_{\rm UV}/L_{\rm E} = 0.13$ simulations, showing gas density and cylindrically radial IR radiative flux. 37

3.3 Poloidal plane of the $L_{\rm UV}/L_{\rm E} = 0.11$ simulation, showing gas and IR temperatures, IR radiative flux, and gas velocity. 39

3.4 IR radiative flux against latitude in the $L_{\rm UV}/L_{\rm E} = 0.11$ simulation. 40

3.5 Mass, spherically radial gas momentum, and kinetic energy loss rates. 42

3.6 Comparison of modeled and simulated IR radiation energy density at the inner edge. 44

4.1 Prescriptions for lowering the angular momentum profile before the UV-RMHD stage, and survival time in the UV-RMHD stage against binding energy at the beginning of the stage. 54

4.2 Poloidal plane in the UV-RMHD and IR-RMHD stages, showing gas density, gas velocity, and the Bernoulli constant. 57

4.3 Schematic diagram of a vertical structure in poloidal section. 58

4.4 Mid-plane specific axial angular momentum profile in run G in the UV-RMHD stage. 60

4.5 Poloidal gas flow in the "steady" state of the IR-RMHD stage. 63

4.6 Ratios of poloidal force components to gravity in the "steady" state of the IR-RMHD stage. . . . 66

4.7 IR radiation energy density and radiative flux against latitude in the "steady" state of the IR-RMHD stage. 68

4.8 Poloidal plane in the IR-RMHD stage, showing gas and IR temperatures, modeled gas temperature inside the central hole, as well as edge-on and face-on IR photospheres. 69

4.9 Poloidal plasma betas in the IR-RMHD stage. 71

4.10 Thomson, IR, and UV optical depths in the IR-RMHD stage against latitude, and histogram of the same in the "steady" state of the IR-RMHD stage over solid angle around the central source. . . . 73
4.11 Gas density along sightlines to the central source of varying latitudes in the IR-RMHD stage. . . 75

CHAPTER 1

INTRODUCTION

> Examining the various parts, one after the other, and trying various ways of considering them, we may be led finally to see the whole result in a different light, and our new conception of the result may suggest a new proof.
> It may be confessed that all this is more likely to happen to an experienced mathematician dealing with some advanced problem than to a beginner struggling with some elementary problem. The mathematician who has a great deal of knowledge is more exposed than the beginner to the danger of mobilizing too much knowledge and framing an unnecessarily involved argument. But, as a compensation the experienced mathematician is in a better position than the beginner to appreciate the reinterpretation of a small part of the result and to proceed, accumulating such small advantages, to recasting ultimately the whole result.
>
> George Pólya, *How to Solve It: A New Aspect of Mathematical Method*

Astrophysics lies at the intersection of all fields of physics and chemistry, pulling together optics, material science, atomic and molecular physics, chemical kinetics, classical mechanics, fluid mechanics, magnetism, plasma physics, relativity, high-energy physics, nuclear physics, and particle physics. The rising importance of computers in modern astrophysics and the immense datasets produced by autonomous observatories require practitioners to be proficient in computer science, numerical algorithms, information processing, and data mining as well. Clearly we cannot hope to provide a comprehensive overview of this ever-growing field, but we should at least attempt to equip the scientifically literate reader with the basic knowledge requisite to understand the matter at hand, which, in the coarsest terms, is the study of fluid motion under the radiative pressure from an active galactic nucleus (AGN).

1.1 Active galactic nuclei

An active galaxy is a galaxy whose nucleus, or central tens of parsecs, exhibits unusually high levels of activity that cannot be accounted for by star formation alone. While stars in a normal galaxy generate electromagnetic radiation mostly in the infrared (IR), optical, and ultraviolet (UV), and to a lesser degree in the radio and X-rays, AGNs produce copious amounts of radiation across the entire spectrum, up to gamma rays. The amount of energy released per decade of wavelength is remarkably constant across the spectrum (e.g., Elvis et al. 1994); for example, the energy in X-rays is ~ 0.05 times that in the UV (e.g., Zamorani et al. 1981).

AGNs cover a large range in bolometric luminosity. At one extreme, the relatively weak AGN in a Seyfert galaxy allows the host galaxy to remain visible, hence a Seyfert galaxy appears as a normal galaxy with a bright central source. At the other extreme, a quasar, short for the antiquated term "quasi-stellar object," is so bright that it outshines the entire galaxy; if the quasar is distant enough that the surface brightness of the galaxy falls below detection limits, or if the angular resolution is not high enough to resolve the galaxy, all that remains in observations is an unresolved point source. The luminosity of quasars (e.g., Matthews & Sandage 1963) and Seyfert galaxies (e.g., Fitch et al. 1967) can vary by tens of percents to a couple times within a timescale of hours to years. A luminous quasar can also temporarily or permanently appear dim if galactic or circumnuclear material happens to lie along our sightline; indeed, the nature of this occluding material is the main subject of this work.

Spectroscopic studies of AGNs reveal the presence of highly ionized species that cannot be produced by UV radiation from stars. In the optical and UV, broad emission lines (BELs) of widths $\gtrsim 2000\,\mathrm{km\,s^{-1}}$ are visible, the most prominent among which are Lyα, C IV 1548, 1551, Hα, Mg II 2796, 2803, O VI 1035, N V 1239, 1243, C III] 1909, Hβ, Si IV 1394, 1403, and O IV] 1400, 1401. Narrow emission lines (NELs) of widths $\sim 500\,\mathrm{km\,s^{-1}}$ are also seen, represented by Lyα, C IV 1548, 1551, [O III] 4959, 5007, Hα, C III] 1909, and [N II] 6583 (e.g., Netzer 1990). Some AGNs also exhibit allowed and forbidden "intermediate" emission lines of widths $\sim 1000\,\mathrm{km\,s^{-1}}$ (e.g., Mason et al. 1996). An AGN is classified as type-1 if it has both BELs and NELs, type-2 if it only has NELs (e.g., Khachikian & Weedman 1971). This strict classification is misleading because AGNs form a continuum between the two types (e.g., Osterbrock & Koski 1976), because AGNs can change from type-1 to type-2 (e.g., LaMassa et al. 2015) or the other way round (e.g., Shappee et al. 2014) over a period of ~ 10 yr, and because, as we shall see below, type-2 AGNs have hidden BELs.

Blueshifted, highly ionized absorption lines are also frequently observed, even in AGNs with little radio or X-ray emission. UV absorption is seen in ~ 60 % of AGNs (Ganguly & Brotherton 2008); these include UV absorbers (e.g., Bahcall et al. 1993) with speeds from $\sim 100\,\mathrm{km\,s^{-1}}$ to $\sim 1000\,\mathrm{km\,s^{-1}}$ (e.g., Anderson & Kraft 1969; Crenshaw et al. 1999), broad absorption lines (BALs) with speeds $\gtrsim 2000\,\mathrm{km\,s^{-1}}$ (e.g., Lynds

1967; Weymann et al. 1991), narrow absorption lines (NALs) with speeds $\lesssim 300\,\mathrm{km\,s^{-1}}$, and mini-BALs with intermediate speeds. In X-rays, we find warm absorbers (e.g., Halpern 1984) with speeds from $\sim 20\,\mathrm{km\,s^{-1}}$ to $\sim 700\,\mathrm{km\,s^{-1}}$ (e.g., Kaastra et al. 2000; Kaspi et al. 2000) in $\gtrsim 50\,\%$ of AGNs (Reynolds 1997), and ultra-fast outflows (UFOs) with speeds from $\sim 0.05\,c$ to $\sim 0.4\,c$ (e.g., Pounds et al. 2003) in $\gtrsim 35\,\%$ of AGNs (Tombesi et al. 2010). UV absorbers and warm absorbers are related phenomena (Crenshaw et al. 1999), and may indeed arise from the same material (Mathur et al. 1994). Warm absorbers and UFOs might be the two ends of a continuum of outflows launched from different distances (Tombesi et al. 2013), but it seems unlikely that the same mechanism could be responsible for outflows with such different kinematics.

When an AGN does not appear effectively point-like, its morphology on the plane of the sky is far from symmetric. The most powerful AGNs in radio galaxies can launch radio jets that propagate $\gtrsim 100\,\mathrm{kpc}$ and carve out large cavities in the circumgalactic medium (e.g., Böhringer et al. 1993). If an AGN is close enough that $\sim 100\,\mathrm{pc}$-scale structures can be resolved, we often see [O III] 5007 emission arranged in a biconical geometry with the apex centered at the AGN, a structure known as an ionization cone (e.g., Pogge 1989; Wilson 1996). Dust, or amorphous grains of graphite or silicate of sizes $\lesssim 1\,\mu\mathrm{m}$, could also be distributed in a similar biconical fashion and reflect light from the AGN; this structure is called a scattering cone (e.g., Pogge & De Robertis 1993; Zakamska et al. 2005, 2006). In about two dozen AGNs, most notably NGC 4258 (e.g., Miyoshi et al. 1995) and NGC 1068 (e.g., Greenhill et al. 1996), masing water vapor is seen in an edge-on, geometrically thin but warped disk of radius $\sim 0.5\,\mathrm{pc}$. The existence of these structures allows us to identify the axis of an AGN: parallel to jets, ionization cones, and scattering cones, but perpendicular to the maser disk. The axis of an AGN may or may not coincide with the axis of its host galaxy (e.g., Ulvestad & Wilson 1984). A surprising revelation is the discovery that NGC 1068 (Antonucci & Miller 1985) and other Seyfert 2s (e.g., Miller & Goodrich 1990), when observed in polarized light, also show BELs; the light is distributed along and polarized perpendicular to the axis.

AGNs emit abundantly in the IR as well. The spectral energy distribution (SED) in the IR is a broad $\sim 1\,\mu\mathrm{m}$ to $\sim 100\,\mu\mathrm{m}$ bump, interpreted as thermal radiation from warm dust (e.g., Rieke & Lebofsky 1981; Barvainis 1987; Sanders et al. 1989; Pier & Krolik 1993). The turnoff at $\lesssim 2\,\mu\mathrm{m}$ is further evidence that dust is responsible, since graphite dust grains sublime at $\sim 1500\,\mathrm{K}$ (e.g., Rees et al. 1969). While SED measurements only tell us the integrated flux within the telescope aperture, the advent of near-infrared (NIR) and mid-infrared (MIR) interferometry in the past decade has furnished us with the first direct observation of the distribution of the IR sources on the sky. Dust can be seen within several parsecs from the centers of NGC 1068 (Wittkowski et al. 2004; Jaffe et al. 2004; Poncelet et al. 2006; Raban et al. 2009), NGC 4151 (Swain et al. 2003; Burtscher et al. 2009; Pott et al. 2010), Centaurus A (Meisenheimer et al. 2007), Circinus (Tristram et al. 2007, 2012, 2014), and other nearby AGNs (Beckert et al. 2008; Hönig et al. 2012, 2013). A sample of 29 AGNs have thus far been

studied in this way (Tristram et al. 2009; Kishimoto et al. 2009, 2011a,b; Kishimoto et al. 2013; Burtscher et al. 2013; López-Gonzaga et al. 2016). Dust in AGNs appears to have a smaller component with temperature ~ 800 K elongated perpendicular to the axis, presumably dust near sublimation, and a larger component with temperature ~ 300 K oriented parallel to the axis. The cooler component contributes most of the MIR emission (Hönig et al. 2012, 2013; Tristram et al. 2012, 2014). On ~ 100 pc scales, MIR emission is also found along the axis (e.g., Tresch-Fienberg et al. 1987; Braatz et al. 1993; Cameron et al. 1993; Bock et al. 2000; Radomski et al. 2002, 2003; Packham et al. 2005; Reunanen et al. 2010; Hönig et al. 2010; Asmus et al. 2014) that appears to be aligned with the cooler interferometric component (Asmus et al. 2016).

The physical explanation for this bewildering list of observations is fairly well understood. The study of stellar motion shows that every galaxy of sufficiently high mass harbors a super-massive black hole (SMBH) at its center (e.g., Kormendy & Richstone 1995; Magorrian et al. 1998). The mass of the SMBH ranges from merely $\sim 5 \times 10^4\, M_\odot$ in the dwarf galaxy RGG 118 (Baldassare et al. 2015) to the monstrous $\sim 4 \times 10^{10}\, M_\odot$ in the hyperluminous quasar S5 0014+813 (Ghisellini et al. 2009). It is the release of gravitational potential energy as gas falls toward the SMBH that ultimately powers an AGN (e.g., Lynden-Bell 1969). The conservation of angular momentum forces the gas into a geometrically thin structure called an accretion disk (§1.3); the characteristic temperature of its innermost regions is $\sim 5 \times 10^5$ K to $\sim 5 \times 10^6$ K, so it emits mostly in the UV. It is believed that these UV photons undergo inverse Compton scattering with relativistic electrons in the corona, which is confined within tens of gravitational radii of the SMBH, and become X-ray photons (e.g., Liang 1979; Haardt & Maraschi 1991). UV radiation from the accretion disk and X-rays from the corona form a power-law continuum in frequency space; this ionizing continuum creates the species whose lines we see. Because the sites where UV radiation and X-rays are generated are much smaller than many other structures of interest, including the AGN torus studied in this dissertation, we can treat them as a single central point source.

Dust blocks optical and UV light; we say that a column of dust along our sightline is optically thick if it removes a fraction $\gtrsim 1/e$ of the background light. The absorption cross section of dust decreases with wavelength from UV to IR (e.g., Draine 2011); therefore, the general behavior of dust is that it absorbs UV radiation, rises in temperature, and re-emits the absorbed energy in the IR. There are indications that light from an AGN does suffer extinction from dust situated close to the source (e.g., MacAlpine 1985); in fact, the existence of dust partly motivates our previous interpretation of observations in terms of dust.

Meanwhile, X-ray obscuration is mainly due to photoelectric absorption by bound electrons and Compton scattering off free or bound electrons. The H I column density of the Milky Way is typically $\lesssim 10^{22}$ cm^{-2} (e.g., Kalberla et al. 2005); this sets a lower limit to the detection of X-ray obscuration in AGNs. Accordingly, we consider an AGN to be obscured in X-rays if it has a column density of $\gtrsim 10^{22}$ cm^{-2}. X-rays at ~ 7 keV to

$\sim 100\,\mathrm{keV}$ are only stopped by Compton scattering; the characteristic interaction cross section is the Thomson scattering cross section $\sigma_\mathrm{T} \approx 6.65 \times 10^{-25}\,\mathrm{cm}^2$, so a gas column is said to be Compton-thick if its column density is $\gtrsim 10^{24}\,\mathrm{cm}^{-2} \sim 1/\sigma_\mathrm{T}$. A Compton-thick gas column blocks all light except far-infrared (FIR), MIR, and X-rays at $\gtrsim 100\,\mathrm{keV}$. Compton-thick AGNs may constitute $\sim 20\,\%$ to $\sim 30\,\%$ of the total AGN population (e.g., Burlon et al. 2011; Ricci et al. 2015), but identifying these objects and producing an unbiased sample remain significant challenges (e.g., Georgantopoulos 2013; Koss et al. 2016). Lastly, given a dust-to-gas ratio, often taken to be the Milky Way value, we expect obscuration in the optical and in X-rays to be correlated.

The only reasonable physical mechanism that can generate polarized light in a type-2 AGN is reflection (Antonucci & Miller 1985). Light from the central source is unpolarized, but when it is reflected off dust or electrons, it is imprinted with a polarization direction that is perpendicular to the plane containing the incident and reflected rays. Now if light could escape the central source isotropically, and there were reflectors all around the central source redirecting it toward the observer, the observer would receive light polarized in every direction, which would combine to essentially unpolarized light. It follows that parts of the solid angle around the central source must be opaque; in particular, since the light from a type-2 AGN is polarized perpendicular to its axis, there must be a reflector along the axis, and there must be optically thick gas arranged in the shape of a torus perpendicular to the axis. This is the classical idea of an AGN torus, although the name must not be taken too literally to mean that dust exists in a completely static, donut-like configuration.

The optical thickness of the torus is explained by the presence of dust. Light emitted along the mid-plane of the torus is absorbed by dust and converted to IR, which produces the hotter dust component detected in IR interferometry; light leaving through the central hole encounters the reflector above the torus and is reflected toward the observer. Ionization and scattering cones are powered by light from the central source, so they also provide information about the geometry of the torus. The fact that these cones do not cover the entire solid angle around the central source implies that the torus should be geometrically thick with an opening toward the axis spanning only a fraction of the solid angle; moreover, the well-defined shapes of the cones from small radii onward suggest that the torus is small and has a relatively sharp edge.

The idea of the torus lends itself to the AGN unification model (e.g., Barthel 1989; Antonucci 1993; Urry & Padovani 1995), as depicted in Figure 1.1. The model argues that all AGNs possess a broad-line region (BLR) and a narrow-line region (NLR). The size of the BLR is $\approx 0.10\,[L/(10^{45}\,\mathrm{erg\,s^{-1}})]^{0.53}\,\mathrm{pc}$, where L is the luminosity of the AGN at 5100 Å (Bentz et al. 2013). The standard explanation for why the BLR gives off BELs is that the gas lies deeper in the gravitational well of the SMBH and thus moves at greater speeds, but it is unclear to what degree radiation pressure affects BLR motion. In comparison, the NLR is extended along the axis on $\sim 10\,\mathrm{pc}$ to $\sim 1000\,\mathrm{pc}$ scales; slower-moving NLR gas produces NELs. AGNs close enough to be observed with IR interferometry are typically dimmer, at $\lesssim 10^{45}\,\mathrm{erg\,s^{-1}}$; for these objects, IR interferometry

shows that the torus is ~ 1 pc, large enough to surround the BLR but not the NLR. The stark contrast in the appearances of type-1 and type-2 AGNs is attributed not to inherent physical differences, but to an uninteresting parameter, namely, the orientation of the AGN axis with respect to the observer. An AGN appears as type-1 if the observer is looking down the axis through the central hole of a face-on torus. The observer has a clear sightline to the central source, the BLR, and the NLR. The same AGN appears as type-2 if the observer is along the mid-plane. The NLR remains visible above the torus, but sightlines to the central source and the BLR are obstructed by the edge-on torus; the UV–to–X-ray continuum and the BELs are only seen when they are reflected off and polarized by material along the axis. This picture is further corroborated by the detection of Compton-thick gas columns in Seyfert 2s (e.g., Risaliti et al. 1999). The ratio of type-2 to type-1 AGNs is typically a few (e.g., Maiolino & Rieke 1995), implying again that the torus covering fraction should be high.

This simplest form of the AGN unification picture, sometimes called the straw person model, is not without contention. An early objection was raised by Miller & Goodrich (1990) who, upon seeing that only half of their Seyfert 2s show polarized BELs, suggested that scattered light from an edge-on AGN may be blocked by the torus if scattering happens much closer to the SMBH than in the straw person model. It could also be that starlight in the aperture dilutes the polarization signal; indeed, the degree of polarization can vary with aperture size (Antonucci et al. 1994).

Most of the difficulty in testing the straw person model rests in unambiguously dividing AGNs into type-1 and type-2. First, obscuration determined through the UV and X-rays may not agree if dust closest to the central source is destroyed by sublimation or sputtering, leaving only gas behind (e.g., Brandt et al. 2000). If AGNs are biased toward larger dust grains than the Milky Way, then the extinction curve would be flatter, and the ratio of optical reddening to gas column density would be smaller than expected assuming the Milky Way dust-to-gas ratio (Maiolino et al. 2001). Similarly, obscuration in the optical and the IR may not correspond; for example, type-1i AGNs are Seyfert 2s that show broad Paβ emission in the IR (Véron-Cetty & Véron 2010). Such AGNs could be assigned opposite types depending on the wavelength of observation.

Second, dust on galactic scales could contribute to the extinction of the BLR (e.g., Maiolino & Rieke 1995; Malkan et al. 1998; Goulding & Alexander 2009; Goulding et al. 2012), particularly in low-luminosity AGNs. Galactic dust alone may suffice to mask the BLR in these AGNs without the need of a torus (Prieto et al. 2014), but it could hide the NLR as well if it is distributed on a large enough scale. BELs could also be diluted by emission lines from star formation in the host galaxy (e.g., Goulding & Alexander 2009; Trump et al. 2015). These two effects are related because star formation throughout most of the history of the universe is expected to occur inside dusty giant molecular clouds.

The unification model leaves unspecified the ratio of type-2 to type-1 AGNs as a function of luminosity, but it is often mistakenly asserted in the straw person model that the ratio is independent of the luminosity

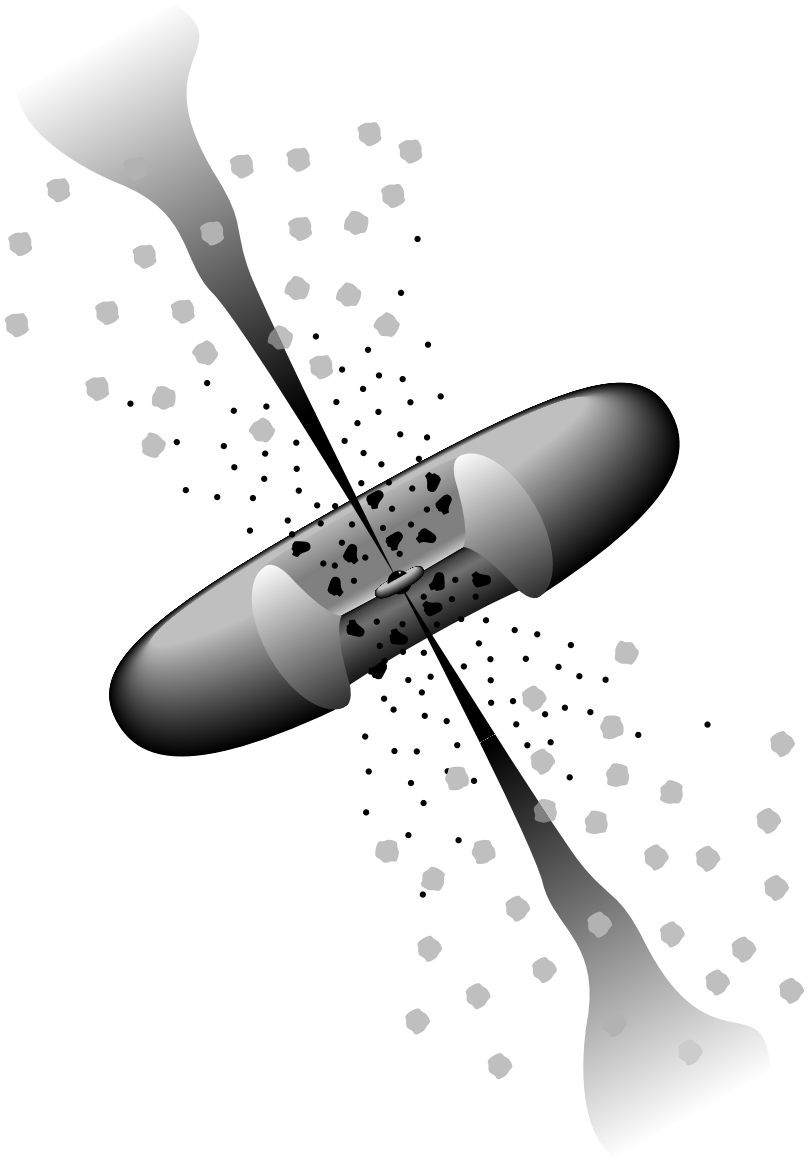

Figure 1.1. Schematic diagram of the straw person model of the AGN unification picture, not to scale, reproduced from Urry & Padovani (1995). At the center is the SMBH with an accretion disk orbiting around it. The geometrically thick torus is the classical torus; photons produced from the disk, shown here as tiny black circles, are blocked by the torus along the mid-plane. Black blobs near the center represent the BLR, while gray blobs further away depict the NLR. A pair of jets emanate from close to the SMBH and travel far beyond the AGN.

of the AGN. Measuring the ratio would inform the unification model, but would also be highly sensitive to how the aforementioned borderline cases are handled (Merloni et al. 2014; Davies et al. 2015). The exact value of the ratio, as well as its dependence on luminosity and redshift, is still under debate (e.g., Ueda et al. 2003; Hasinger 2008; Treister et al. 2008; Lawrence & Elvis 2010; Oh et al. 2015). Particularly influential is the receding torus model; it describes a torus whose height is for reasons unknown fixed, but whose inner radius $R_{\rm in}$, which equals the dust sublimation radius, varies with the luminosity L of the AGN as $R_{\rm in} \propto L^{1/2}$ (Lawrence 1991).

More radical revisions to the straw person model have also been proposed. Since the detection rate of BELs in scattered light is only $\sim 30\,\%$ to $\sim 50\,\%$ (e.g., Moran et al. 2000; Tran 2001), there may be AGNs with no BLRs at all; these are true type-2, unobscured type-2, or non-hidden BLR AGNs (e.g., Tran 2001). The results were contested, particularly on the grounds of selection effects (Antonucci 2002). The BLR may disappear in low-luminosity AGNs (Nicastro 2000; Laor 2003; Elitzur & Ho 2009; Trump et al. 2011). However, it could be that true type-2 AGNs are rare, and some candidates of true type-2 AGNs are merely misclassified because of intrinsically weak BELs (e.g., Shi et al. 2010; Ramos Almeida et al. 2016).

An AGN may change its type throughout its lifetime. A classical type-2 AGN may evolve to a type-1 as it clears away the occluding gas and dust by injecting mechanical and thermal energy into the environment (e.g., Sanders et al. 1988); this would produce observational results mimicking the receding torus model. Conversely, a type-1 AGN may become a true type-2 as it depletes the surrounding gas through accretion, its accretion rate and luminosity drops, and it loses its BLR (e.g., Elitzur et al. 2014) as well as its UV–to–X-ray continuum.

Let us leave the issue of classifying AGNs behind and proceed to our last topic of interest, namely, absorption lines. They are regarded as signatures of cooler outflowing gas. Popular models for wind formation include the accretion disk wind and the thermally driven wind. An accretion disk wind arises when the outer parts of an accretion disk are ionized by radiation from the inner parts and driven outward by line pressure from the same radiation (Proga et al. 2000); this wind could be associated with faster outflows such as BALs and NALs. BALs are observed in a small fraction of AGNs; possible explanations are that BALs occupy a small solid angle (Weymann et al. 1991), or that they occupy a large solid angle but an anisotropic central source does not fully illuminate them (Krolik & Voit 1998). Whether BALs or NALs are observed could be entirely an effect of where the observer is with respect to the AGN (Elvis 2000). A thermally driven wind (Begelman et al. 1983) in the context of the torus (Krolik & Begelman 1986; Balsara & Krolik 1993; Krolik & Kriss 2001; Blustin et al. 2005) refers to gas lifted from the inner surface of the torus, exposed to ionizing radiation from the central source, and heated to the Compton temperature soon after its ionization parameter exceeds unity (Krolik et al. 1981). This wind is identified as UV and warm absorbers in observations. The mildly

relativistic speeds of UFOs suggest that they originate from the vicinity of the SMBH, possibly the accretion disk, but the line-driving mechanism responsible for BALs and NALs is not energetic enough to accelerate gas to such speeds.

Outflows are often invoked as a mechanism for AGN feedback. The mass of an SMBH is correlated with the line-of-sight stellar velocity dispersion of the galactic bulge it resides in (e.g., Gebhardt et al. 2000); this is unexpected since the bulge is much larger than the sphere of influence of the SMBH, and it is taken as evidence that the AGN can somehow regulate the growth of the bulge. One way in which regulation could happen is if outflows couple the immense amount of energy liberated in the accretion disk with the immediate surroundings of the SMBH, with the host galaxy, and with the circumgalactic medium. As it turns out, the outflows listed above do not carry sufficient momentum or energy to expel gas from the galaxy, and only the brightest AGNs (Zakamska & Greene 2014) can unambiguously drive unbound outflows with kinetic energies necessary for feedback (Liu et al. 2013; Zakamska et al. 2016). The details of how feedback operates is a current topic of research, but AGN feedback is widely accepted as an essential ingredient of galaxy evolution.

1.2 Dynamics of AGN tori

Once it was realized that the torus has to be geometrically thick, the next step was to predict its effect on the SED of AGNs. The first attempt in this direction was by Pier & Krolik (1992a). When they performed radiative transfer (RT) on a smooth cylindrical torus of dust, they found that while their model could roughly reproduce the observed IR bump, it under-produces the emission at the shortest and longest wavelengths. The main reason for the latter failure is that the optically thick torus does not allow sufficient radiation from the central source to reach the outer surface of the torus and warm up the dust there. In response to this, Nenkova et al. (2002) suggested a torus model with clumpy dust (see also Nenkova et al. 2008a,b). In this model, UV radiation from the central source can pass through the gaps between clumps and reach dust at greater distances; the energy deposited is then re-radiated in the FIR. The clumpy model explains the IR bump, and is considered among observers as a standard paradigm under which SED measurements are to be interpreted. However, it cannot account for MIR emission along the axis seen in interferometry. A simple revision to the model is to place warm dust in the NLR (Braatz et al. 1993; Pier & Krolik 1993), or dusty clumps around the edge of the ionization cone (Hönig et al. 2012), both of which are directly illuminated by the central source.

All three torus models are phenomenological models in the sense that they are designed to reproduce observational results. They do not contain any physical mechanisms that explain what keeps the dust in a geometrically thick distribution, or how clumps are formed and destroyed. The size and opening angle of the torus, the number density and spatial distribution of clumps, the size and shape of each clump, and the

density contrast between the clumps and the surroundings, are merely parameters obtained by fitting model predictions against observed SEDs; no physical arguments are provided for why the parameters should assume those particular values. Since an SED contains only about twice as many data points as there are parameters in the models, SED fitting is highly degenerate and cannot be relied upon to distinguish one model from another. Progress can only be made by constructing physically motivated torus models; in order to do so, the forces controlling torus dynamics must first be understood.

The torus has an aspect ratio of unity if its velocity dispersion is comparable to its orbital velocity. A torus is said to be at the virial temperature if gas pressure alone can support it against gravity; in this case, the velocity dispersion is entirely due to thermal motion. However, the virial temperature of hydrogen atoms at a distance r from an SMBH of mass M is $\gtrsim 1.7 \times 10^6\,[M/(10^7\,M_\odot)]\,(r/\mathrm{pc})^{-1}\,\mathrm{K}$, hot enough to destroy dust by sputtering (Krolik & Begelman 1988). Many models have been put forward over the past decades in an effort to reconcile the simultaneous presence of dust and angle-dependent obscuration in AGNs. These models fall into five general categories, but as we shall show below, none of them is entirely satisfactory.

Some proposed an intrinsically warped structure as the obscurer. For example, Phinney (1989) and Sanders et al. (1989) advanced the notion that in lieu of a torus, obscuration could be provided by a geometrically thin warped disk. The disk must stretch from ~ 1 pc to $\sim 10^4$ pc to reproduce the observed IR spectrum, at odds with the presence of well-defined ionization cones on ~ 100 pc scales, with IR interferometric observations, and with optical variability on a timescale of years (e.g., Goodrich 1989). Worse still, the covering fraction is less than half except for the most severe warps and twists, and twists are imperative if one must obstruct more than half of the sightlines at high inclinations. Parsec-scale warps and twists have garnered recent attention, with proponents arguing that they can be sustained by stochastic accretion of clumps from random directions (Lawrence & Elvis 2010; Hopkins et al. 2012), or that they are bending modes excited by radial flows caused by a lopsided disk (Hopkins et al. 2012). However, the torus advocated by Lawrence & Elvis (2010) still suffers from the same shortcomings above, whereas the aspect ratio of the Hopkins et al. (2012) torus is only ~ 0.1.

Another option to partially avoid the dynamical problem is for dust to reside in cool clumps, the collisions among which convert orbital shear to bulk velocity dispersion (Krolik & Begelman 1988). The collision rate must be almost once per orbit for the mid-plane to be completely covered. Should these supersonic encounters be inelastic, the resulting shocks would quickly turn the velocity dispersion of clumps into internal energy; a torus that cools efficiently would settle to the mid-plane, and one that does not would be geometrically thick, but so hot that dust is burnt away. Clumps threaded with magnetic fields could be sufficiently elastic, but the conditions are rather unusual, and one would ask how adequate field strength could be sustained.

Other workers turn to large-scale magnetic fields for an answer. Dusty molecular material lifted up from

the surface of the accretion disk around the central mass could be entrained in a magnetocentrifugal wind; in this scenario, the torus is merely the parts of the wind which happen to be optically thick enough (Königl & Kartje 1994). The dust perhaps takes the form of optically thick clumps embedded in the wind (Elitzur & Shlosman 2006; see also Kartje et al. 1999). Alternatively, magnetic fields could directly support a static torus against gravity (Lovelace et al. 1998). Magnetic models, however, require strong, ordered fields on large scales, which are difficult to justify.

Still another alternative is to invoke the nuclear starbursts seen in some Seyfert 2s (e.g., Heckman et al. 1997; González Delgado et al. 2001; Cid Fernandes et al. 2001; Davies et al. 2007). They prompted Wada & Norman (2002) to suggest turbulence stirred up by supernovae as a means of creating a quasi-stable torus, but its size needs to be $\gtrsim 30$ pc, and even then the covering fraction is $\lesssim 0.2$. A recent simulation by Wada et al. (2016) using a smaller central mass shows once again that supernovae can only produce a torus of size ~ 10 pc and covering fraction ~ 0.25. The obscuring gas disk of Hopkins et al. (2016) has similar drawbacks in that its size and aspect ratio are $\gtrsim 10$ pc and $\lesssim 0.3$. Stellar feedback is in fact too weak to keep the torus geometrically thick on parsec scales (Krolik & Begelman 1988). Attacking the problem from a different perspective, Schartmann et al. (2009) considered mass and energy injection by stars in a spherical and isotropic nuclear cluster. Filaments in that scheme are formed by shock waves from supernovae and planetary nebulae interacting with one another, while cold clumps come from cooling. An analogous proposal by Hueyotl-Zahuantitla et al. (2013) looked at supernova ejecta and stellar winds released with some angular momentum. The gas cools and is compressed to filaments, which then flows inward and accumulates at the centrifugal barrier, forming a torus made geometrically thick by X-ray heating. Both models attempt to circumvent the weakness of stellar feedback by injecting gas at the positions of the stars of a spatially extended cluster, hence the fate of the torus is unclear once the starburst ends. Moreover, the specific mass injection rate in the latter model is $\sim 6 \times 10^3$ times the galactic specific star formation rate.

Last but not least, Pier & Krolik (1992b) realized that since dust opacity in the IR is $\gtrsim 10$ times Thomson opacity, even sub-Eddington AGN luminosities could dramatically affect the torus through radiation pressure. In their picture, UV radiation from the central source is converted to IR on the inner surface of a smooth cylindrical torus (Pier & Krolik 1992a); part of the IR radiation diffuses through the torus and supports it. Krolik (2007) revisited the problem and constructed an analytic solution of a smooth axisymmetric torus under the combined influence of gravity and radiation; Shi & Krolik (2008) later extended his work by incorporating the effects of hard X-ray and stellar heating. Unfortunately, both models are overly simplistic in that they assume a hydrostatic torus and the diffusion approximation for the IR radiative flux.

Others have developed ideas along a similar vein. For example, Ohsuga & Umemura (1999) and Ohsuga & Umemura (2001) considered radiation pressure from both an AGN and a nuclear starburst ring, yet their

obscuring structure is stable near the mid-plane only for specific parameters. Everett (2005) and Keating et al. (2012) studied a magnetocentrifugal wind accelerated by radiation from the central source; the wind again depends on the existence of some postulated large-scale magnetic field. An alternative model from Wada (2012, 2015) focuses instead on turbulence generated when gas streams lifted up by radiation fall back to the mid-plane and intersect. Its conclusions can only be tentative because UV heating and radiative cooling in this model assume ionization by starlight while X-ray heating is based on stellar-mass black hole X-ray spectra, entirely ignoring AGN radiation. The model also does not treat dust destruction by sputtering at temperatures $\gtrsim 10^5$ K (Draine & Salpeter 1979). In addition, the omission of reprocessed IR radiation in these three schemes renders their applicability to optically thick tori doubtful. Less directly related is the suggestion from Thompson et al. (2005) that a starburst disk with Eddington luminosity in the IR possesses a tenuous, dusty, and geometrically thick atmosphere.

In a series of articles, Dorodnitsyn & Kallman (Dorodnitsyn et al. 2011, 2012; Dorodnitsyn & Kallman 2012; Dorodnitsyn et al. 2016) investigated the effects of IR radiation pressure on dusty tori using two-dimensional simulations that couple hydrodynamics and radiation. Encouragingly, they found that gas evolves naturally to a geometrically thick obscuring wind. However, there are two limitations to this work. They neglected momentum deposition from direct UV illumination. More worrisome is their use of the flux-limited diffusion (FLD) approximation, which can yield radiative fluxes in completely wrong directions wherever the optical depth is comparable to or smaller than unity. This problem is especially troubling when the dynamical effect of radiation is important (e.g., Davis et al. 2012), as it is here. The recent simulations by Namekata & Umemura (2016) adopt the finite-volume method for radiative transfer (FVMRT) instead, but their simulations are two-dimensional, and their geometrically thin initial condition may be related to their inability to create a geometrically thick structure. Roth et al. (2012) took the complementary direction of performing detailed Monte Carlo RT on an arbitrary static distribution of dusty gas and calculating the radiative acceleration. The fact that they find accelerations exceeding gravity emphasizes that hydrodynamics and RT should be treated together.

The objective of this work is to study torus dynamics with three-dimensional simulations that combine magnetohydrodynamics (MHD) and RT. However, in contrast to previous simulations that include all relevant physical effects at once, we conduct a series of numerical experiments in which mechanisms are added one at a time; in doing so, we hope to distinguish between their effects and garner physical insight. Only toward the end of this process will it be appropriate to construct a torus model that relates to observable quantities. We begin in this work by considering a dusty, magnetized torus that experiences radiative acceleration on dust due to UV radiation from the central source and diffuse IR radiation in the torus. Other ingredients, such as realistic atomic and molecular heating and cooling rates, and dust destruction by sputtering in high-temperature regions,

are left to future iterations.

As we shall see in Chapters 3 and 4, mass is inevitably lost from the UV-irradiated inner surface of the torus; in other words, realistic tori must be resupplied with gas falling in from galactic scales. External feeding may be emulated by putting mass sources at the boundaries of the simulation domain (e.g., Dorodnitsyn et al. 2011, 2012; Dorodnitsyn & Kallman 2012), but this method is subject to a great degree of arbitrariness. Our approach is to begin with a finite amount of mass in the simulation domain and disable mass inflow; because our simulations cannot portray steady-state tori, any connection between simulated and real tori must be posed in terms of the rate of mass resupply necessary to secure stationarity.

1.3 Theory of accretion disks

Since a torus is essentially a geometrically thick accretion disk, it is fruitful to review the physical principles that govern the evolution of disks.

One may naïvely think that a black hole, famously being an object so dense that even light cannot escape its gravitational pull, should produce little electromagnetic radiation. This argument ignores the fact that black holes can be surrounded by copious amounts of gas. As gas falls into the deep gravitational well of the black hole, gravitational potential energy is first converted to kinetic energy, and then to other forms of energy that powers all phenomena around the black hole.

Astrophysical gases typically exist in the form of plasmas. They have number densities far below those encountered in terrestrial laboratories; however, the fact that the mean free path of the particles is much smaller than the length scale of the system justifies the use of the fluid approximation in many situations. A macroscopic plasma is electrically neutral, and most astrophysical plasma is threaded by magnetic fields. The study of the motion of such plasma is called MHD. The ideal MHD condition assumes the plasma is perfectly conductive; in other words, charges can move freely and the electric field in the fluid frame vanishes. This does not mean the electric field is zero in the observer frame, because a time-changing magnetic field induces an electric field as well. The ideal MHD condition holds even at extremely low ionization fractions (Blaes & Balbus 1994; Gammie 1996), and is presumably valid inside the torus where X-rays keep the gas mildly ionized (Neufeld & Maloney 1995).

An interesting result in ideal MHD is Alfvén's theorem (Alfvén 1942), which states that the magnetic flux through a surface moving with the fluid is constant. Loosely put, magnetic fields are frozen into the fluid. Magnetic field lines are dragged along by fluid elements as they move around; conversely, fluid elements can only move along magnetic field lines, not transverse to them.

Gas typically has a finite amount of angular momentum far away from the black hole. The conservation

of angular momentum means that the gas does not collapse spherically radially onto the black hole, but spins faster and faster as it falls in. Furthermore, streams of gas moving in different directions collide and dissipate their kinetic energy until the state of lowest energy obtains. The end result is an accretion disk, a geometrically thin disk of gas along the mid-plane of the black hole in which gas travels in the same direction in almost circular orbits.

Ironically, the conservation of angular momentum that allows the formation of an accretion disk appears to prevent the disk from doing what it is named for, to wit, bringing gas toward the black hole. Angular momentum must be removed before the gas can descend further into the gravitational well and the liberation of gravitational potential energy can continue. If the black hole is in a binary system, the companion can exert a non-axisymmetric torque on the disk and remove angular momentum, but the theoretical community struggled for decades to understand what happens to a symmetric disk until the pivotal role played by the magnetorotational instability (MRI) was clarified (Balbus & Hawley 1991; Hawley & Balbus 1991).

The instability is most easily understood by considering an accretion disk threaded by a weak vertical magnetic field. If an orbiting fluid element is perturbed slightly in the radial direction, it drags field lines along with it. Since the disk is differentially rotating, or more precisely, since the orbital frequency decreases with radius, the field lines are gradually sheared and stretched out in the azimuthal direction as well. A stretched field line behaves like a rubber band in that it allows fluid elements connected by it to exert force on each other. In this case, the fluid element at smaller radius, which orbits at a higher frequency, tugs on the fluid element at greater radius. Angular momentum is transferred from the first fluid element to the second, so the first fluid element falls deeper into the gravitational well while the second fluid element moves further away, increasing the tension in the field line. This creates a runaway process that transports angular momentum outward and leads to the accretion of matter. The characteristic timescale for the growth of the MRI is of the order of an orbital timescale, which is arguably the fastest timescale allowed in a disk. Since the conditions required for MRI to appear are quite general, it is expected to operate in a wide range of conditions. Subsequent numerical simulations demonstrated beyond doubt that the MRI is indeed a robust mechanism for enhancing angular momentum transport (Balbus & Hawley 1998, and references therein).

Kinetic energy in the gas of the disk is ultimately converted to thermal energy by dissipation. If we assume the energy is radiated locally with the disk acting as a blackbody, we can easily compute the disk temperature T as a function of radius R from the central mass (Shakura & Sunyaev 1973; Lynden-Bell & Pringle 1974):

$$\sigma_{\rm SB} T^4 = \frac{3GM\dot{M}}{8\pi R^3}\left[1 - \left(\frac{R}{R_0}\right)^{-1/2}\right]. \tag{1.1}$$

Here M is the central mass, $\dot{M}$ is the accretion rate, R_0 is the inner edge of the accretion disk, and $\sigma_{\rm SB}$ is the Stefan–Boltzmann constant. The pre-factor of the bracket is valid in general, but the bracket itself is a

correction factor that holds only for non-relativistic flows with a zero-torque boundary condition at the inner edge.

The characteristic value of luminosity due to accretion is the Eddington luminosity, defined as $L_{\mathrm{E}} \equiv 4\pi GMc/\kappa_{\mathrm{T}}$, where $\kappa_{\mathrm{T}} \equiv \sigma_{\mathrm{T}}/m_{\mathrm{H}}$ is the Thomson scattering cross section per mass, c is the speed of light, and m_{H} is the mass of a hydrogen atom. The Eddington luminosity is most easily understood in terms of a spherically symmetric system: It is the luminosity at which the radiative acceleration on the accreting material is equal and opposite to the gravitational acceleration, and the accretion rate needed to generate such a luminosity is the Eddington accretion rate. The Eddington luminosity is the upper limit to the accretion rate of a spherically symmetric system, and is the characteristic accretion rate of any other system. The Eddington ratio is the ratio of bolometric luminosity to the Eddington luminosity.

Measuring the Eddington ratio requires knowledge about the central mass and the luminosity of the accretion disk. In the case of AGNs, luminosity can be measured more or less directly, and mass is often determined by means of reverberation mapping (e.g., Peterson et al. 2004) or scaling relations with bulge properties (e.g., Gebhardt et al. 2000). There is weak evidence that the Eddington ratio is insensitive to luminosity (Woo & Urry 2002).

Putting in $M \sim 10^7\, M_\odot$ for a typical SMBH and the characteristic accretion rate $\dot{M} \sim L_{\mathrm{E}}/c^2$, Equation (1.1) yields $T \sim 10^6\, (R/R_{\mathrm{g}})^{-3/4}\,\mathrm{K}$, with $R_{\mathrm{g}} \equiv GM/c^2$ being the gravitational radius; in other words, the accretion disk of an AGN emits mainly in the UV.

CHAPTER 2

METHODS

> The core concepts of Unix have always had a spare, Zen-like simplicity that continues to shine through the layers of historical accidents that have accreted around them. This quality is reflected in the cornerstone documents of Unix, like *The C Programming Language* and the 1974 CACM paper that introduced Unix to the world; one of the famous quotes from that paper observes "…constraint has encouraged not only economy, but also a certain elegance of design." That simplicity came from trying to think not about how much a language or operating system could do, but of how *little* it could do—not by carrying assumptions but by starting from zero (what in Zen is called "beginner's mind" or "empty mind").
>
> Eric S. Raymond, *The Art of Unix Programming*

Having discussed in qualitative terms the observational features of AGNs, we now turn to the main subject, that is, the exploration of the origin of the geometrical thickness of the torus. We consider a cold, dusty, and optically thick torus orbiting a point mass M at the origin. Isotropic UV radiation of luminosity $L_{\rm UV}$ emerges from the origin. UV radiation impinging on the inner surface is absorbed by dust and re-emitted in the IR; radiation pressure from both the IR and the UV, in concert with rotation, supports the torus against gravity. Cylindrical coordinates (R, ϕ, z) are a natural choice for describing this system, although we do occasionally refer to the spherical radius $r \equiv (R^2 + z^2)^{1/2}$. From now on, the adjective "radial" shall implicitly refer to the cylindrically radial direction. We also call the section of the inner surface near the mid-plane the "inner edge."

2.1 Simulation code

Our simulations use the finite-volume MHD code Athena (Stone et al. 2008). As we shall see in §2.2, the MHD equations are essentially a set of conservation equations that relate the rate of change of the volume integral

of some conserved quantity in a cell with the surface integral of its flux through the cell interfaces. A finite-volume discretization assigns to each cell the volume average of the quantity over the entire cell. At each time step, the value of the quantity at the interface between two cells is reconstructed by some interpolation scheme, from which the flux of the quantity through the interface is computed. The same flux is used to update the volume average on either side of the interface; therefore, a finite-volume code conserves a quantity to machine accuracy. For further details on finite-volume methods, the reader is encouraged to consult LeVeque (2002) for a highly readable introduction, and Toro (2009) for more in-depth discussions.

In order to solve the MHD and RT equations simultaneously in one simulation, we augment the MHD code with one of several RT modules. The time-independent module (Davis et al. 2012; Jiang et al. 2012) performs RT on a snapshot of the simulation, computes the Eddington tensor, and uses it to close the angular moments of the RT equation. In comparison, the time-dependent module (Jiang et al. 2014) tracks the propagation of radiation by solving the multi–angle group RT equation directly on a large number of grid rays, rather than adopting *ad hoc* closure prescriptions such as the FLD approximation. Both modules are suited to handling diffusive IR radiation inside the torus, but we are restricted to the time-dependent module because it is the only one available for cylindrical coordinates.

None of these modules is appropriate for point-source radiation crossing the optically thin region between the central source and the torus because they concentrate radiation along directions defined by the angle grid. Contours of constant radiation energy density, instead of being spherically symmetric, show prominent spherically radial spikes coincident with the grid rays. We therefore reserve the time-dependent module for reprocessed IR radiation inside the torus. UV radiation emitted by the central source is handled by a custom-made RT module that employs the method of long characteristics, as described in §2.3.5.

Each time step in our simulation consists of three substeps: in order of execution, they are the UV radiative substep (§2.3.5), the IR radiative substep (§2.3.1), and the MHD substep (§2.2). This approach of breaking down time evolution into substeps is called operator splitting; in particular, our method of carrying out substeps in fixed order is known as Godunov splitting. We modify Athena to use Godunov splitting so that momentum and energy are conserved in each substep separately, and so that our UV RT module can be introduced with minimal changes to the algorithm. Although this formally makes our code first-order accurate in time, the difference between Godunov splitting and the formally second-order accurate Strang splitting is minimal (e.g., LeVeque 1998).

2.2 Ideal magnetohydrodynamics

The equations of ideal MHD in Newtonian mechanics are

$$\frac{\partial \rho}{\partial t} + \nabla \cdot (\rho \mathbf{v}) = 0, \tag{2.1}$$

$$\frac{\partial}{\partial t}(\rho \mathbf{v}) + \nabla \cdot (\rho \mathbf{v}\mathbf{v} + p^* \mathsf{I} - \mathbf{B}\mathbf{B}) = -\rho \nabla \Phi + \mathbf{S}^{\rm m}_{\rm IR} + \mathbf{S}^{\rm m}_{\rm UV}, \tag{2.2}$$

$$\frac{\partial E}{\partial t} + \nabla \cdot [(E + p^*)\mathbf{v} - (\mathbf{B} \cdot \mathbf{v})\mathbf{B}] = -\rho \mathbf{v} \cdot \nabla \Phi + S^{\rm e}_{\rm IR} + S^{\rm e}_{\rm UV}, \tag{2.3}$$

$$\frac{\partial \mathbf{B}}{\partial t} - \nabla \times (\mathbf{v} \times \mathbf{B}) = \mathbf{0}. \tag{2.4}$$

Here ρ, $\mathbf{v}$, and p are gas density, velocity, and pressure, while $\mathbf{B}$ is the magnetic field; the unit of magnetic field is chosen such that the magnetic permeability is unity. Gas temperature, total pressure, and total energy density are $T = p/(\rho R_{\rm ideal})$, $p^* = p + \frac{1}{2}B^2$, and $E = \frac{1}{2}\rho v^2 + p/(\gamma - 1) + \frac{1}{2}B^2$ respectively, where $R_{\rm ideal}$ and γ are the specific ideal gas constant and the ratio of specific heats. The gravitational potential of the central mass is $\Phi(\mathbf{r}) = -GM/r$. The energy and momentum source terms due to radiation are $S^{\rm e}_{\rm IR,UV}$ and $\mathbf{S}^{\rm m}_{\rm IR,UV}$; we shall define the IR source terms in §2.3.1, and the UV source terms in §2.3.5. Finally, the isotropic rank-two tensor is denoted by I. Equations (2.1) to (2.3) are essentially the conservation equations of mass, momentum and energy. Equation (2.4) is the induction equation, which is a consequence of Alfvén's theorem (§1.3).

The presence of dust in the torus means that gas temperature is $\lesssim 10^5$ K, otherwise dust would be rapidly destroyed by sputtering (Draine & Salpeter 1979). This temperature is much smaller than the virial temperature, hence the gas sound speed is also a tiny fraction of the orbital velocity, or $c_{\rm s}/v_\phi \ll 1$. Because gas pressure alone falls far short of maintaining the geometrical thickness of the torus, it is dynamically unimportant compared to whatever pressure that actually provides support against gravity, such as IR radiation pressure, so an approximate equation of state for the gas is entirely satisfactory. This approximation breaks down outside the torus body, particularly in the central hole where photoionization and Compton recoil can strongly heat the gas (Krolik & Begelman 1986; Krolik & Kriss 2001). In the interest of focusing attention on radiation-driven dynamics, in the simulations presented here we do not change the equation of state between the body and the central hole. We plan in future work to incorporate photoionization, Compton recoil, and related processes; the increased gas pressure in the central hole could potentially alter the shape of the inner surface.

We treat dust and gas as a single fluid with common velocity and temperature. The fact that dust contributes significantly to IR emission implies a dust temperature below sublimation. We expect hydrogen at such temperature to remain molecular and the vibrational modes of the molecule to be weakly excited; we therefore set $R_{\rm ideal} = k_{\rm B}/(2m_{\rm H})$ and $\gamma = \frac{7}{5}$.

2.3 Radiative transfer

The quality of a radiative hydrodynamics (RHD) or radiative magnetohydrodynamics (RMHD) simulation depends heavily on the accuracy of its RT algorithm. Here we merely recapitulate the RT equation solved; the reader is directed to Jiang et al. (2014) for the numerical algorithm. This is followed by a comprehensive discussion of our improvements to the IR RT module, and of our tailor-made UV RT module. Finally, we end the section by presenting our approximation formulae for IR and UV opacities.

2.3.1 Time-dependent IR radiative transfer

To first order in v/c, where c is the speed of light, the mixed-frame time-dependent RT equation for IR radiation interacting with gray material reads (Jiang et al. 2014)

$$\begin{aligned}\frac{1}{c}\frac{\partial I_{\rm IR}}{\partial t} + \hat{\mathbf{n}}\cdot\nabla I_{\rm IR} &= \left(-1+\hat{\mathbf{n}}\cdot\frac{\mathbf{v}}{c}\right)\rho\,(\kappa_{\rm IR}+\sigma_{\rm IR})I_{\rm IR} \\ &+ \left(1+3\,\hat{\mathbf{n}}\cdot\frac{\mathbf{v}}{c}\right)\rho\,(\kappa_{\rm IR}B+\sigma_{\rm IR}J_{\rm IR}) - 2\rho\sigma_{\rm IR}\frac{\mathbf{v}}{c}\cdot\mathbf{H}_{\rm IR} + \rho\,(\kappa_{\rm IR}-\sigma_{\rm IR})\frac{\mathbf{v}}{c}\cdot(\mathbf{H}^0_{\rm IR}-\mathbf{H}_{\rm IR}). \quad (2.5)\end{aligned}$$

The specific intensity integrated over the IR in the observer frame is $I_{\rm IR}(\hat{\mathbf{n}})$; its lowest three angular moments are $J_{\rm IR}$, $\mathbf{H}_{\rm IR}$, and $\mathsf{K}_{\rm IR}$, from which the IR radiation energy density and flux follow as $E_{\rm IR} = (4\pi/c)J_{\rm IR}$ and $\mathbf{F}_{\rm IR} = 4\pi\mathbf{H}_{\rm IR}$. The frequency-integrated blackbody mean intensity is $B(T) = ca_{\rm SB}T^4/(4\pi)$, where $a_{\rm SB}$ is the radiation constant. The coupling between gas and radiation is mediated by $\kappa_{\rm IR}$ and $\sigma_{\rm IR}$, the comoving absorption and scattering cross sections per mass in the IR. If we take the zeroth and first angular moments of Equation (2.5), we get

$$\frac{1}{c}\frac{\partial J_{\rm IR}}{\partial t} + \nabla\cdot\mathbf{H}_{\rm IR} = \rho\kappa_{\rm IR}(B-J_{\rm IR}) + \rho\,(\kappa_{\rm IR}-\sigma_{\rm IR})\frac{\mathbf{v}}{c}\cdot\mathbf{H}^0_{\rm IR} \equiv -\frac{1}{4\pi}S^{\rm e}_{\rm IR}, \quad (2.6)$$

$$\frac{1}{c}\frac{\partial \mathbf{H}_{\rm IR}}{\partial t} + \nabla\cdot\mathsf{K}_{\rm IR} = \rho\kappa_{\rm IR}\frac{\mathbf{v}}{c}(B-J_{\rm IR}) - \rho\,(\kappa_{\rm IR}+\sigma_{\rm IR})\mathbf{H}^0_{\rm IR} \equiv -\frac{c}{4\pi}\mathbf{S}^{\rm m}_{\rm IR}. \quad (2.7)$$

The remaining piece to specify in Equations (2.5) to (2.7) is $\mathbf{H}^0_{\rm IR}$, the first angular moment of the IR specific intensity in the fluid frame. It is related to the angular moments in the observer frame by a Lorentz transformation (Mihalas & Weibel-Mihalas 1984):

$$\mathbf{H}^0_{\rm IR} = \mathbf{H}_{\rm IR} - \frac{\mathbf{v}}{c}J_{\rm IR} - \frac{\mathbf{v}}{c}\cdot\mathsf{K}_{\rm IR} + \mathrm{O}(v^2/c^2). \quad (2.8)$$

2.3.2 Reduced speed of light approximation

The radiative timescale governing Equations (2.5) to (2.7) is shorter than the hydrodynamic timescale of Equations (2.1) to (2.3) by a factor of $c/v \gg 1$. Our primary concern is the hydrodynamic timescale, whereas the fast variation of $I_{\rm IR}$ relative to ρ, $\mathbf{v}$, and p is uninteresting since radiation merely equilibriates with the gas

in between hydrodynamic time steps. To avoid following the system on the radiative timescale, we adopt the method of reduced speed of light (Gnedin & Abel 2001; Skinner & Ostriker 2013).

The physical light speed c attached to the time derivatives in Equations (2.5) to (2.7) is substituted with the reduced light speed $\hat{c}$ (see also Gnedin 2016). This allows the use of coarser temporal resolution since the rate of change of $I_{\rm IR}$ in Equation (2.5), including thermalization by absorption, isotropization by scattering, propagation in vacuum, and advection in optically thick gas, is slowed down by a factor of $\hat{c}/c$. The source terms $S^{\rm e}_{\rm IR}$ and $\mathbf{S}^{\rm m}_{\rm IR}$ are not altered, only the rate at which they change $J_{\rm IR}$ and $\mathbf{H}_{\rm IR}$ in Equations (2.6) and (2.7); in fact, they must not be touched in Equations (2.2) and (2.3) if we are to preserve gas dynamics.

Our approximation does not stop radiation from reaching equilibrium with the gas inasmuch as $v < \hat{c} \ll c$. However, it is critical that we not replace c attached to $\mathbf{v}/c$ in Equations (2.5) to (2.7), otherwise $\mathbf{H}_{\rm IR}$ could be beamed in the direction of $\mathbf{v}$ even when $v \lesssim \hat{c} \ll c$.

Because the rate of change of energy and momentum of gas is $c/\hat{c}$ times that of radiation, Equations (2.2), (2.3), (2.6) and (2.7) taken together do not conserve the physical values of energy and momentum, but $E + 4\pi J_{\rm IR}/\hat{c}$ and $\rho\mathbf{v} + 4\pi\mathbf{H}_{\rm IR}/(c\hat{c})$ instead. Granted that spurious transients may manifest themselves on approach to energy and momentum equilibrium between gas and radiation, we nevertheless expect time-averaged values of $S^{\rm e}_{\rm IR}$ and $\mathbf{S}^{\rm m}_{\rm IR}$ to vanish once equilibrium prevails.

A technical point to bear in mind is that the time-dependent RT module of Athena evaluates $S^{\rm e}_{\rm IR}\,\Delta t$ and $\mathbf{S}^{\rm m}_{\rm IR}\,\Delta t$ not from the right-hand sides of Equations (2.6) and (2.7), but directly from $\Delta I_{\rm IR}$ as computed by the IR radiative substep; the conversion from $\Delta I_{\rm IR}$ to $S^{\rm e}_{\rm IR}\,\Delta t$ and $\mathbf{S}^{\rm m}_{\rm IR}\,\Delta t$ therefore necessitates a factor of $c/\hat{c}$.

2.3.3 Improvement to treatment of scattering in Athena

We consider the treatment of scattering opacity by the time-dependent RT module of Athena. The notation follows Jiang et al. (2014), except that here c and $\hat{c}$ are the physical and reduced light speeds. We define $\sigma_{\rm s}$ as the scattering cross section per volume, Δt as the time step, and $\zeta \equiv \tau^*_{\rm s} v/c$, where $\tau^*_{\rm s} \equiv \sigma_{\rm s}\hat{c}\Delta t$.

The module handles scattering by solving equations (29) and (30) listed in the reference. We repeat the equations below, minus a couple typos:

$$\begin{pmatrix} a_1+b_1+c_1 & b_2+c_1 & b_3+c_1 & \cdots & b_N+c_1 \\ b_1+c_2 & a_2+b_2+c_2 & b_3+c_2 & \cdots & b_N+c_2 \\ b_1+c_3 & b_2+c_3 & a_3+b_3+c_3 & \cdots & b_N+c_3 \\ \vdots & \vdots & \vdots & \ddots & \vdots \\ b_1+c_N & b_2+c_N & b_3+c_N & \cdots & a_N+b_N+c_N \end{pmatrix} \begin{pmatrix} x_1 \\ x_2 \\ x_3 \\ \vdots \\ x_N \end{pmatrix} = \begin{pmatrix} r_1 \\ r_2 \\ r_3 \\ \vdots \\ r_N \end{pmatrix}, \tag{2.9}$$

where

$$a_l \equiv W_l^{-1}[1 + \tau_s^*(1 - \mathbf{n}_l \cdot \mathbf{v}/c)], \tag{2.10a}$$

$$b_l \equiv \tau_s^*[2(\mathbf{n}_l \cdot \mathbf{v}/c) - (\mathbf{n}_l \cdot \mathbf{v}/c)^2 - v^2/c^2], \tag{2.10b}$$

$$c_l \equiv -\tau_s^*[1 + 3(\mathbf{n}_l \cdot \mathbf{v}/c)], \tag{2.10c}$$

$$x_l \equiv W_l I_l^{n+1}, \tag{2.10d}$$

$$r_l \equiv I_l^n. \tag{2.10e}$$

In the process of computing the LU decomposition of the matrix, $c_l - c_N \sim \zeta$ appears multiple times in the denominator. If $\zeta \ll 1$, some elements of the resultant matrices are ~ 1 while others are $\sim \zeta^{-1}$; put differently, the matrices are ill-conditioned, with the ratio of the greatest to smallest singular values of either matrix being $\sim \zeta$. Because the solution is computed using back-substitution as $x_i = U_{ij}^{-1} L_{jk}^{-1} r_k^{'}$, it could be highly inaccurate. The code already includes checks to avoid this kind of situation, but it is easy to construct triples of τ_s^*, v, and c that bypass them.

When ζ is below a certain threshold, it is preferable to regard the scattering equation, written in the form

$$I_l^n = \sum_{m=1}^{N} (\lambda_{lm} + \epsilon_{lm}) I_m^{n+1}, \tag{2.11}$$

where

$$\lambda_{lm} \equiv (1 + \tau_s^*)\delta_{lm} - \tau_s^* W_m, \tag{2.12a}$$

$$\epsilon_{lm} \equiv \tau_s^*(a_l^{'}\delta_{lm} + b_m^{'} W_m + c_l^{'} W_m), \tag{2.12b}$$

$$a_l^{'} \equiv -\mathbf{n}_l \cdot \mathbf{v}/c, \tag{2.12c}$$

$$b_l^{'} \equiv 2(\mathbf{n}_l \cdot \mathbf{v}/c) - (\mathbf{n}_l \cdot \mathbf{v}/c)^2, \tag{2.12d}$$

$$c_l^{'} \equiv -[3(\mathbf{n}_l \cdot \mathbf{v}/c) + v^2/c^2], \tag{2.12e}$$

and δ_{lm} is the Kronecker delta, as a perturbative equation and solve it iteratively. The procedure starts with $I_l^{n+1} \leftarrow I_l^n$; each iterative step updates the solution as

$$I_l^{n+1} \leftarrow \sum_{m=1}^{N} \lambda_{lm}^{-1} \left[I_m^n - \sum_{p=1}^{N} \epsilon_{mp} I_p^{n+1} \right]. \tag{2.13}$$

The special structure of the matrix allows the inner multiplication to be accomplished with time expenditure $\mathrm{O}(N)$, while the multiplication of any vector v_m by the inverse matrix λ_{lm}^{-1} is simply

$$\sum_{m=1}^{N} \lambda_{lm}^{-1} v_m = \frac{1}{1 + \tau_s^*} \left(v_l + \frac{\tau_s^* \sum_{m=1}^{N} W_m v_m}{1 + \tau_s^* - \tau_s^* \sum_{m=1}^{N} W_m} \right) = \frac{1}{1 + \tau_s^*} \left(v_l + \tau_s^* \sum_{m=1}^{N} W_m v_m \right). \tag{2.14}$$

The chief aim of this modification is not to obtain a more accurate solution when $\zeta \sim 10^{-15}$; rather, it prevents the numerical instability that the standard algorithm exhibits in the static or extremely optically thin limit. Furthermore, the new solution is not to replace, but to complement, the old solution.

The threshold at which we switch between solution strategies is somewhat arbitrary; our choice is $\zeta = 10^{-5}$ as the standard algorithm has not yet shown instability above it. If double-precision floating-point numbers are used, the machine epsilon is $2^{-52} \approx 2.22 \times 10^{-16}$, so the iterative step should be performed at least four times.

2.3.4 Reduction of numerical artifacts in advection of IR radiation in Athena

Jiang et al. (2014) break the advective term of Equation (2.5) down into

$$c\,\hat{\mathbf{n}} \cdot \nabla I_{\rm IR} = \nabla \cdot (\hat{\mathbf{n}}\, c I_{\rm IR}) = \nabla \cdot \{\hat{\mathbf{n}}\,[c I_{\rm IR} - 3(\hat{\mathbf{n}} \cdot \mathbf{v}) J_{\rm IR}]\} + \nabla \cdot \{\hat{\mathbf{n}}\,[3(\hat{\mathbf{n}} \cdot \mathbf{v}) J_{\rm IR}]\}. \tag{2.15}$$

Both terms on the right-hand side are treated as advection. The advective flux under each divergence operator is further split into two parts, an advected quantity and an advection velocity. The first term produces advected quantities $n_x[I_{\rm IR} - 3(\hat{\mathbf{n}}\cdot\mathbf{v})J_{\rm IR}/c]$, $n_y[I_{\rm IR} - 3(\hat{\mathbf{n}}\cdot\mathbf{v})J_{\rm IR}/c]$, and $n_z[I_{\rm IR} - 3(\hat{\mathbf{n}}\cdot\mathbf{v})J_{\rm IR}/c]$, with respective advection velocities $c\alpha$ sign n_x, $c\alpha$ sign n_y, and $c\alpha$ sign n_z; here n_x, n_y, and n_z are the components of a grid ray $\hat{\mathbf{n}}$, with x, y, and z being the radial, azimuthal, and vertical directions defined locally at a cell, and α is a limiter on the advection velocity defined by Jiang et al. (2013b). The second term yields advected quantities $3n_x^2 J_{\rm IR}$, $3n_y^2 J_{\rm IR}$, and $3n_z^2 J_{\rm IR}$, with respective advection velocities $(\hat{\mathbf{n}}\cdot\mathbf{v})/n_x$, $(\hat{\mathbf{n}}\cdot\mathbf{v})/n_y$, and $(\hat{\mathbf{n}}\cdot\mathbf{v})/n_z$. Given arbitrary advected quantity q and advection velocity $u(q)$, the nonlinear advection equation

$$\frac{\partial q}{\partial t} + \frac{\partial}{\partial x}[q u(q)] = 0 \tag{2.16}$$

can be solved numerically with standard methods (e.g., LeVeque 2002); this is exactly what Jiang et al. (2014) did with the advected quantities and advection velocities derived from Equation (2.15).

The problem with this approach is that the grid rays have the same directions in all cells; therefore, the components n_x, n_y, and n_z of a grid ray $\hat{\mathbf{n}}$ in the local x-, y-, and z-directions vary with the azimuthal coordinate of the cell. Some cells in the simulation domain can contain grid rays lying close to the poloidal plane and thus having very small n_y. In this scenario, the implementation described above gives an enormous advection velocity in the y-direction for the second term on the right-hand side of Equation (2.15), with the consequence that the specific intensity on this grid ray can turn negative purely from advection. This can happen even when slope limiters are applied. Since the code patches up negative numbers by replacing them with a tiny positive number, this leads to an increase in radiative energy in the affected cells. A simple fix for this problem is to

regard the second term as consisting of advected quantities $3n_xJ$, $3n_yJ$, and $3n_zJ$, with the same advection velocity $\hat{\mathbf{n}} \cdot \mathbf{v}$ for all three directions.

2.3.5 Time-independent long-characteristics UV radiative transfer

Dust has $\sim 10^2$ to $\sim 10^3$ times greater opacity to UV radiation than to IR radiation (e.g., Semenov et al. 2003); such a large contrast compels us to treat radiation at the two frequencies separately.

UV radiation comes from the innermost regions of an accretion disk at the origin, but the angular distribution of its radiative flux is poorly known. The classical picture of a limb-darkened disk only holds for a Newtonian, scattering-dominated, geometrically thin, and optically thick disk; disk turbulence, thermal instabilities, coronal scattering, as well as relativistic boosting, beaming, and ray bending, could all skew the angular profile of emergent radiation. The axis of the disk also need not be aligned with that of the torus. Because we lack a detailed disk model, and because our desire is to understand physical principles rather than to provide observables, we simply allow our UV radiative flux to be isotropic instead of giving it a more complicated and more model-dependent angular distribution.

We have developed a time-independent long-characteristics RT module to deal with UV radiation from a point source at the origin in cylindrical coordinates. Our ray-casting algorithm is similar to that of Amanatides & Woo (1987). We construct a ray from the source to the center of every cell in the simulation domain, extend it so that it reaches the far side of the destination cell, and then chop it up into segments, one for each cell the ray passes through. This ray-casting is done once, before the simulation starts. Our adoption of cylindrical coordinates means that we only need to solve the ray-casting problem in two dimensions. A subtlety of our algorithm is that, whenever a ray passes very close to a cell corner, we allow the ray to pass diagonally through it.

At the beginning of a time step, we compute the UV radiation energy density in the destination cell by

$$\frac{4\pi}{c} J_{\rm UV} \equiv \frac{L_{\rm UV}}{4\pi r^2 c} e^{-\tau_{\rm UV}} \frac{\exp(\frac{1}{2}\tau^*_{\rm UV}) - \exp(-\frac{1}{2}\tau^*_{\rm UV})}{\tau^*_{\rm UV}}, \tag{2.17}$$

where $L_{\rm UV}$ is the luminosity of the source in the UV and $\mathbf{r}$ is the displacement from the source to the destination cell. We determine the UV optical depth $\tau_{\rm UV}$ from the origin to the destination cell by accumulating the products of the length of each segment and $\rho\kappa_{\rm UV}$ averaged over the cell in which the segment lies; note that we consider only half of the length of the last segment in this exercise. The last factor in the equation comes from averaging $J_{\rm UV}$ over the entire last segment, which has UV optical depth $\tau^*_{\rm UV}$; its inclusion improves the agreement of the UV energy and momentum absorption rate between runs at different resolutions, particularly at locations where $\tau_{\rm UV} \lesssim 1$.

To arrive at the energy and momentum source terms of gas due to UV radiation, we remind ourselves of the RT equation in the form derived by Mihalas & Klein (1982):

$$\frac{1}{c}\frac{\partial I_{\rm UV}}{\partial t} + \hat{\mathbf{n}}\cdot\nabla I_{\rm UV} = \left(-1 + \hat{\mathbf{n}}\cdot\frac{\mathbf{v}}{c}\right)\rho\,(\kappa_{\rm UV}+\sigma_{\rm UV})I_{\rm UV} + \left(1 + 3\,\hat{\mathbf{n}}\cdot\frac{\mathbf{v}}{c}\right)\rho\,(\kappa_{\rm UV}B + \sigma_{\rm UV}J_{\rm UV}) - 2\rho\,\sigma_{\rm UV}\frac{\mathbf{v}}{c}\cdot\mathbf{H}_{\rm UV}. \quad (2.18)$$

The zeroth and first angular moments of Equation (2.18) are

$$\frac{1}{c}\frac{\partial J_{\rm UV}}{\partial t} + \nabla\cdot\mathbf{H}_{\rm UV} = \rho\,\kappa_{\rm UV}(B - J_{\rm UV}) + \rho\,(\kappa_{\rm UV}-\sigma_{\rm UV})\frac{\mathbf{v}}{c}\cdot\mathbf{H}_{\rm UV} \equiv -\frac{1}{4\pi}S^{\rm e}_{\rm UV}, \quad (2.19)$$

$$\frac{1}{c}\frac{\partial \mathbf{H}_{\rm UV}}{\partial t} + \nabla\cdot\mathsf{K}_{\rm UV} = -\rho\,(\kappa_{\rm UV}+\sigma_{\rm UV})\left(\mathbf{H}_{\rm UV} - \frac{\mathbf{v}}{c}\cdot\mathsf{K}_{\rm UV}\right) + \frac{\mathbf{v}}{c}\rho\,(\kappa_{\rm UV}B + \sigma_{\rm UV}J_{\rm UV}) \equiv -\frac{c}{4\pi}\mathbf{S}^{\rm m}_{\rm UV}. \quad (2.20)$$

Lowrie et al. (1999) pointed out that Equations (2.18) to (2.20) do not give the correct equilibrium in moving fluids. To overcome this problem, the time-dependent RT module of Athena solves the modified Equation (2.5), but Equations (2.5) and (2.18) are identical to first order in v/c save for the subscripts.

For time-independent RT, which applies to the UV, we drop the time derivatives from Equations (2.18) to (2.20). In the special case of point-source UV radiation interacting with purely absorbing material that does not re-radiate in the UV, we set $\sigma_{\rm UV} = 0$, $B = 0$, $\mathbf{H}_{\rm UV} = \hat{\mathbf{e}}_r J_{\rm UV}$, and $\mathsf{K}_{\rm UV} = \hat{\mathbf{e}}_r\hat{\mathbf{e}}_r J_{\rm UV}$ in Equations (2.19) and (2.20); the source terms we seek can be skimmed off as

$$-\frac{1}{4\pi}S^{\rm e}_{\rm UV} \equiv -\rho\,\kappa_{\rm UV}J_{\rm UV}\left(1 - \hat{\mathbf{e}}_r\cdot\frac{\mathbf{v}}{c}\right), \quad (2.21)$$

$$-\frac{c}{4\pi}\mathbf{S}^{\rm m}_{\rm UV} \equiv -\rho\,\kappa_{\rm UV}J_{\rm UV}\,\hat{\mathbf{e}}_r\left(1 - \hat{\mathbf{e}}_r\cdot\frac{\mathbf{v}}{c}\right). \quad (2.22)$$

Observe that a consistent solution cannot be reached with Equations (2.6) and (2.7).

As implied by Equations (2.2) and (2.3), the source terms are added directly to the gas at the beginning of the time step. The energy source term is rather large compared to the other terms of Equation (2.3), so the gas is temporarily overheated. The IR radiative substep is then carried out as described by Jiang et al. (2014), during which the gas releases almost all of the energy it gained from the UV into the IR. Although the source terms are added using the explicit Euler method, the IR radiative substep proceeds by the implicit Euler method, hence a large energy source term does not pose a problem.

Despite the sharp rise in gas temperature after the UV long-characteristics substep, we must not change the IR and UV opacities until the IR radiative substep is finished; otherwise, gas exposed to UV radiation would be absorbing UV and emitting IR at two unrelated opacities, which would generate specious temperature fluctuations with a period equal to two or three time steps around the true equilibrium value.

2.3.6 IR and UV opacities

The chief sources of opacity in our system are dust absorption and electron scattering, which we model as

$$\kappa_{\rm IR}(T) \equiv \bar{\kappa}_{\rm IR} \times \frac{1}{2}\left[1 - \tanh\frac{\log_{10}(T/T_{\rm ds})}{\Delta_{\rm ds}}\right], \tag{2.23}$$

$$\kappa_{\rm UV}(T) \equiv \bar{\kappa}_{\rm UV} \times \frac{1}{2}\left[1 - \tanh\frac{\log_{10}(T/T_{\rm ds})}{\Delta_{\rm ds}}\right], \tag{2.24}$$

$$\sigma_{\rm IR}(T) \equiv \kappa_{\rm T} \times \frac{1}{2}\left[1 + \tanh\frac{\log_{10}(T/T_{\rm hi})}{\Delta_{\rm hi}}\right]. \tag{2.25}$$

In these fitting formulae, $T_{\rm ds} \approx 1500\,{\rm K}$ is the dust sublimation temperature (e.g., Rees et al. 1969; Rieke & Lebofsky 1981; Barvainis 1987), $T_{\rm hi} \approx 4013\,{\rm K}$ is the temperature at which hydrogen atoms in local thermodynamic equilibrium (LTE) at a number density of $10^4\,{\rm cm}^{-3}$ are collisionally half-ionized, and $\kappa_{\rm T} \approx 0.397\,{\rm cm}^2\,{\rm g}^{-1}$ is the Thomson scattering cross section per mass. The dust opacities are normalized to Thomson as $\bar{\kappa}_{\rm IR}/\kappa_{\rm T} = 20$ and $\bar{\kappa}_{\rm UV}/\kappa_{\rm T} = 80$. The parameters governing the transition between opacity regimes are $\Delta_{\rm ds} = 0.05$ and $\Delta_{\rm hi} \approx 0.196$.

The actual value of $\kappa_{\rm UV}/\kappa_{\rm IR}$ is $\sim 10^2$ to $\sim 10^3$ (e.g., Semenov et al. 2003), but we cannot model this in our simulations. The thickness of the UV radiation absorption layer at the inner surface is $\propto \kappa_{\rm IR}/\kappa_{\rm UV})$, so a large opacity ratio would entail the use of a grid size small enough to resolve an extremely thin absorption layer. Moreover, because all of the momentum in UV radiation is delivered within the layer, gas in the layer experiences an acceleration $\propto \kappa_{\rm UV}$. With greater $\kappa_{\rm UV}$, tracking the development of the inner surface would necessitate high temporal resolution, and the value of $\hat{c}$ would also need to be revised upward to keep $v < \hat{c}$.

2.4 Simulation setup

We now discuss technicalities pertaining to the construction of the RHD simulations described in Chapter 3 and the RMHD simulations described in Chapter 4.

2.4.1 Central mass and reduced speed of light

The astute reader will notice that we have so far evaded any mention of the value of the central mass M in our simulations. This is because its choice is by far the most complicated consideration.

Sharp discontinuities in numerical calculations are flanked by ringing artifacts, which resemble wiggles associated with the Gibbs phenomenon. These artifacts usually damp out over time; however, in the case of a cylindrical discontinuity in a gas partially supported against gravity, such as the inner edge, the artifact grows rapidly at any spatial resolution. Experimentation with different values of $c_{\rm s}/v_\phi$ shows that the artifact can be suppressed by demanding $c_{\rm s}/v_\phi \gtrsim {\rm O}(0.1)$. If $c_{\rm s}/v_\phi$ is kept at the low end of the numerically permitted

range, gas pressure should always be weak compared to gravity; as long as gas pressure is a minor influence, it should not matter if it is not as tiny as in realistic astrophysical circumstances.

These constraints determine M. The gas equilibrium temperature $T_{\rm in}$ at the inner edge $R_{\rm in}$ is set by

$$\frac{\kappa_{\rm UV} L_{\rm UV}}{4\pi R_{\rm in}^2} = \kappa_{\rm IR} c a_{\rm SB} T_{\rm in}^4; \tag{2.26}$$

the stability requirement $R_{\rm ideal} T_{\rm in}/(GM/R_{\rm in}) \gtrsim {\rm O}(0.1)^2$ then becomes

$$\begin{aligned} M &\lesssim \frac{R_{\rm ideal}^2 (\kappa_{\rm UV}/\kappa_{\rm IR})}{G \kappa_{\rm T} a_{\rm SB} T_{\rm ds}^2} \left(\frac{L_{\rm UV}}{L_{\rm E}}\right) \left(\frac{T_{\rm in}}{T_{\rm ds}}\right)^{-2} {\rm O}(0.1)^{-4} \\ &\approx 7.58 \times 10^{-4} \left(\frac{L_{\rm UV}/L_{\rm E}}{0.1}\right) \left(\frac{T_{\rm in}}{T_{\rm ds}}\right)^{-2} {\rm O}(0.1)^{-4} M_\odot, \end{aligned} \tag{2.27}$$

with $L_{\rm E}$ being the Eddington luminosity. We use $M \approx 0.758\, M_\odot$ in practice. We shall argue in §2.4.2 that our failure to simulate a torus around a genuine supermassive black hole is completely superficial.

We now consider how M affects our choice of $\hat{c}$. The dynamical timescale is $[R_{\rm in}^3/(GM)]^{1/2}$, whereas the IR radiation diffusion timescale in the reduced speed of light approximation is $\rho_{\rm in} \bar{\kappa}_{\rm IR} (\frac{1}{2} R_{\rm in})^2/\hat{c}$, where $\rho_s uin$ is the gas density at the inner edge. Clean separation of dynamical evolution from IR radiation diffusion requires

$$\frac{\hat{c}}{(GM/R_{\rm in})^{1/2}} \gg \frac{1}{4} \rho_{\rm in} \bar{\kappa}_{\rm IR} R_{\rm in}; \tag{2.28}$$

the right-hand side is an overestimate by a factor of a couple because density falls off away from the inner edge. We settle on $\hat{c} \sim 50\, (GM/R_{\rm in})^{1/2}$ as a trade-off between accuracy and computational time (see §§3.1.4 and 4.1.3 for the actual value), although we find little qualitative difference even at $\hat{c} \approx 8.94\, (GM/R_{\rm in})^{1/2}$ as long as $v < \hat{c}$ everywhere.

2.4.2 Normalization

Physical quantities are hereafter normalized to their respective fiducial values. The fundamental fiducial quantities are the central mass M, the dust sublimation temperature $T_{\rm ds}$, and the Thomson scattering cross section per mass $\kappa_{\rm T}$; all other fiducial quantities, listed in Table 2.1, are derived from them. In particular, $L_{\rm E}$ is the Eddington luminosity, and r_0 is the distance where the effective temperature of the radiative flux in vacuum from a source with Eddington luminosity equals $\sqrt{2}$ times the dust sublimation temperature. Note that a system in which rotational support is provided by diffusive radiation must have $\rho_0 v_0^2/r_0 \sim E_0/r_0$.

One virtue of our normalization is that, because the characteristic length scale is $r_0 \propto M^{1/2}$, the gravitational acceleration at $r = r_0$ does not depend on M. We can guarantee accelerations due to gas pressure and radiation are likewise independent of M by fixing $c_{\rm s}/v_\phi$ and $L_{\rm UV}/L_{\rm E}$ for each simulation. These invariances ensure that the character of the dynamics simulated differs from that for more astrophysically relevant values

Table 2.1. Derived fiducial quantities.

Fiducial quantity	Symbol	Definition
luminosity	$L_{\rm E}$	$4\pi GMc/\kappa_{\rm T}$
length	r_0	$[L_{\rm E}/(4\pi c a_{\rm SB} T_{\rm ds}^4)]^{1/2}$
velocity	v_0	$(GM/r_0)^{1/2}$
time	t_0	$(GM/r_0^3)^{-1/2}$
gas density	ρ_0	$(\kappa_{\rm T} r_0)^{-1}$
gas pressure	p_0	$\rho_0 v_0^2 = a_{\rm SB} T_{\rm ds}^4$
magnetic field	B_0	$p_0^{1/2}$
radiation energy density	E_0	$L_{\rm E}/(4\pi r_0^2 c) = p_0$
radiative flux	F_0	cE_0

of M only in the magnitude of the timescale $t_0 \propto M^{1/4}$. The normalizations of other quantities, such as momentum density, could nevertheless vary with M.

Now that we have a system of normalization in place, we can translate our choice $M \approx 0.758\,M_\odot$ in §2.4.1 to dimensionless parameters that the simulation actually accepts, namely, $R_{\rm ideal} = 0.05 p_0/(\rho_0 T_{\rm ds})$ and $c \approx 2.70 \times 10^4\, v_0$.

2.4.3 Ambient material

Any initial condition of the torus puts mass within a limited region of the simulation domain. The exterior of that region is filled with isothermal and hydrostatic ambient material; we grant it nonzero orbital velocity because static ambient material is found to be numerically unstable. To determine the properties of the ambient material, we build upon the method used by Goldreich et al. (1986) for slender tori. The gravitational term of the force equation is clearly the gradient of some scalar field; if we stipulate polytropic gas and a power-law orbital velocity profile, then both pressure and centrifugal terms are gradients as well, and the force equation becomes an easily solvable algebraic equation. Unlike the solution of Goldreich et al. (1986), which is an expansion around some (R, z), our solution is exact. The density, pressure, and velocity given by our method assuming a polytropic index of unity are

$$\rho_{\rm amb}(R,z) \equiv \bar{\rho}_{\rm amb} \exp\left[\frac{GM}{r(c_{\rm s}^2)_{\rm amb}} + \frac{(v_\phi^2/c_{\rm s}^2)_{\rm amb}}{2-2q_{\rm amb}}\right], \tag{2.29}$$

$$p_{\rm amb}(R,z) \equiv \rho_{\rm amb}(R,z) \times (c_{\rm s}^2)_{\rm amb}, \tag{2.30}$$

$$\mathbf{v}_{\rm amb}(R) \equiv \left(\frac{GM}{R_{\rm amb}}\right)^{1/2} \left(\frac{R}{R_{\rm amb}}\right)^{1-q_{\rm amb}} \hat{\mathbf{e}}_\phi. \tag{2.31}$$

The length scale of the ambient material is set by $R_{\rm amb}$, while the other parameters are $(c_{\rm s}^2)_{\rm amb} = GM/R_{\rm amb}$ and $q_{\rm amb} = 1.75$. The shear parameter must satisfy $1.5 < q_{\rm amb} < 2$ in order that the ambient material have finite height and be stable. Since it is preferable that density and pressure vary monotonically across the torus boundary, we additionally require $\rho \geq \rho_{\rm amb}$ and $p \geq p_{\rm amb}$ everywhere in the initial condition.

2.4.4 Boundary conditions and numerical limits

Periodic hydrodynamic, magnetic, and radiative boundary conditions are adopted for the azimuthal direction, with the understanding that grid rays at one boundary must be rotated through $\pm\frac{1}{2}\pi$ before they can be copied to the ghost zones at the opposite boundary, to account for the fact that the simulation domain covers only a quarter of a circle (§3.1.4).

Outflow hydrodynamic and magnetic boundary conditions are applied at both boundaries in the radial and vertical directions. The value of $\mathbf{v}$ in the ghost zones is duplicated from the last physical cell, and components pointing into the simulation domain are zeroed. We then adjust ρ and p in the ghost zones at constant $c_s^2 \equiv p/\rho$ so that the pressure gradient exactly cancels the gravitational and centrifugal forces. The value of c_s^2 is the greater of p/ρ of the last physical cell and $(c_s^2)_{\rm amb}$; bounding c_s^2 from below protects ρ and p from numerical underflow. We zero the transverse components of the magnetic flux in the ghost zones and require the longitudinal component there to be divergence-free (Hawley & Krolik 2001).

Outflow radiative boundary conditions are used for the outer-radial and both vertical boundaries. For grid rays pointing away from the simulation domain, we copy their values of specific intensity from the last physical cell to the ghost zones; for all other grid rays, we set their values of specific intensity to zero. We also implement a cutout boundary condition for the inner-radial boundary. Ghost zones are filled out in the same way as an outflow boundary; on top of that, for every radially inward grid ray intersecting this boundary, we trace its trajectory across the cylindrical cutout to where it re-enters the domain, and add the specific intensity of the exiting grid ray to the corresponding grid ray in the ghost zone at the re-entry point without allowing for any time delay. Since the angle grid does not vary with coordinates, the matching of exiting to re-entering grid rays is exact. Grid rays re-entering at azimuthal coordinates outside the simulation domain are wrapped back after a suitable rotation.

Limits on gas density and temperature are enforced for the sake of numerical stability. We require that ρ satisfy $\rho \geq \rho_{\rm amb}$, and that T satisfy $10^{-3}\,T_{\rm ds} \leq T \leq 10\,(c_s^2)_{\rm amb}/R_{\rm ideal}$; if at any time ρ and T violate these conditions, we reset them to the nearest value within the acceptable range. The density floor guarantees a stable vacuum. A static pressure floor is unsatisfactory because pressure could hit the floor before density; any further drop in density would result in erroneous heating of the gas, making the overall time step unreasonably small. A better approach is to restrict temperature to within a generous range. Because $\kappa_{\rm IR,UV} \approx 0$ when $T \gg T_{\rm ds}$ (§2.3.6) and $R_{\rm ideal}T_{\rm ds} \ll (c_s^2)_{\rm amb}$ if the torus is supported by radiation pressure, radiative heating cannot bring the gas to the temperature ceiling.

CHAPTER 3

RADIATIVE HYDRODYNAMIC AGN TORI

Farewell sweet earth and northern sky,
for ever blest, since here did lie
and here with lissom limbs did run
beneath the Moon, beneath the Sun,
Lúthien Tinúviel
more fair than mortal tongue can tell.
Though all to ruin fell the world
and were dissolved and backward hurled
unmade into the old abyss,
yet were its making good, for this—
the dusk, the dawn, the earth, the sea—
that Lúthien for a time should be.

J.R.R. Tolkien, *The Silmarillion*

We present in this chapter RHD simulations of a dusty torus that experiences radiative acceleration on dust due to UV radiation from the central source and diffuse IR radiation in the torus. The reader is should revisit our conventions and terminology (Chapter 2), as well as the fiducial values used for normalization (Table 2.1)

3.1 Simulation setup

We describe details that are specific to this particular suite of simulations and therefore not covered in §2.4.

3.1.1 Initial condition

The initial condition is based on the analytic solution of an axisymmetric hydrostatic torus by Krolik (2007). To summarize, the radiation energy density inside the torus is determined along the mid-plane by

$$E^0_{\rm IR}(R,0) \equiv (E^0_{\rm IR})_{\rm in} + \frac{3GM\rho_{\rm in}}{R_{\rm in}}\left\{\frac{1}{1+\xi}\left[\left(\frac{R}{R_{\rm in}}\right)^{-(1+\xi)} - 1\right] - \frac{j^2_{\rm in}}{\xi}\left[\left(\frac{R}{R_{\rm in}}\right)^{-\xi} - 1\right]\right\}, \tag{3.1}$$

and everywhere else by the constant-$E^0_{\rm IR}$ contours

$$\frac{1}{2}\left(\frac{z}{R_{\rm in}}\right)^2 + \frac{1}{2}\left(\frac{R}{R_{\rm in}}\right)^2 - \frac{1}{3}j_{\rm in}^2\left(\frac{R}{R_{\rm in}}\right)^3 = \text{constant}. \tag{3.2}$$

Of the five free parameters, four pertain to quantities measured at the inner edge: radial coordinate $R_{\rm in}$, gas density $\rho_{\rm in}$, comoving IR radiation energy density $(E^0_{\rm IR})_{\rm in}$, and ratio of gas orbital to Keplerian velocity $j_{\rm in}$. The remaining free parameter is the radial power-law exponent ξ of gas density along the mid-plane. We distinguish between $E_{\rm IR}$ and $E^0_{\rm IR}$, the IR radiation energy density in the inertial and fluid frames respectively. Although the radiative initial condition inside the torus is fully specified by $E^0_{\rm IR}$, the procedure for assigning $I_{\rm IR}$ to individual grid rays is somewhat elaborate, and is therefore relegated to §3.1.2. Gas density inside the torus is given by

$$\rho(R,z) \equiv -\left[\frac{3GM}{R^2}\left(1 - j_{\rm in}^2\frac{R}{R_{\rm in}}\right)\right]^{-1}\frac{\partial E^0_{\rm IR}}{\partial R}; \tag{3.3}$$

in particular, $\rho(R,0) = \rho_{\rm in}(R/R_{\rm in})^{-\xi}$. Gas temperature and pressure are established by thermal equilibrium between gas and radiation, to wit, $E^0_{\rm IR} = a_{\rm SB}T^4$. Lastly, gas inside the torus has orbital velocity

$$\mathbf{v} \equiv j_{\rm in}\left(\frac{GM}{R_{\rm in}}\right)^{1/2}\hat{\mathbf{e}}_\phi; \tag{3.4}$$

in other words, $j/j_{\rm in} = (R/R_{\rm in})^{1/2}$, where $j \equiv v_\phi(R/GM)^{1/2}$. This velocity profile in fact applies to all hydrostatic radiation-supported tori in point-mass potentials (§3.1.3). The torus has extent $1 < R/R_{\rm in} < j_{\rm in}^{-2}$ and $z^2/R_{\rm in}^2 \leq \frac{1}{3}(j_{\rm in}^{-2} - 1)^2(2j_{\rm in}^2 + 1)$.

The free parameters are selected in a similar fashion to Krolik (2007). We pick $j_{\rm in} = \frac{1}{2}$ such that the inner edge is not supported by rotation alone, and that its vertical extent is comparable to its radial coordinate. Having

$$(E^0_{\rm IR})_{\rm in} = \frac{GM\rho_{\rm in}}{R_{\rm in}} \tag{3.5}$$

ensures IR and gravitational accelerations are comparable, that is, $\|\nabla E_{\rm IR}\|/\rho \sim GM/r^2$, although $(E^0_{\rm IR})_{\rm in}$ could take on any value as long as $E^0_{\rm IR} \geq 0$ inside the torus. The only deviation from Krolik (2007) is in our choice that $\xi = 1$, which results in a less massive torus.

The ambient material surrounding the torus was prescribed in §2.4.3. For our simulations, we set its length scale $R_{\rm amb}$ to be the center of the simulation domain, and its density scale to be $\bar{\rho}_{\rm amb} = 2\times10^{-8}\,\rho_{\rm in}$; it also has large enough sound speed to make it geometrically thick.

This initial condition is not an exact equilibrium since the central source may not be able to maintain the initial distribution of IR radiation energy density along the inner surface. It is not even intended to resemble the quasi-steady state of a realistic, axisymmetric, radiation-supported torus since its properties, such as its radial and vertical extent, can be arbitrarily altered by manipulating, say, the parameter $j_{\rm in}$. The initial condition is

merely an approximate analytic solution of a hydrostatic radiation-supported torus; as such, it is a convenient initial condition to employ.

3.1.2 IR initial condition

Because the time-dependent RT module of Athena operates on $I_{\rm IR}$ rather than $J_{\rm IR}$ and $\mathbf{H}_{\rm IR}$, we must convert $E^0_{\rm IR}$ provided by the initial condition to $I_{\rm IR}$. Inside the optically thick torus body, the IR specific intensity in the fluid frame can be found in the FLD approximation as (Levermore & Pomraning 1981)

$$I^0_{\rm IR}(\hat{\mathbf{n}}^0) \equiv \frac{c}{4\pi} E^0_{\rm IR}\, \mathcal{R}^{-1} (\coth \mathcal{R} - \hat{\mathbf{m}}^0 \cdot \hat{\mathbf{n}}^0)^{-1}; \tag{3.6}$$

it follows that

$$\mathbf{H}^0_{\rm IR} = \frac{c}{4\pi} E^0_{\rm IR} (\coth \mathcal{R} - \mathcal{R}^{-1})\, \hat{\mathbf{m}}^0. \tag{3.7}$$

Here $\mathcal{R} \equiv \|\nabla E^0_{\rm IR}\| / (\rho \kappa_{\rm IR} E^0_{\rm IR})$ is the Knudsen number for radiation diffusion, and $\hat{\mathbf{m}}^0 \equiv -\nabla E^0_{\rm IR} / \|\nabla E^0_{\rm IR}\|$. Geometrically speaking, if we draw arrows $\hat{\mathbf{n}}^0$ from the origin with lengths proportional to $I^0_{\rm IR}(\hat{\mathbf{n}}^0)$, the envelope is a prolate ellipsoid with ellipticity $\tanh \mathcal{R}$ and one focus at the origin. We impose the additional constraint that $0 \le \tanh \mathcal{R} \le 0.95$; the ceiling makes radiation less unidirectional in optically thin regions so that at least a few grid rays carry finite specific intensity. The specific intensity is then boosted to the inertial frame by

$$I_{\rm IR}(\hat{\mathbf{n}}) = I^0_{\rm IR}(\hat{\mathbf{n}}^0) \left[\frac{(1 - v^2/c^2)^{1/2}}{1 - \hat{\mathbf{n}} \cdot \mathbf{v}/c} \right]^4. \tag{3.8}$$

We remarked after Equation (2.5) that $I_{\rm IR}$ is a frequency-integrated quantity, which explains why the exponent is four, not three. Note that the FLD approximation is used merely to define the initial condition; it is not used to solve Equations (2.5) to (2.7).

3.1.3 Orbital velocity profile of a hydrostatic, radiation-supported torus

Curiously, all hydrostatic tori supported by IR radiation against the gravity of a point mass have the same orbital velocity profile. To see this, we write down the force balance in such a torus as

$$-\nabla\left(-\frac{GM}{r}\right) + \frac{\kappa_{\rm IR}}{c} \mathbf{F}_{\rm IR} + \frac{v_\phi^2}{R}\, \hat{\mathbf{e}}_R = \mathbf{0}. \tag{3.9}$$

The equation is solved together with the constraint of IR radiation energy conservation, $\nabla \cdot \mathbf{F}_{\rm IR} = 0$, and the assumption that $\kappa_{\rm IR}$ is not a strong function of position. A similar equation has been solved by Krolik (2007) under axisymmetry; here we adopt a more intuitive approach that leads us to the desired conclusion. Because the gravitational and radiative terms are both divergence-free, the same must also be true for $(v_\phi^2/R)\, \hat{\mathbf{e}}_R$. The

only radial and divergence-free vector field is $C(\phi, z) R^{-1}\, \hat{\mathbf{e}}_R$ for some function $C(\phi, z)$, hence v_ϕ is a constant over R. If we further restrict v_ϕ to be axisymmetric, we can write

$$v_\phi(R, z) = j_{\rm in}(z) \left(\frac{GM}{R_{\rm in}} \right)^{1/2}. \tag{3.10}$$

Here $j_{\rm in}(z)$ is some dimensionless function that measures the shortfall of orbital velocity at $R = R_{\rm in}$ from Keplerian as a consequence of radiative support, so we have $0 \le j_{\rm in} \le 1$.

3.1.4 Simulation parameters and simulation domain

It remains to pick the appropriate parameters for the simulations. To start with, we choose $0.10 \le L_{\rm UV}/L_{\rm E} \le 0.15$ in steps of 0.01 because these luminosities are high enough to hold back the infall of the torus, but low enough not to push it away too briskly. The simulation at each $L_{\rm UV}$ is run for about two orbits at the inner edge, at which point the radial component of velocity is positive throughout the torus body.

Three of the five parameters governing the initial condition have already been picked in §3.1.1; the remaining two will be given here. The inner edge $R_{\rm in}$ should be just outside the dust sublimation surface (e.g., Rees et al. 1969; Rieke & Lebofsky 1981; Barvainis 1987; Clavel et al. 1989; Sanders et al. 1989; Pier & Krolik 1993), that is, $R_{\rm in}^2 \gtrsim r_{\rm ds}^2 = \kappa_{\rm UV} L_{\rm UV}/(4\pi \kappa_{\rm IR} c a_{\rm SB} T_{\rm ds}^4)$. Our initial condition puts $R_{\rm in} = 0.8\, r_0$, so that $R_{\rm in}$ goes from $1.26\, r_{\rm ds}$ to $1.03\, r_{\rm ds}$ as $L_{\rm UV}/L_{\rm E}$ varies from 0.10 to 0.15. The reduced light speed introduced in §2.4.1 can be recast in terms of fiducial values as $\hat{c} = 50\, v_0$.

The density at the inner edge is selected to be $\rho_{\rm in} = \rho_0$. The radial Thomson optical depth of our initial condition along the mid-plane is

$$\int_{R_{\rm in}}^{\infty} dR\, \rho\, \kappa_{\rm T} = \rho_{\rm in} R_{\rm in} \kappa_{\rm T} \times \begin{cases} [j_{\rm in}^{-2(1-\xi)} - 1]/(1-\xi), & \xi \ne 1, \\ 2 \ln j_{\rm in}^{-1}, & \xi = 1, \end{cases} \tag{3.11}$$

while the vertical Thomson optical depth at $R = R_{\rm in}$ is

$$\int_{-\infty}^{\infty} dz\, \rho\, \kappa_{\rm T} = 2 \rho_{\rm in} R_{\rm in} \kappa_{\rm T} \int_1^{j_{\rm in}^{-2}} dx\, \frac{x^{-(2+\xi)} (1 - j_{\rm in}^2 x)}{(x^2 - \frac{2}{3} j_{\rm in}^2 x^3 - 1 + \frac{2}{3} j_{\rm in}^2)^{1/2}}. \tag{3.12}$$

Our parameters yield Thomson optical depths of ≈ 1.11 and ≈ 1.01 respectively, consistent with the observed range of values (e.g., Risaliti et al. 1999). The corresponding IR optical depths are established by numerical integration to be ≈ 19.9 and ≈ 10.9. The ratios of Thomson to IR optical depths are not $\kappa_{\rm T}/\bar{\kappa}_{\rm IR}$ due to the higher temperature and lower IR opacity near the inner edge.

The simulation domain spans $[0.3\, r_0, 5\, r_0] \times [-\frac{1}{4}\pi, \frac{1}{4}\pi] \times [-4\, r_0, 4\, r_0]$ in (R, ϕ, z). The vertical direction is made as tall as possible to capture escaping material, while not so tall that the centrifugal barrier would cause numerical problems at the inner-radial boundary. The number of grid cells is $188 \times 33 \times 320$ in (R, ϕ, z), and the number of grid rays per cell is 168.

3.2 Results

It is important to remember that the simulations do not reach steady state; therefore, what we report below is the transient response of the Krolik (2007) hydrostatic torus to UV irradiation. We already see within the first two orbits that the torus will never be hydrostatic for any $L_{\rm UV}$. This is because the degree of radiative support varies strongly with time and location (§3.2.1), because the inner surface is corrugated radially by radiation and sheared azimuthally by differential rotation (§3.2.2), and because mass is continually lost in the form of a radiation-driven wind from the inner surface (§§3.2.1 and 3.2.4). We do not claim our simulations represent the only possible configuration of a torus; instead, we wish to draw qualitative conclusions that apply to any flavor of smooth, radiation-supported torus, and to let this information guide us toward constructing a more realistic torus.

3.2.1 Qualitative description of gas motion

For the purpose of orientation, we begin by examining the evolution of the torus in general terms, using Figure 3.1 as reference. Parts of the simulation domain with $z < 0$ are discarded from our figures on the grounds that we observe no breaking of symmetry about the mid-plane.

UV radiation creates two immediate effects on the inner surface. Gas at the inner surface is swept up in the radially outward direction, forming a density concentration along it. The inner surface recedes as a result, first supersonically, then subsonically; this excites a transient in the form of an acoustic density perturbation peeling away from the density concentration and propagating outward through the torus, discernible at times $t \gtrsim 1$. The perturbation is shaped like a chevron bending outward when viewed with the full range of z.

More notably, UV radiation shaves off gas at high latitudes and creates a wind, while the central hole opens up from a cylindrical to a flaring shape. There are two reasons why this gas is the most vulnerable to UV stripping. First, we designate the UV optical depth from the central source by $\tau_{\rm UV}$. Only gas at $\tau_{\rm UV} \lesssim 1$ experiences substantial UV acceleration, and the $\tau_{\rm UV} = 1$ surface slants radially outward with increasing $|z|$ in the initial condition since ρ diminishes monotonically with $|z|$. Second, let us mentally divide the solid angle as seen from the origin into infinitely many sectors, and let us study the dynamics of the gas column contained within each sector with the proviso that neighboring columns do not interact. This is akin to the approach used by Roth et al. (2012) to calculate accelerations in their simulations. The acceleration of a column of thickness Δr due to point-source UV radiation is $\propto (1 - e^{-\rho\kappa_{\rm UV}\Delta r})/(\rho\Delta r)$, an expression that drops with increasing $\rho\Delta r$, while for any plausible initial condition of the torus, including ours (§3.1.1), $\rho\Delta r$ decreases with latitude. An intuitive way to think about the second argument is that UV radiative flux is spherically symmetric, and if it is capable of supporting an optically thick column against gravity at low latitudes, then it

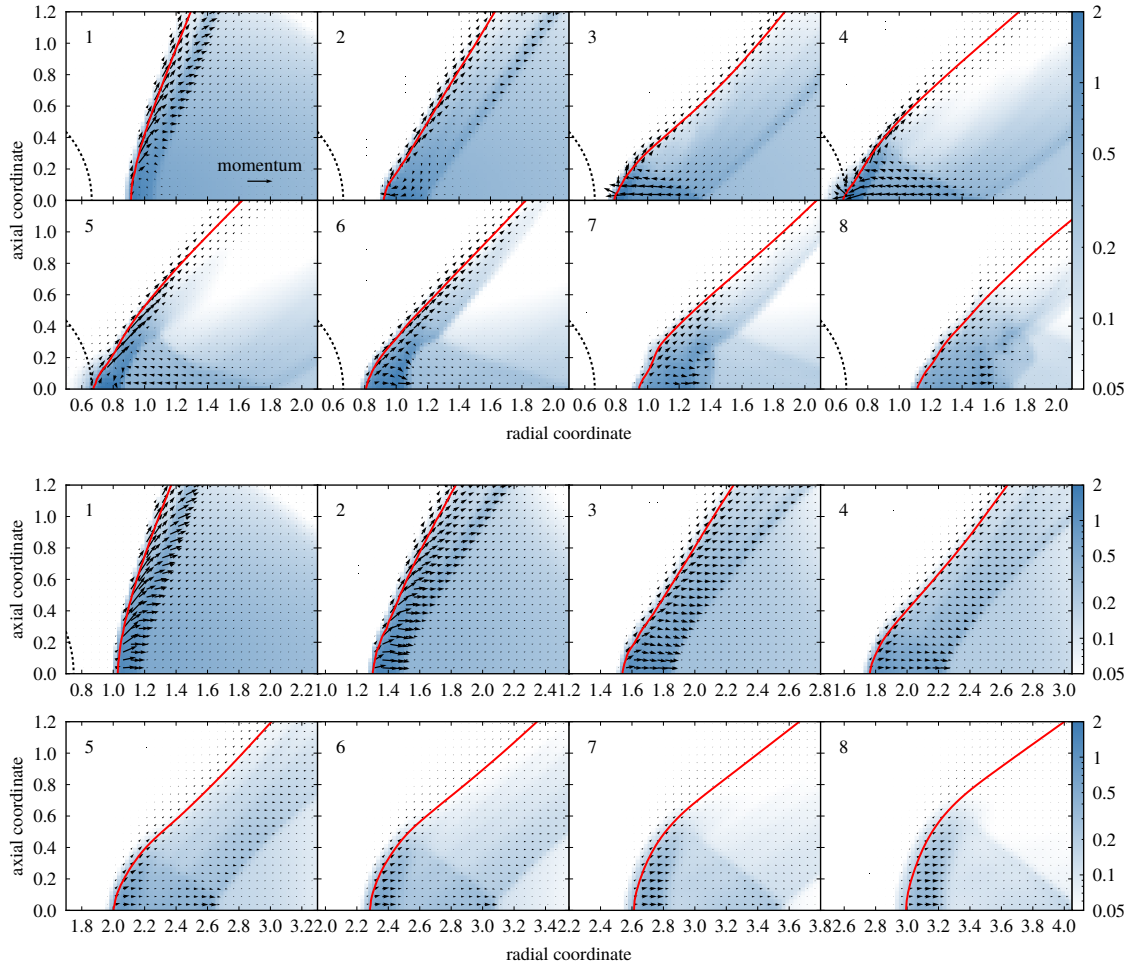

Figure 3.1. Zoom-in of the azimuthally averaged poloidal plane at times $t = nt_0$, where n is the number in the top-left corner of each panel. Gas density is presented on a logarithmic scale as blue intensities (see color bar along the right edge). The dust sublimation surface $r = r_{\rm ds}$ (§3.1.4) is the dotted black contour around the origin, and the red contour traces the surface on which $\tau_{\rm UV} = 1$. Gas momentum density is shown by arrows with lengths $\propto \rho v$; the arrow in the bottom-right corner of the first panel has length $0.5\ \rho_0 v_0$. All quantities are normalized to fiducial units (§2.4.2). *Top grid:* Plot of the $L_{\rm UV}/L_{\rm E} = 0.11$ simulation. *Bottom grid:* Plot of the $L_{\rm UV}/L_{\rm E} = 0.14$ simulation; note that the abscissa shifts at a constant rate toward the right from panel to panel.

is fully equipped to expel an optically thin column at high latitudes.

One might think that only gas at high latitudes participates in the wind, while gas at low latitudes accelerated by UV radiation is simply rammed against the inner surface. This is untrue because gas pressure along the flaring inner surface is virtually constant. At any height above the mid-plane, UV acceleration has a component parallel to the inner surface; unchecked by pressure gradients, this component is free to peel off gas into a wind gliding outward along the inner surface. Also note that, according to Equation (3.4), gas starting out from smaller R has smaller Rv_ϕ, so the wind preferentially removes gas with lower specific angular momentum.

Care must be exercised in reading Figure 3.1 after this initial phase. We shall see in §3.2.2 that the initially

axisymmetric inner surface becomes radially corrugated at $t \gtrsim 4\,t_0$. For $L_{\rm UV}/L_{\rm E} = 0.11$, averaging this undulating structure in the azimuthal direction produces the illusion that the inner surface at $t \gtrsim 6\,t_0$ resembles a thick shell while in fact the density concentration remains thin in any single poloidal slice. For $L_{\rm UV}/L_{\rm E} = 0.14$, the inner surface stays relatively axisymmetric; however, the fact that it moves radially outward almost as quickly as the transients excited along it gives it the appearance of multiple shells.

The radial motion subsequent to the initial phase depends on $L_{\rm UV}$, which determines the IR radiative flux across the torus. For $L_{\rm UV}/L_{\rm E} \geq 0.13$, IR radiative flux is strong enough that gas velocity is radially outward in the torus body almost all the time, hence there is little doubt the torus will be driven outward. In contrast, for $L_{\rm UV}/L_{\rm E} \leq 0.12$, a region develops above and below the mid-plane at greater radial coordinates than the inner edge in which the sum of the radial components of IR and centrifugal accelerations falls slightly short of counteracting gravity, and thus the radial component of velocity is negative. The size of this region decreases with $L_{\rm UV}$. Gas outside the region continues to be propelled outward, but gas inside slides slowly toward the mid-plane and inward; as it reaches the $\tau_{\rm UV} = 1$ surface, it is flung away by UV radiation. This kind of inflow–outflow is essentially a balance between the infall of gas toward the inner edge and the ability of UV radiation to clear out the pileup. Because there is only a finite amount of gas in the simulated torus, the inflow–outflow in our simulations cannot last forever.

The density distribution at times $t \gtrsim 4\,t_0$ bears little resemblance to the initial condition. Gas continues to be removed in the wind, but the detailed shape of the body depends on whether vertical support due to IR radiation is stronger or weaker than gravity. For $L_{\rm UV}/L_{\rm E} \geq 0.14$, IR radiative flux is sufficiently strong to inflate the body in the vertical direction. But for $L_{\rm UV}/L_{\rm E} \leq 0.13$, the body falls toward the mid-plane, reaching a thickness comparable to the gas pressure scale height, and then expands back vertically. The density concentration along the inner surface is shaped like another chevron and is taller than the body thanks to UV radiation constantly accelerating the gas upward and outward. Although the IR covering fraction drops steadily with time, the vertically extended inner surface and the wind keep it at a value higher than would be due to the body alone.

The degree of IR radiative support differs from place to place at these late times. For all $L_{\rm UV}$, IR vertical support in the chevron-shaped inner surface is generally insufficient to counteract gravity; as we move radially outward, we encounter a wedge-shaped, lower-density region in which marginal IR vertical support prevails, followed by another region of even lower density in which IR vertical support again falls short of gravity. As $L_{\rm UV}$ increases, IR vertical support becomes stronger more rapidly at the inner surface than further outward in the torus, such that the inner surface is completely supported against gravity at $L_{\rm UV}/L_{\rm E} = 0.15$ even when other parts of the torus are not.

Significant mass loss in the wind leads to a substantial drop in radial IR optical depth along the mid-plane

over time: By $t = 10\,t_0$, the optical depth is less than half its initial value for $L_{\rm UV}/L_{\rm E} = 0.10$, and down to ~ 0.05 times its initial value for $L_{\rm UV}/L_{\rm E} = 0.15$. This diminution in optical depth can be quite uneven as a function of azimuthal coordinate for $L_{\rm UV}/L_{\rm E}$ at the low end of the simulated range because, as we shall discuss in §3.2.2, those are the conditions in which the non-axisymmetric radial perturbation at the inner surface grows the most; at the high end of $L_{\rm UV}/L_{\rm E}$, axisymmetry is maintained much more closely.

The rate at which UV radiation deposits momentum in the torus is proportional to the UV covering fraction, whereas the mass of the torus is roughly proportional to the covering fraction times the optical depth; hence, the sharp plunge in IR optical depth explains why the body experiences progressively stronger radially outward acceleration. For $L_{\rm UV}/L_{\rm E} \leq 0.12$, this means the inflow–outflow eventually ceases, the radial component of velocity turns positive throughout the body, and the body slides outward more and more quickly as further mass loss accompanies its outward motion.

3.2.2 Radial perturbation of the torus inner surface

Another intriguing complication at $t \gtrsim 4\,t_0$ is the breaking of axisymmetry along the inner surface.

The three-dimensional structure of the inner surface stays remarkably vertical throughout the simulation for all $L_{\rm UV}$. Isosurfaces of constant density extend almost perpendicularly upward and downward from the mid-plane until they are cut off at some height. This height depends on the density at the isosurface, and typically increases with radial coordinate due to the flaring shape of the inner surface (§3.2.1).

The verticality of the inner surface allows us to focus our attention on the mid-plane, as we do in Figure 3.2. Non-axisymmetry along the mid-plane assumes the form of a slight radial perturbation of the inner edge going through three oscillations per quarter circle at $t \sim 4\,t_0$. The perturbation grows in amplitude afterward, and its behavior in the nonlinear regime depends on $L_{\rm UV}$.

The top circles illustrate how, for $L_{\rm UV}/L_{\rm E} \leq 0.11$, the originally smooth inner surface breaks up into dense, thin sheets overlapping in the azimuthal direction; seen along the mid-plane, the dominant sheets resemble trailing spiral density waves. For $L_{\rm UV}/L_{\rm E} = 0.11$, the three original oscillations combine into one at $t \sim 9\,t_0$; for $L_{\rm UV}/L_{\rm E} = 0.10$, the three oscillations merge into two at $t \sim 5\,t_0$ and break apart into three again at $t \sim 12\,t_0$.

In comparison, the bottom circles show that for $L_{\rm UV}/L_{\rm E} \geq 0.12$, the inner edge is characterized by a series of fingers pointing radially inward, connected at the outward end by arcs which are convex outward. The fingers are better described in three dimensions as vertical inward protrusions of the inner surface shaped like rounded flaps in poloidal section. The tips of the fingers and the middle portions of the arcs are slightly denser than other parts of the inner edge. The tips of the fingers are also sheared azimuthally into hooks by differential rotation. At any given time, the amplitude of the perturbation, as well as the azimuthal distortion

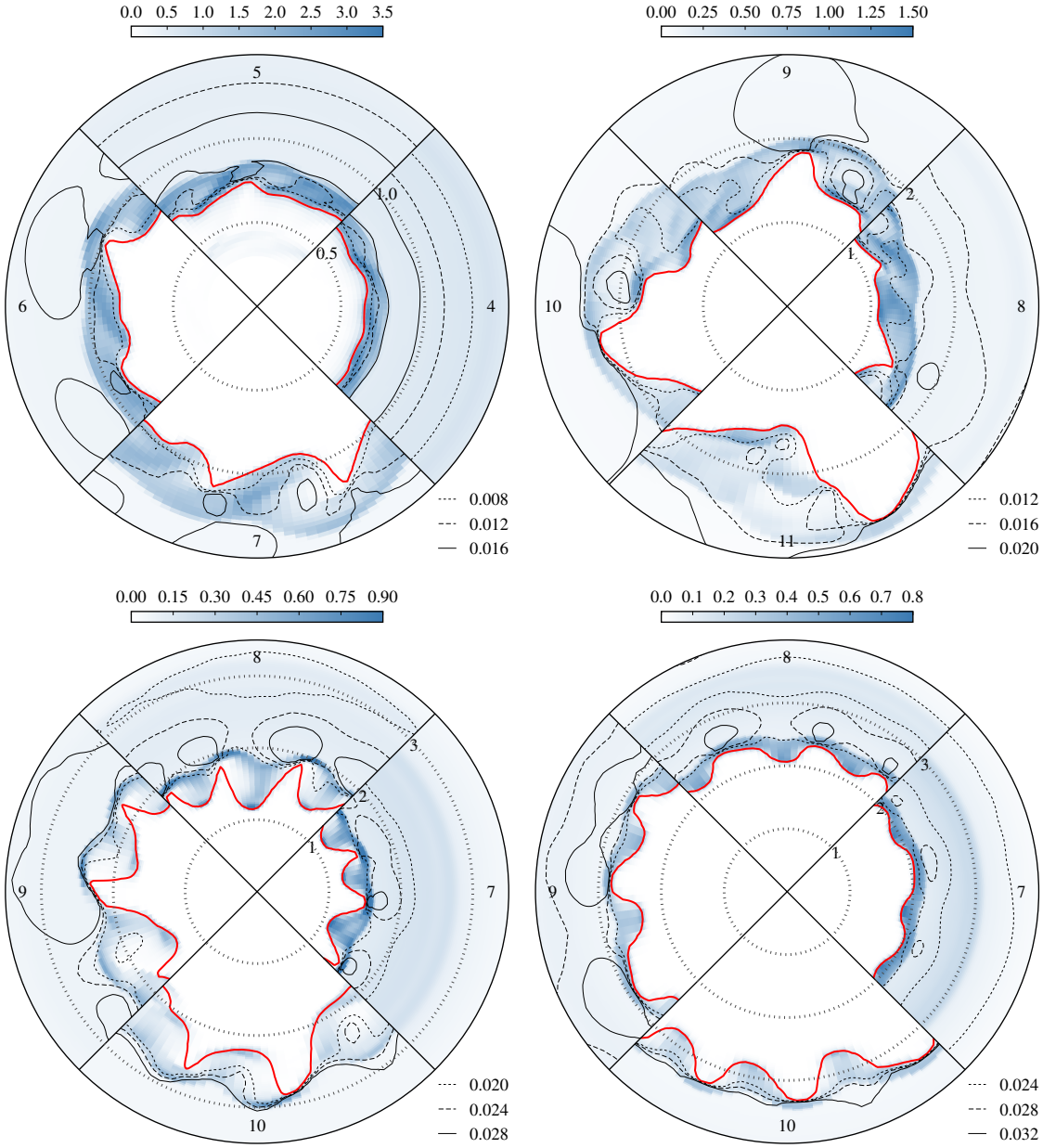

Figure 3.2. Mid-plane at times $t = nt_0$, where n is the number along the rim of each quadrant of the circles. Gas density is presented on a linear scale as blue intensities (see color bar above each circle), the red contour traces the surface on which $\tau_{\rm UV} = 1$, and the black contours display $R^2\,\hat{\mathbf{e}}_R \cdot \mathbf{F}_{\rm IR}$ at levels indicated in the legend. Orbital motion is counter-clockwise, all quantities are normalized to fiducial units (§2.4.2), and all circles have different scales. *Top circles:* Plots of the $L_{\rm UV}/L_{\rm E} = 0.11$ simulation. *Bottom-left circle:* Plot of the $L_{\rm UV}/L_{\rm E} = 0.12$ simulation. *Bottom-right circle:* Plot of the $L_{\rm UV}/L_{\rm E} = 0.13$ simulation.

of the fingers due to shearing, both decrease with $L_{\rm UV}$.

There is nothing physical about the number three in the number of oscillations at $t \sim 4\,t_0$. The initial perturbation is seeded by a small numerical artifact associated with the angle grid whose influence is the strongest at six azimuthal coordinates; the six originally tiny oscillations then merge to three easily discernible ones. Since the artifact is fixed in space while the orbital motion of the gas takes it across azimuthal coordinates, the artifact is not expected to act on the same gas packet continually; therefore, we believe the growing perturbation is a real effect.

3.2.3 Anisotropy of IR radiation

We now discuss the properties of IR radiation with the aid of Figure 3.3. Although the figure pertains to one snapshot of a single simulation, it is representative of the configuration of the torus at earlier times for all $L_{\rm UV}$.

The first thing we notice in the top panel is that gas and IR temperature contours coincide in the torus body, and diverge only in low-density regions outside the body. This confirms our expectation that thermal equilibrium holds deep inside the torus but not outside.

A more significant observation, verifiable by a quick inspection of the bottom panel, is that IR radiative flux streaming vertically through the central hole is stronger by a factor of a few than its nearly horizontal counterpart diffusing through the torus. This is explained by the conversion of UV radiation to IR taking place in a thin layer of thickness $\sim (\rho_{\rm in}\kappa_{\rm UV})^{-1}$ centered at $\tau_{\rm UV} = 1$. The IR optical depth is $\gg 1$ from there to the outer surface, but merely $\sim \kappa_{\rm IR}/\kappa_{\rm UV} \ll 1$ to the central hole; consequently, it is much easier for the freshly created IR radiation to head back into the central hole than to penetrate the body.

In a geometrically and optically thick torus, some of the IR radiation emitted by the inner edge can cross the central hole, reach the far side, and be absorbed again, giving IR radiation multiple chances at breaking into the torus. However, owing to the high optical depth of the torus, the probability per attempt that IR radiation can cross the entire torus is very small, so most of the IR radiation eventually leaves in the vertical direction after a few ricochets off the inner surface. Through this process, IR radiation transfers its momentum several times to a thin layer of gas at the inner surface.

This focusing of IR radiative flux into the vertical direction means $F_{\rm IR}/F_{\rm UV}$ rises gradually with r in the central hole, as seen in the bottom panel of Figure 3.3. A consequence is that although the wind is launched by UV radiation, IR radiation also contributes to its acceleration once it reaches altitudes comparable to the vertical extent of the torus.

We investigate $\mathbf{F}_{\rm IR}$ more quantitatively with Figure 3.4. The top panel displays $[L_{\rm UV}/(4\pi r^2)]^{-1}\,\hat{\mathbf{e}}_r\cdot\mathbf{F}_{\rm IR}$ for $L_{\rm UV}/L_{\rm E} = 0.11$ along sightlines emanating from the central source at various latitudes; this quantity would

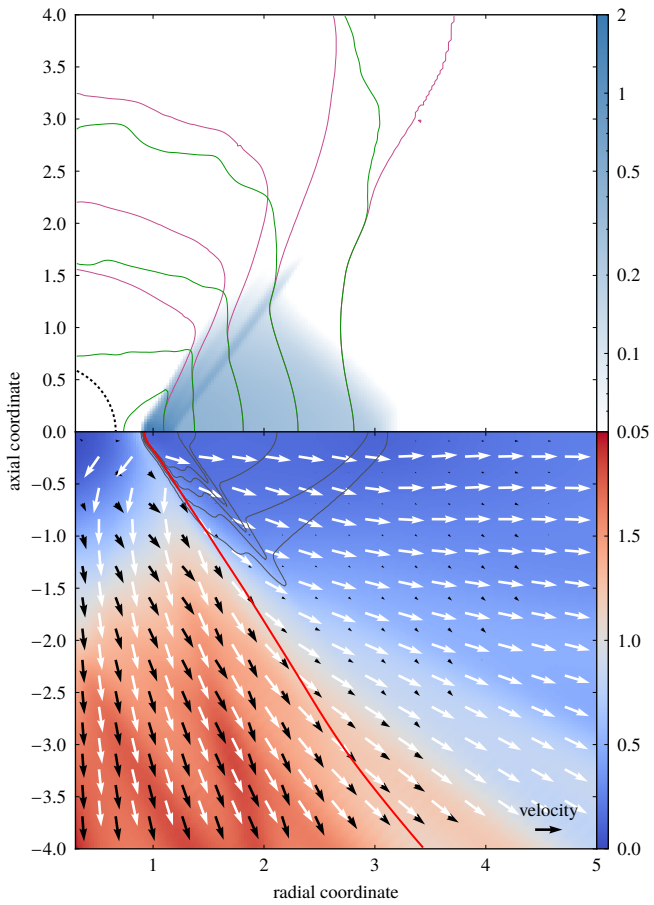

Figure 3.3. Azimuthally averaged poloidal plane of the $L_{\rm UV}/L_{\rm E} = 0.11$ simulation at time $t = 2\,t_0$, but extending farther than in the top grid of Figure 3.1. All quantities are normalized to fiducial units (§2.4.2). *Top panel:* Gas density is presented on a logarithmic scale as blue intensities (see color bar along the right edge). The dust sublimation surface $r = r_{\rm ds}$ (§3.1.4) is the dotted black contour around the origin. Purple and green contours respectively show gas and IR temperatures, both going from $0.3\,T_{\rm ds}$ to $0.7\,T_{\rm ds}$ in steps of $0.1\,T_{\rm ds}$ as one moves from the right to the left; to avoid confusion, contours not passing through the torus body are hidden. *Bottom panel:* The background colors display $[L_{\rm UV}/(4\pi r^2)]^{-1} F_{\rm IR}$ (see color bar along the right edge), which is unity for spherically symmetric radiation. The gray contours plot density rising from $0.1\,\rho_0$ on the outside to $0.5\,\rho_0$ on the inside in steps of $0.1\,\rho_0$. The $\tau_{\rm UV} = 1$ surface is traced by a red contour. The white and black arrows graph $\mathbf{F}_{\rm IR}/F_{\rm IR}$ and $\mathbf{v}$ respectively; the arrow in the bottom-right corner has length $5\,v_0$.

be unity if the IR radiative flux were spherically symmetric. The solid portions of the curves highlight the parts of the sightlines belonging to the torus proper. The sightlines are divided into two classes. Sightlines at low latitudes pass through the torus and have flux magnitudes below the spherically symmetric value. Conversely, sightlines at high latitudes lie completely within the central hole and have flux magnitudes above the spherically symmetric value; in fact, the curves appear to converge to $\sim C_{\rm IR}/(1 - C_{\rm IR})$ at large r, where $C_{\rm IR}$ is the IR covering fraction (§3.3.1). The increasing discrepancy from spherical symmetry toward the mid-plane illustrates the high degree of flux anisotropy.

The bottom panel of Figure 3.4 shows the angle between $\mathbf{F}_{\rm IR}$ and $\hat{\mathbf{e}}_r$. For sightlines at high latitudes, $\mathbf{F}_{\rm IR}$ is roughly parallel to $\hat{\mathbf{e}}_r$ everywhere; for sightlines at low latitudes, it is intriguing that the IR radiative flux snaps immediately to $\hat{\mathbf{e}}_r$ past the $\tau_{\rm UV} = 1$ surface. The fact that $\mathbf{F}_{\rm IR}$ is nearly aligned with $\hat{\mathbf{e}}_r$ in the body is all

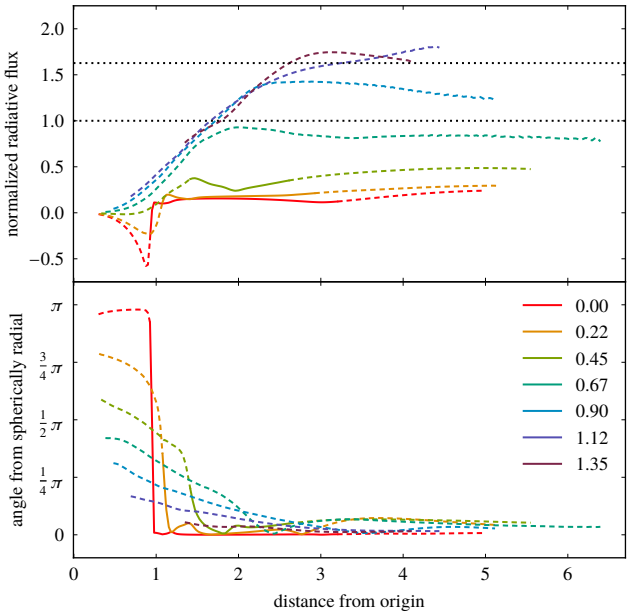

Figure 3.4. Azimuthally averaged IR radiative flux in the $L_{\rm UV}/L_{\rm E} = 0.11$ simulation at time $t = 2\,t_0$ measured along sightlines of latitudes indicated in the legend. The solid portion of each curve terminates at $\tau_{\rm UV} = 1$ on the left and $\rho = (\bar{\kappa}_{\rm IR}\, r_0)^{-1}$ on the right. All quantities are normalized to fiducial units (§2.4.2). *Top panel:* Plot of $[L_{\rm UV}/(4\pi r^2)]^{-1}\,\hat{\mathbf{e}}_r \cdot \mathbf{F}_{\rm IR}$; the upper and lower horizontal dotted lines are drawn at $C_{\rm IR}/(1 - C_{\rm IR})$ and 1. *Bottom panel:* Plot of $\arccos(\hat{\mathbf{e}}_r \cdot \mathbf{F}_{\rm IR}/F_{\rm IR})$.

the more striking considering that the IR optical depth from the inner edge to the outer surface in the vertical direction is a quarter that in the radial direction (§3.1.4).

Similar conclusions were also reached by Roth et al. (2012), who found that, for a smooth torus with geometrical thickness under a certain threshold, most of the bolometric radiative flux exits through the central hole while only a small fraction traverses the body. In addition, because $\mathbf{F}_{\rm UV} \propto \hat{\mathbf{e}}_r$ by definition, the bolometric radiative flux is likewise spherically radial except where $\mathbf{F}_{\rm IR}$ deviates most from spherically radial, that is, just inside the uppermost parts of the inner surface.

Roth et al. (2012) also stated that $F_{\rm IR} \propto r^{-2}$ at large r. The top panel of Figure 3.4 certainly suggests such a trend, especially for IR radiation beyond the outer surface. Nevertheless, since the radial coordinate ratio of the outer to inner edge is small, we cannot say with confidence if the inverse-square law holds inside the body. The situation is also complicated by the torus not being in a quasi-steady state.

3.2.4 Mass, momentum, and kinetic energy loss rates

It is natural to ask how much mass, momentum, and kinetic energy are carried away by the UV-launched wind mentioned in §3.2.1. The rate at which mass is evacuated allows us to determine the ultimate fate of the torus by balancing it against possible mass resupply. Moreover, we can connect the loss rates in our simulations with observations of AGN outflows.

We emphasize that the chevron-shaped transient (§3.2.1) is not the wind, and that the density concentration along the inner surface (§3.2.1) does not trace the trajectory of individual gas packets. Since the wind encompasses a large solid angle and density range, we have no reliable way of separating it from the torus body, which is moving radially outward at the same time along the mid-plane. In practice, we define the mass loss rate as

$$\dot{M} \equiv \int_{R=R_{\rm max},\,|z|>r_0} R\,d\phi\,dz\,\hat{\mathbf{e}}_R \cdot (\rho\mathbf{v}) - \int_{z=z_{\rm min}} R\,dR\,d\phi\,\hat{\mathbf{e}}_z \cdot (\rho\mathbf{v}) + \int_{z=z_{\rm max}} R\,dR\,d\phi\,\hat{\mathbf{e}}_z \cdot (\rho\mathbf{v}), \tag{3.13}$$

and the momentum and kinetic energy loss rates in a similar fashion; here $R_{\rm max}$ and $z_{\rm min,max}$ denote the coordinates of the boundaries of the simulation domain. We must be mindful to terminate our analysis before the IR half–opening angle becomes too large and the wind drops below $|z| = r_0$ at the outer-radial boundary, at $t \gtrsim 6\,t_0$. All loss rates derived from the simulations are implicitly quadrupled to account for our limited azimuthal extent (§3.1.4).

We begin with an analytic estimate of the mass loss rate. Supposing that the wind is propelled by UV momentum and reaches into $\tau_{\rm UV} \sim 1$, the mass loss rate may be estimated by either $\dot{M} \sim L_{\rm UV}/(cv_\infty)$ or

$$\dot{M} \sim 2\left(\frac{2\pi R_{\rm in}}{\rho_{\rm in}\kappa_{\rm UV}}\right)(\rho_{\rm in}v_\infty) = 4\pi\frac{R_{\rm in}v_\infty}{\kappa_{\rm UV}}. \tag{3.14}$$

These two estimates agree if the wind terminal speed is

$$v_\infty \equiv \left(\frac{GM}{R_{\rm in}}\frac{L_{\rm UV}}{L_{\rm E}}\frac{\kappa_{\rm UV}}{\kappa_{\rm T}}\right)^{1/2}. \tag{3.15}$$

It follows that

$$\dot{M} \sim 4\pi\left(\frac{GMR_{\rm in}}{\kappa_{\rm T}^2}\frac{L_{\rm UV}}{L_{\rm E}}\right)^{1/2}\left(\frac{\kappa_{\rm UV}}{\kappa_{\rm T}}\right)^{-1/2} \tag{3.16}$$

and

$$\frac{\dot{M}v_\infty^2}{L_{\rm UV}} = \frac{v_\infty}{c} = \left(\frac{GM}{c^2R_{\rm in}}\frac{L_{\rm UV}}{L_{\rm E}}\frac{\kappa_{\rm UV}}{\kappa_{\rm T}}\right)^{1/2}. \tag{3.17}$$

When appropriately rewritten, Equations (3.15) and (3.16) will also serve as the basis of our scaling relations for extrapolating our simulation results to more astrophysically relevant values of M and $\kappa_{\rm UV}$ (§3.3.3).

The top panel of Figure 3.5 demonstrates that, in keeping with this simple picture, the mass loss rates in our simulations normalized by $L_{\rm UV}/(cv_\infty)$ are of order unity and nearly the same for all $L_{\rm UV}/L_{\rm E}$ until $t \sim 4\,t_0$.

The middle panel traces the rate at which $\hat{\mathbf{e}}_r \cdot (\rho\mathbf{v})$, the spherically radial component of gas momentum, leaves the simulation domain; the normalization is $L_{\rm UV}/c$, the rate of momentum injection in the form of UV radiation. This quantity is about half for $t_0 \lesssim t \lesssim 4\,t_0$, suggesting that a sizable fraction of the radiation momentum is not transferred to the gas.

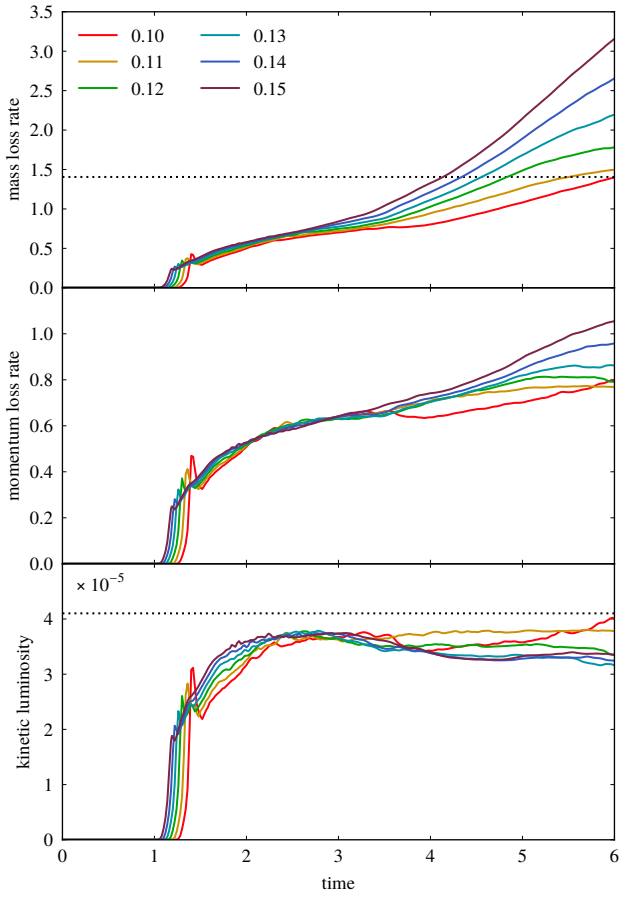

Figure 3.5. *Top panel:* Plot of the mass loss rate divided by $L_{\rm UV}/(cv_\infty)$, with v_∞ from Equation (3.15), for each value of $L_{\rm UV}/L_{\rm E}$ indicated in the legend. The dotted line shows the mass loss rate required to deplete an isolated torus within five orbits if $L_{\rm UV}/L_{\rm E} = 0.11$. *Middle panel:* Plot of the spherically radial gas momentum loss rate divided by $L_{\rm UV}/c$. *Bottom panel:* Plot of the ratio of kinetic to UV luminosity. The dotted line shows the value of $\frac{1}{3}(v_\infty/c)$ for $L_{\rm UV}/L_{\rm E} = 0.11$; the factor $\frac{1}{3}$ merely brings the line into the plot range and has no physical meaning. All quantities are normalized to fiducial units (§2.4.2).

We show in the bottom panel the ratio of kinetic to UV luminosity, where the kinetic luminosity is the loss rate of kinetic energy. Because $R_{\rm in} \propto M^{1/2}(L_{\rm UV}/L_{\rm E})^{1/2}$ (§3.1.4), Equation (3.17) predicts $\dot{M}v_\infty^2/L_{\rm UV} \propto M^{1/4}(L_{\rm UV}/L_{\rm E})^{1/4}$. The $L_{\rm UV}/L_{\rm E}$ scaling is undetectable in our results since our range of $L_{\rm UV}/L_{\rm E}$ spans a mere factor of 1.5; in fact, our ratio of kinetic to UV luminosity is effectively constant for all $L_{\rm UV}$ simulated, contrary to the $\propto L_{\rm UV}^{1.8}$ scaling offered by Roth et al. (2012). Moreover, our explicit value is $\sim 4 \times 10^{-3}$ times that of Roth et al. (2012), but this is largely because our M is $\sim 10^{-8}$ theirs and $\dot{M}v_\infty^2/L_{\rm UV} \propto M^{1/4}$.

3.3 Discussion

We now interpret our simulation results and generalize them to radiation-supported tori with different parameters.

3.3.1 Estimation of IR radiation energy density at the torus inner edge

The maximum of $E_{\rm IR}$ is attained at the inner edge because that is where UV radiation is reprocessed (§3.2.3). We can estimate the magnitude of the peak $(E_{\rm IR})_{\rm in}$ by considering the radiation energy balance at the inner edge:

$$C_{\rm UV}\frac{L_{\rm UV}}{4\pi R_{\rm in}^2}+C_{\rm IR}\,(F_{\rm IR}^-)_{\rm in}\approx(F_{\rm IR}^+)_{\rm in}. \tag{3.18}$$

We denote by $C_{\rm IR,UV}$ the IR and UV covering fractions. Similar to the two-stream approximation, we divide the radial component of the IR radiative flux into outward and inward parts, and we assign them to $F_{\rm IR}^{\pm}$ respectively. The second term on the left-hand side represents the part of the IR radiative flux leaking from the torus through the inner edge into the central hole, and then absorbed at the far side after crossing the hole.

Equation (3.18) relates five variables at fixed $L_{\rm UV}$ and is therefore difficult to verify against our simulations; two assumptions simplify it. The first one is $C_{\rm UV}\approx C_{\rm IR}$. The second one comes from observing that, for IR optical depth $\Delta\tau_{\rm IR}\gg 1$ and covering fraction $C_{\rm IR}\lesssim 1$, IR radiation propagates diffusively at $R>R_{\rm in}$, that is, $F_{\rm IR}^+ + F_{\rm IR}^-\approx cE_{\rm IR}\gg F_{\rm IR}^+ - F_{\rm IR}^-$, or $F_{\rm IR}^{\pm}\approx\frac{1}{2}cE_{\rm IR}$; we suppose this holds at $R=R_{\rm in}$ as well. Equation (3.18) then turns into

$$(E_{\rm IR})_{\rm in}\approx\frac{L_{\rm UV}}{4\pi R_{\rm in}^2 c}\frac{2C_{\rm IR}}{1-C_{\rm IR}}. \tag{3.19}$$

Our assumptions are not strictly correct because $C_{\rm UV}>C_{\rm IR}$, but their errors act in opposite directions in such a way that Equation (3.19) is still an excellent description of our simulations. The factor $C_{\rm IR}/(1-C_{\rm IR})$ is the number of scatterings IR radiation suffers at the inner surface prior to exit; $(E_{\rm IR})_{\rm in}$ goes up with $C_{\rm IR}$ because the torus traps IR more efficiently as $C_{\rm IR}$ approaches unity.

Figure 3.6 is a verification that, despite numerous simplifications, Equation (3.19) captures the physics well. In preparation of this figure, we construct the radial profile of $E_{\rm IR}$ by azimuthally averaging its mid-plane value; we then assign $(E_{\rm IR})_{\rm in}$ and $R_{\rm in}$ to the peak of the radial profile and its radial coordinate respectively. We measure $C_{\rm IR}$ by considering a tight cylindrical envelope of the simulation domain, and measuring the solid angle subtended at the origin by the parts of this envelope for which the IR optical depth toward the origin is greater than unity. The success of Equation (3.19) confirms the inner surface does act like a mirror to IR radiation.

Our study of the IR covering fraction leads to another useful result: We can predict the value of $L_{\rm UV}$ that marginally balances gravity in our initial condition (§3.1.1). Using Equations (3.5) and (3.19), we get

$$\frac{L_{\rm UV}}{L_{\rm E}}\approx\frac{\rho_{\rm in}}{\rho_0}\frac{R_{\rm in}}{r_0}\frac{1-C_{\rm IR}}{2C_{\rm IR}}. \tag{3.20}$$

The IR half–opening angle at $t=0$ is ≈ 0.727 rad; the estimate $L_{\rm UV}/L_{\rm E}\approx 0.135$ agrees with what we found in §3.2.1.

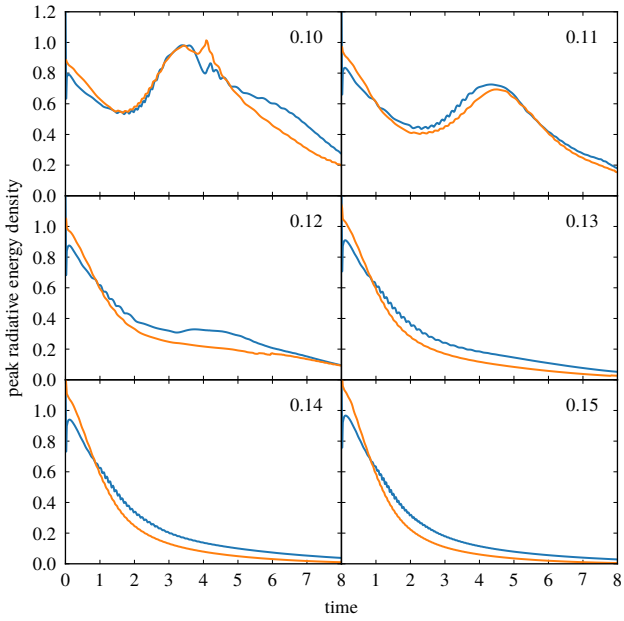

Figure 3.6. Plot of the left- and right-hand sides of Equation (3.19) in blue and orange curves respectively for each value of $L_{\rm UV}/L_{\rm E}$ indicated in the top-right corner of each panel. All quantities are normalized to fiducial units (§2.4.2).

3.3.2 Variation of simulation parameters

It is useful to extend beyond the tiny parameter space explored by our simulations. At fixed M, the principal parameters of the system are $L_{\rm UV}/L_{\rm E}$, as well as $\rho_{\rm in}$ and $j_{\rm in}$ in the initial condition (§3.1.1). We ignore detailed mass and angular momentum distributions, although interesting local effects may arise if we consider them fully. We also suppose the inner edge has temperatures near dust sublimation (e.g., Rees et al. 1969; Rieke & Lebofsky 1981; Barvainis 1987; Clavel et al. 1989; Sanders et al. 1989; Pier & Krolik 1993), so $R_{\rm in}$ is not a free parameter once M and $L_{\rm UV}/L_{\rm E}$ are given. All these parameters enter into the net acceleration

$$\mathbf{a} \equiv -\frac{GM}{r^2}\,\hat{\mathbf{e}}_r + j^2\frac{GM}{R^2}\,\hat{\mathbf{e}}_R + \frac{\kappa_{\rm IR}}{c}\mathbf{F}_{\rm IR} + \frac{\kappa_{\rm UV}}{c}\mathbf{F}_{\rm UV}, \tag{3.21}$$

which is a crucial factor governing torus dynamics. As far as global dynamics are concerned, it is essentially a poloidal vector with radial and vertical components $a_R \equiv \hat{\mathbf{e}}_R \cdot \mathbf{a}$ and $a_z \equiv (\operatorname{sign} z)\,\hat{\mathbf{e}}_z \cdot \mathbf{a}$.

Consider how each parameter affects a_R and a_z in the torus body. Clearly a_R increases with $j_{\rm in}$, while a_R and a_z increase with $L_{\rm UV}/L_{\rm E}$ through $\mathbf{F}_{\rm IR}$ and $\mathbf{F}_{\rm UV}$. The influence of $\rho_{\rm in}$ on a_R and a_z is subtler as it simultaneously controls $\Delta\tau_{\rm IR}$ and $C_{\rm IR}$, which play a role when $\Delta\tau_{\rm IR} \gtrsim 1$. On the one hand, greater $\Delta\tau_{\rm IR}$ reduces $F_{\rm IR}$ in the body according to $F_{\rm IR} \sim c(E_{\rm IR})_{\rm in}/\Delta\tau_{\rm IR}$; on the other hand, greater $C_{\rm IR}$ better traps IR radiation within the central hole, which at constant $L_{\rm UV}/L_{\rm E}$ raises $(E_{\rm IR})_{\rm in}$ (§3.3.1) and thus $F_{\rm IR}$ in the body. Both $\Delta\tau_{\rm IR}$ and $C_{\rm IR}$ rise with $\rho_{\rm in}$, so it is difficult to determine which effect dominates. In short, raising $j_{\rm in}$ increases radial support, raising $L_{\rm UV}/L_{\rm E}$ increases both radial and vertical support, whereas raising $\rho_{\rm in}$ has

an indeterminate effect on support.

We now turn to local effects that can appear at the inner surface. First, consider two tori with different $L_{\rm UV}/L_{\rm E}$ and $\rho_{\rm in}$ tuned so that they share $\mathbf{F}_{\rm IR}$ and $\mathbf{a}$ in the body. Dynamics in the body may be identical, but $\mathbf{F}_{\rm IR}$ in the central hole of the torus with greater $L_{\rm UV}/L_{\rm E}$ is necessarily stronger. Since Equations (3.15) and (3.16) show that v_∞ and $\dot{M}$ depend on $L_{\rm UV}/L_{\rm E}$ but not $\rho_{\rm in}$, this torus must host a faster wind than the other, as well as more severe losses of mass, momentum, and kinetic energy. Second, a sufficiently large increase in either $L_{\rm UV}/L_{\rm E}$ or $C_{\rm IR}$ could make $(E_{\rm IR})_{\rm in} \gtrsim a_{\rm SB} T_{\rm ds}^4$ and $\kappa_{\rm IR} \approx 0$ at the inner edge.

3.3.3 Scaling simulation results to more realistic parameters

As already remarked, for numerical reasons we adopt artificially reduced values of M and $\kappa_{\rm UV}/\kappa_{\rm IR}$. It is of course desirable to explore how the properties of our simulations might change if those two parameters were pushed to astrophysically realistic values.

The true opacity ratio should be $\sim 10^2$ to $\sim 10^3$ (e.g., Semenov et al. 2003), but since the essential requirement for capturing the physics is that the correct ordering of $\kappa_{\rm IR}$ and $\kappa_{\rm UV}$ be kept, we argue our simulations are undamaged by our reduced opacity ratio. To explore the effect of altering $\bar{\kappa}_{\rm UV}$, we have experimented with two simulations at twice the normal spatial resolution, one with the usual value of $\bar{\kappa}_{\rm UV}$, the other with twice the value. The inner surface recedes slightly faster and is sharper at higher $\bar{\kappa}_{\rm UV}$, but otherwise the overall evolution of the torus and its qualitative features are unaffected.

Nevertheless, quantitative results do vary with $\kappa_{\rm UV}$; in particular, care must be taken when scaling the wind terminal speed and mass loss rate found in §3.2.4. A higher value of $\kappa_{\rm UV}$ means the optically thin wind is faster but restricted to a thinner layer. Rewriting Equations (3.15) and (3.16) in terms of $R_{\rm in}/r_{\rm ds}$ highlights how this scaling should be performed:

$$v_\infty \sim (GM\kappa_{\rm T} a_{\rm SB} T_{\rm ds}^4)^{1/4} \left(\frac{L_{\rm UV}}{L_{\rm E}}\right)^{1/4} \left(\frac{\kappa_{\rm IR}\kappa_{\rm UV}}{\kappa_{\rm T}^2}\right)^{1/4} \left(\frac{R_{\rm in}}{r_{\rm ds}}\right)^{-1/2} \tag{3.22}$$

and

$$\dot{M} \sim 4\pi \left[\frac{(GM)^3}{\kappa_{\rm T}^5 a_{\rm SB} T_{\rm ds}^4}\right]^{1/4} \left(\frac{L_{\rm UV}}{L_{\rm E}}\right)^{3/4} \left(\frac{\kappa_{\rm IR}\kappa_{\rm UV}}{\kappa_{\rm T}^2}\right)^{-1/4} \left(\frac{R_{\rm in}}{r_{\rm ds}}\right)^{1/2}. \tag{3.23}$$

These forms cleanly separate the dependence on M and $\kappa_{\rm UV}$ from everything else.

Shifting the fiducial values of these parameters from those used in our simulations to more astrophysical numbers changes the wind terminal speed and mass loss rate found in our simulations to

$$v_\infty \sim 5000 \left(\frac{M}{10^7\,M_\odot}\right)^{1/4} \left(\frac{L_{\rm UV}/L_{\rm E}}{0.1}\right)^{1/4} \left(\frac{\kappa_{\rm IR}/\kappa_{\rm T}}{20}\right)^{1/4} \left(\frac{\kappa_{\rm UV}/\kappa_{\rm T}}{2000}\right)^{1/4} \left(\frac{R_{\rm in}}{r_{\rm ds}}\right)^{-1/2} {\rm km\,s^{-1}} \tag{3.24}$$

and

$$\dot{M} \sim 0.1 \left(\frac{M}{10^7\,M_\odot}\right)^{3/4} \left(\frac{L_{\rm UV}/L_{\rm E}}{0.1}\right)^{3/4} \left(\frac{\kappa_{\rm IR}/\kappa_{\rm T}}{20}\right)^{-1/4} \left(\frac{\kappa_{\rm UV}/\kappa_{\rm T}}{2000}\right)^{-1/4} \left(\frac{R_{\rm in}}{r_{\rm ds}}\right)^{1/2} M_\odot\,{\rm yr}^{-1}. \tag{3.25}$$

Outflows with speeds from $\sim 100\,\mathrm{km\,s^{-1}}$ to $\sim 2000\,\mathrm{km\,s^{-1}}$ have been identified in observations of X-ray warm absorbers (e.g., Kaastra et al. 2000; Kaspi et al. 2000) and UV absorbers (e.g., Anderson & Kraft 1969; Crenshaw et al. 1999) in Seyfert 1s. Mass loss rates inferred from X-ray warm absorbers go from $\sim 10^{-3}\,M_\odot\,\mathrm{yr^{-1}}$ to $\sim 10\,M_\odot\,\mathrm{yr^{-1}}$ (e.g., Blustin et al. 2005; Zhang et al. 2011), whereas studies of UV absorbers suggest a wider range of $\sim 10^{-4}\,M_\odot\,\mathrm{yr^{-1}}$ to $\sim 10\,M_\odot\,\mathrm{yr^{-1}}$ (Crenshaw & Kraemer 2012). These empirical results are roughly consistent with our fiducial values of v_∞ and $\dot{M}$.

The mass loss rate can be understood in a more intuitive fashion. The initial mass of the torus is $M_\mathrm{tor} \equiv C_\mathrm{tor} \times 2\pi\,\rho_\mathrm{in} R_\mathrm{in}^3$, where $C_\mathrm{tor} \approx 4$ for our initial condition (§3.1.1). We define the lifetime of the torus against mass loss in the radiation-driven wind as $t_\mathrm{tor} \equiv M_\mathrm{tor}/\dot{M}$; from Equation (3.16), we have

$$t_\mathrm{tor}\,\Omega_\mathrm{in} \sim \frac{1}{2} C_\mathrm{tor} (\tau_\mathrm{T}\,\tau_\mathrm{UV})_\mathrm{in}^{1/2} \left(\frac{L_\mathrm{UV}}{L_\mathrm{E}}\right)^{-1/2}. \tag{3.26}$$

In this equation, $\Omega_\mathrm{in} = (GM/R_\mathrm{in}^3)^{1/2}$ is the orbital frequency at the inner edge, and $(\tau_\mathrm{T,UV})_\mathrm{in} \equiv \rho_\mathrm{in} R_\mathrm{in} \kappa_\mathrm{T,UV}$ stand for Thomson and UV optical depths evaluated with inner-edge values. Our simulations have $(\tau_\mathrm{T})_\mathrm{in} \sim 0.8$, $(\tau_\mathrm{UV})_\mathrm{in} \sim 64$, and $0.10 \leq L_\mathrm{UV}/L_\mathrm{E} \leq 0.15$, so $t_\mathrm{tor}\,\Omega_\mathrm{in} \sim 42$. Our torus remains inside the simulation domain for a shorter amount of time because the torus body moves radially outward at late times (§3.2.1). Our Thomson optical depth may be reasonable for real AGNs, but our UV optical depth is too small by a factor of $\gtrsim 10$, so we expect the lifetime of realistic tori against mass loss to be $\gtrsim 3$ times longer.

3.3.4 Balance between radiation-driven mass loss and mass resupply

A salient feature of simulations for all L_UV is a radiation-driven wind from the inner surface (§3.2.1). The wind always has temperatures below T_ds since it lies outside of the dust sublimation surface. Depending on the geometry of the inner edge, the wind can be found at higher latitudes than the torus body; this enhances the covering fraction, and hints at a connection between the wind and dust observed in the polar regions of NGC 424 (Hönig et al. 2012) and NGC 3783 (Hönig et al. 2013).

The radiation-driven wind is distinct from the thermally driven wind (Begelman et al. 1983), which is launched when ionizing radiation heats the gas at the inner surface to the Compton temperature (Krolik et al. 1981). The wind is often discussed in connection with the torus (Krolik & Begelman 1986; Balsara & Krolik 1993; Krolik & Kriss 2001; Blustin et al. 2005); its mass loss rate is $\sim 0.4\,M_\odot\,\mathrm{yr^{-1}}$ (Krolik & Begelman 1986), similar to that of the radiation-driven wind found in Equation (3.25). The two winds could consequently augment each other despite their different physical properties.

The mass lost to these winds could be resupplied from the outside. A steady state could also obtain in which the IR optical depth across the body is approximately constant, so that the IR radiative flux does not become powerful enough to shove the body collectively outward (§3.2.1). A combined molecular and ionized

gas inflow rate of $\sim 0.2\,M_\odot\,\mathrm{yr}^{-1}$ has been observed down to ~ 40 pc in NGC 1097 (Fathi et al. 2013). Inflows of this magnitude at the outskirts of the torus suffice to replenish the mass loss given by Equation (3.25).

Magnetic effects can strongly influence the resupply rate. MHD turbulence stirred up by the MRI could lead to outward angular momentum transport through the torus and subsequent accretion toward the inner edge. The ideal MHD condition holds even at extremely low ionization fractions (Blaes & Balbus 1994; Gammie 1996), which can be maintained by X-rays (Neufeld & Maloney 1995) if they carry a sizeable fraction of the energy in the UV (e.g., Zamorani et al. 1981). Indeed, magnetic fields have been detected on $\lesssim 30$ pc scales in the nucleus of NGC 1068 (Lopez-Rodriguez et al. 2015).

Recall that the steady-state mass inflow timescale in a disk is $\sim [\alpha\,(H/R)^2\,\Omega]^{-1}$, where H/R and Ω are the aspect ratio and orbital frequency of the disk. Accretion driven by MHD stresses has $0.01 \lesssim \alpha \lesssim 0.1$, so the inflow timescale is quite close to the torus lifetime calculated in Equation (3.26) if, as here, $H/R \sim 1$. The relatively mild dependence of $t_{\rm tor}\,\Omega_{\rm in}$ on $L_{\rm UV}/L_{\rm E}$ suggests that equilibrium between inflow and outflow could be attained over a wide range of luminosities.

The presence of MHD stresses can redistribute angular momentum in the torus, altering the distribution of IR radiation needed to achieve radial force balance against gravity; this change could in turn affect whether the torus is vertically supported. Magnetic fields could also remove angular momentum altogether from the torus through a magnetized wind (Blandford & Payne 1982; Königl & Kartje 1994).

3.3.5 Radial perturbation of the torus inner surface

The nonlinear development of the radial perturbation of the inner surface (§3.2.2) is reminiscent of the classical Rayleigh–Taylor instability in hydrodynamics (Rayleigh 1883; Taylor 1950). For $L_{\rm UV}/L_{\rm E} \geq 0.12$, the emergence of fingers and arcs from an originally smooth inner surface is a hallmark of the instability. For $L_{\rm UV}/L_{\rm E} = 0.11$, the azimuthal wavenumber of the most prominent mode of the perturbation decreases as the development of the perturbation becomes nonlinear; this mirrors the classical picture in which the fastest-growing mode of the perturbation of the interface separating the two fluids shifts from high wavenumbers in the linear regime to low wavenumbers in the nonlinear regime (e.g., Garabedian 1957; Chang 1959).

Since radiation and not a physical fluid is supporting the gas against gravity, it is more accurate to compare our simulations with the radiative Rayleigh–Taylor instability (Krolik 1977; Mathews & Blumenthal 1977; Jacquet & Krumholz 2011; Jiang et al. 2013a). Figure 3.2 shows that in both linear and nonlinear regimes, wherever a part of the $\tau_{\rm UV} = 1$ surface is farther from the origin, the region immediately radially outward of it has greater $R^2\,\hat{\mathbf{e}}_R \cdot \mathbf{F}_{\rm IR}$ because the optical depth to the outer surface is smaller; the perturbation grows as a consequence. This mechanism is similar to what Krolik (1977) described. Nonetheless, the cylindrical

geometry of our simulations, as well as the presence of an acceleration gradient and differential rotation, complicates direct comparison with these previous analyses.

The amplification of the perturbation turns a smooth density distribution inhomogeneous; this kind of fragmentation process could provide a physical mechanism for the formation of dusty clumps often invoked to explain the observed broad $\sim 1\,\mu$m to $\sim 100\,\mu$m bump in the SED of AGNs (Nenkova et al. 2002, 2008b), the weak 9.7 μm silicate emission or absorption feature (Nenkova et al. 2002, 2008b; Hönig et al. 2006), and the gentle radial temperature profile of dust within the central parsec of Circinus (Tristram et al. 2007).

Radiation-driven clump formation has already been reported in FLD simulations of super-Eddington outflows from axisymmetric accretion disks (Takeuchi et al. 2013) and from two-dimensional planar atmospheres (Takeuchi et al. 2014) where the dominant source of opacity is electron scattering. Clumps in these simulations are irregular and typically one optical depth across. Anisotropic structures are likewise observed in our three-dimensional simulations employing genuine RT, but they have multiple characteristic length scales. Magnetic fields certainly exist in the torus (Lopez-Rodriguez et al. 2015) and could change how fragments are formed and destroyed, but we must leave its study to future work.

3.4 Summary

We have conducted three-dimensional, time-dependent RHD simulations of AGN tori in which gas and radiation are evolved simultaneously, and IR and UV radiative fluxes are not approximated using arbitrary closure prescriptions. The simulations reveal that a smooth, geometrically and Compton-thick torus is not very permeable to IR radiation, whereas the optically thin central hole allows IR radiation to escape immediately; therefore, the IR radiative flux is much stronger through the central hole than across the torus, and IR radiative support inside the torus is weaker than if the torus body were optically thin (§3.2.3). Meanwhile, IR radiation undergoing several reflections at the inner surface before leaving the central hole enhances the IR radiation energy density at the inner edge (§3.3.1) and reduces the luminosity needed to achieve marginal IR radiative support.

The inner surface experiences a spontaneous breaking of axisymmetry under radiation and differential rotation; the consequent radial perturbation amplifies rapidly with time (§3.2.2). The growth of the perturbation conjures up the picture of the radiative Rayleigh–Taylor instability, but with critical differences. The fragmentation of the inner surface alludes to a physical mechanism for the creation of clumps; however, the steady-state configuration of the fragments is not probed by our simulations and is likely affected by magnetic fields (§3.3.5).

Most importantly, a dusty wind can be launched from the inner surface by UV radiation and propelled

outward by a combination of IR and UV radiation. The appearance of this wind is inevitable in a torus with vertical density stratification (§3.2.1). High dust opacity in the UV, along with the concentration of IR radiative flux into the vertical direction (§3.2.3), means the wind likely experiences an acceleration well above gravity. The radiation-driven wind carries momentum comparable to that in UV radiation (§3.2.4). It is also a powerful mechanism of mass loss with the capacity to remove an isolated torus within ~ 20 orbital periods at the inner edge (§3.3.3).

Our study calls attention for the first time to the possibility that UV radiation pressure acting on dust can drive a wind with speed and mass loss rate of the same order as values inferred from observations (§3.3.3), and with mass loss rate similar to the better-known thermally driven wind (§3.3.4). In order to achieve an approximate steady state against mass loss through both kinds of winds, any such torus must be furnished with a new inventory of mass every ~ 20 orbital periods. The strong variation of radiative support throughout the body (§3.2.1), the existence of a radiation-driven wind (§§3.2.1 and 3.2.4), and the growth of perturbations along the inner surface (§3.2.2), demonstrate that the internal structures of tori are unlikely ever to achieve strict hydrostatic equilibrium.

CHAPTER 4

RADIATIVE MAGNETOHYDRODYNAMIC AGN TORI

> Heaven lasts, earth abides. Heaven and earth endures because they do not live for themselves; hence they can long live. Therefore the sage puts himself last and yet comes out first, cares little for himself and yet remains intact. Is it not because he is selfless that he can complete himself?
> Nothing is softer and weaker than water, yet when it assails the hard and strong, none can prevail against it, because it cannot be truly altered. Weak overcomes strong, soft overcomes hard: No one is unaware of this, but no one can put this into practice.
>
> Laozi, *Tao Te Ching*

We present in this chapter RMHD simulations of a magnetized dusty torus that experiences radiative acceleration on dust due to UV radiation from the central source and diffuse IR radiation in the torus. The reader is again reminded to review our conventions and terminology (Chapter 2), particularly the fiducial values used for normalization (Table 2.1).

4.1 Simulation setup

The basic design of our simulations was already specified in §2.4; here we describe settings on top of that foundation.

4.1.1 Simulation strategy

MHD turbulence stirred by the MRI saturates after several tens of orbits, but RMHD simulations are computationally prohibitively expensive on that timescale. One solution is to carry out the simulation in stages; in order of execution, they are the MHD stage, the UV-RMHD stage, and the IR-RMHD stage. Each stage is documented at length below.

4.1.1.1 MHD stage

In the MHD stage, we follow a geometrically thick, gas-supported torus in pure MHD to saturation. The rationale is that if IR radiation does behave like a pressure in optically thick regions, we should be able to replace gas pressure by IR pressure at a later stage with minimal changes to the geometry of the torus.

We construct the initial condition for the MHD stage in a fashion inspired by Goldreich et al. (1986). Assuming $\mathbf{v} = (GM/r_0)^{1/2}(R/r_0)^{1-q}\,\hat{\mathbf{e}}_\phi$ and $p = K\rho^\Gamma$, the density of an axisymmetric hydrostatic torus is uniquely given by

$$\text{constant} = \frac{GM}{r} + \frac{v_\phi^2}{2-2q} - \begin{cases} K\frac{\Gamma}{\Gamma-1}\rho^{\Gamma-1}, & \Gamma \neq 1, \\ K\ln\rho, & \Gamma = 1. \end{cases} \tag{4.1}$$

The free parameters of this initial condition are the shear parameter q, polytropic constant K, polytropic index Γ, and the constant on the left-hand side. The density maximum $\rho_{\max}$ is at $(R,z) = (r_0, 0)$. Note that we require $1.5 < q < 2$ for the torus to have finite height and be stable; indeed, geometrical thickness implies sub-Keplerian rotational profile. A geometrically thick torus with bounded radial and vertical extent can be obtained with $\rho_{\max} = \rho_0$, $q = 1.9$, $K = 0.2 p_0 \rho_0^{-\Gamma}$, and $\Gamma = 4$. The surface of the torus is $\rho(R,z) = 0$; solving this equation for $z = 0$ yields $R \approx 0.545\,r_0$ and $R \approx 4.72\,r_0$. The large dynamic range of specific angular momentum from the inner to outer edge gives the torus freedom to settle into a steady state through angular momentum redistribution.

Overlaid on the torus is a poloidal loop of magnetic field derived from the vector potential $\mathbf{A} \propto \max(\rho R^\xi - C\rho_0 r_0^\xi, 0)\,\hat{\mathbf{e}}_\phi$; we choose an exponent $\xi = 0.4$ so that the plasma betas at the inner and outer surfaces of the torus are similar, and a cutoff $C = 0.4$ so that all field lines are properly confined within the torus. The proportionality constant is selected to make the ratio of total gas pressure to total magnetic energy equal to 1000. Gas pressure is also perturbed at the 0.01 level to seed the MRI.

We already discussed how we set up the ambient material around the torus in §2.4.3; here we pick its length and density scales as $R_{\rm amb} = r_0$ and $\bar{\rho}_{\rm amb} = 10^{-5}\,\rho_0$ respectively. Additionally, the sound speed of the ambient material is equal to the orbital speed at $R = R_{\rm amb}$.

The configuration is evolved to $t = 200\,t_0$, at which point MHD turbulence has fully saturated, density reaches steady state, and gas pressure supports the geometrically thick structure. The mid-plane radial specific angular momentum profile is a broken power law; it is approximately $j(R) \propto R^{0.41}$ for $R \lesssim 2\,r_0$ and $j(R) \propto R^{0.25}$ for $R \gtrsim 2\,r_0$, with $j(R)$ being ≈ 0.81 times Keplerian at the break.

Transients develop during the MHD stage, spreading the torus outer edge radially outward at $t \gtrsim 40\,t_0$ and driving outflows through all boundaries, but eventually the torus stabilizes. To compensate for the mass loss, we multiply $\rho^{1/2}$, $p^{1/2}$, and $\mathbf{B}$ at the end of the MHD stage by the same factor everywhere, determined

as follows. The Thomson optical depth averaged over all sightlines contained within a mid-plane wedge of aspect ratio $m \ll 1$ is

$$\langle \tau_{\rm T} \rangle \approx \frac{(1+m^2)^{1/2}}{2m(\phi_{\rm max}-\phi_{\rm min})} \kappa_{\rm T} \int dV\ \rho r^{-2}\, \vartheta(mR-|z|), \tag{4.2}$$

where $\vartheta(\cdot)$ is the step function and $\phi_{\rm min,max}$ are the coordinates of the azimuthal boundaries of the simulation domain. The factor is chosen such that $\langle \tau_{\rm T} \rangle$ of a wedge with $m = 0.1$ matches some desired value, which we shall give in §4.1.1.3. The hydrodynamic variables are scaled in this fashion in order to preserve Equations (2.1) to (2.4).

4.1.1.2 UV-RMHD stage

We now switch over to RMHD. When the central source is turned on and radiation starts pushing on the gas at the inner surface, the torus is no longer in equilibrium. Since we would like a steady state, the simulation should be run long enough that any transients excited at the inner surface have time to propagate radially outward, away from the inner surface where the dynamics is the most interesting. This motivates us to introduce the UV-RMHD stage, in which we run the MHD solver with the UV RT module but not the IR RT module. The most expensive step of this RT module is ray-casting, which is performed just once before the simulation starts, thus the amortized cost is low. In addition to being a preprocessing step for the IR-RMHD stage, the UV-RMHD stage is also valuable for studying dynamics driven exclusively by UV radiation.

The UV RT module needs to be modified specifically for this stage. First, gas temperature in this stage is unsuitable for computing $\kappa_{\rm UV}$ with Equation (2.24) because gas temperature in a gas-supported torus is virial, whereas gas temperature in a realistic IR-supported torus reflects the balance between radiative absorption and re-emission. Since UV radiative acceleration is strong only in the central hole, we estimate what the gas temperature there may be in the IR-RMHD stage, use that expressly for $\kappa_{\rm UV}$ in the UV-RMHD stage, while keeping the actual gas temperature unchanged. Such an opacity temperature would be

$$T_{\rm op}(r) \equiv \left(\frac{\bar{\kappa}_{\rm UV} L_{\rm UV}}{4\pi \bar{\kappa}_{\rm IR} c a_{\rm SB} r^2} \right)^{1/4}, \tag{4.3}$$

where $\bar{\kappa}_{\rm IR}/\kappa_{\rm T} = 20$ and $\bar{\kappa}_{\rm UV}/\kappa_{\rm T} = 80$ (§2.3.6); now $\kappa_{\rm UV}$ is a function not of gas temperature, but of position. Second, the gas should convert most of the energy it receives from UV radiation to the IR, but since it cannot do so without the IR RT module, Equation (2.21) overestimates the energy actually imparted to the gas. The correct value of $S^{\rm e}_{\rm UV}$ should simply be the rate of work done by UV radiation, that is, $S^{\rm e}_{\rm UV} \equiv \mathbf{v} \cdot \mathbf{S}^{\rm m}_{\rm UV}$. Note that although Wada (2012) also considered the case where UV radiation deposits momentum, not energy, their energy equation does not include a similar term. Third, we assume gas velocity vanishes in Equation (2.22), thereby ignoring the minute effect of Lorentz transformation. Fourth, the time step is arbitrarily multiplied by 0.25 to account for the fact that $S^{\rm m}_{\rm UV} \gg GM\rho/r^2$ at $\tau_{\rm UV} \lesssim 1$.

We reset t to zero before the UV-RMHD stage begins; consequently, all times reported below are reckoned from the beginning of the stage.

4.1.1.3 Reduction of angular momentum in UV-RMHD stage

MHD stresses establish $j(R)$ in realistic tori. Simulating this process all the way to steady state is impossible in the IR-RMHD stage because of computational cost, and impossible in either the UV-RMHD stage or the IR-RMHD stage because MHD stresses redistribute angular momentum over tens of orbital periods while our choice of $\kappa_{\rm UV}$ prevents the torus from surviving this long against UV irradiation (§3.3.3). An approximate "steady" state may nonetheless be obtained in the UV-RMHD stage within reasonable time if we alter the output of the MHD stage before forwarding it to the UV-RMHD stage; for example, we could match $j(R)$ to an educated guess of its value in the UV-RMHD stage. Since UV radiation substitutes for rotation in radial support at the inner surface in the UV-RMHD stage, the steady-state $j(R)$ in that stage should lie below its equilibrium value in the MHD stage.

We can also see from an energy perspective why $j(R)$ should be reduced in our simulations. A realistic torus would be unbound by UV radiation doing positive work at its inner surface were there not a constant stream of gas toward the inner edge whose binding energy is higher than the average at the inner edge. Gas accretion through the torus is a consequence of angular momentum transport by MHD stresses, which, as argued above, is too slow to simulate, but we could emulate the long-term effects of inflow in our simulations by lowering $j(R)$ before the UV-RMHD stage.

Our purpose is to determine how $j(R)$ from the MHD stage should be depressed so as to put the torus in some lasting "steady" state in the UV-RMHD stage. Generally speaking, a torus in the UV-RMHD stage is in a "steady" state if its inner edge stays close to the dust sublimation surface and its morphology is qualitatively the same over time. The "steady" state ends when UV radiation causes radially outward recession of the inner edge and disruption of overall torus structure. The preceding paragraph suggests that a torus would have a long "steady" state if $j(R)$ at once raises the binding energy of gas at large distances and maintains a persistent flow of such gas toward the inner edge.

For ease of parameterization, we multiply $j(R)$ from the MHD stage by $\alpha\,(R/r_{\rm ds})^{-\beta}$, where $r_{\rm ds}$ is the dust sublimation radius (§3.1.4), $0 < \alpha \leq 1$, and $\beta \geq 0$. A parameter study decides the optimal values of α and β. While the computational cost of the UV-RMHD stage is merely a couple percent of the IR-RMHD stage, extensive sampling of the parameter space is still unfeasibly expensive; we therefore test 11 pairs of parameters, as shown in the left panel of Figure 4.1. All runs have the same gravitational potential energy $E_{\rm grav}$ at $t = 0$ but different kinetic energy $E_{\rm kin}$; consequently, a useful parameter is $b \equiv 1 + E_{\rm kin}/E_{\rm grav}$, the binding energy normalized to the negative of the gravitational potential energy. Conscious effort is expended

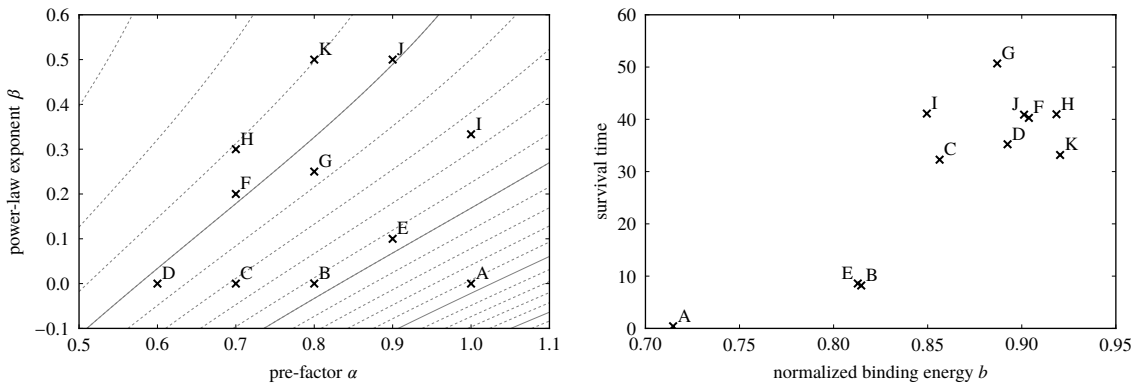

Figure 4.1. *Left panel:* Plot of pre-factor α and power-law exponent β that specify how $j(R)$ is modified before the UV-RMHD stage. Contours plot b, with solid contours at 0.6 to 0.9 from bottom-right to top-left in steps of 0.1. *Right panel:* Plot of survival time, normalized to fiducial units (§2.4.2), against b. See §4.1.1.3 for the definitions of $j(R)$, α, β, and b, and §4.2.2 for the definition of survival time.

to ensure each run has a value of b similar to that of at least one other run. We choose $\langle \tau_T \rangle = 1$ for the parameter study because this optical depth lies within the observed range (e.g., Risaliti et al. 1999), but its exact value is immaterial as long as the torus is optically thick to UV radiation. We shall demonstrate in §4.2.2 that $\alpha = 0.8$ and $\beta = 0.25$ grant the torus the longest "steady" state.

With parameters thus fixed, it remains to choose a snapshot of the UV-RMHD stage for passing on to the IR-RMHD stage. We impose two criteria on such snapshot. First, in the UV-RMHD stage, gas falls radially inward due to its decreased rotational support, then rebounds and relaxes upon encountering the centrifugal barrier. The infalling and relaxing regions are separated by an outward-propagating shock. A shock is clearly undesirable for a steady state, so a snapshot is eligible only if the shock has moved sufficiently far away from the inner surface. Second, to ensure that the torus would not be blown away immediately in the IR-RMHD stage, we stipulate that the torus survive in the UV-RMHD stage beyond the selected snapshot for two more orbits at the inner edge. A more massive torus is able to withstand UV irradiation longer, allowing ourselves greater freedom in picking a snapshot that obeys both requirements; therefore, we conduct yet another run in the UV-RMHD stage with the optimal α and β, but with $\langle \tau_T \rangle = 2$. The snapshot we opt for in the additional run is $t = 50\, t_0$.

This exercise provides us with a "steady"-state torus in the UV-RMHD stage; of course, there is no guarantee that it would remain so in the following IR-RMHD stage.

4.1.1.4 IR-RMHD stage

As we advance to the IR-RMHD stage, we reinstate IR radiative support by replacing gas pressure with a combination of gas and IR radiation pressure under thermal equilibrium; in other words, if the temperature

before and after the replacement are T_1 and T_2 respectively, and the isotropic IR specific intensity in the fluid frame after the replacement is I_2^0, then we demand $\rho R_{\rm ideal} T_1 = \rho R_{\rm ideal} T_2 + \frac{1}{3} a_{\rm SB} T_2^4$ and $a_{\rm SB} T_2^4 = (4\pi/c) I_2^0$. The degree to which gas pressure is replaced is quantified by $T_2/T_1 = [1 + \frac{1}{3} a_{\rm SB} T_2^4 / (\rho R_{\rm ideal} T_2)]^{-1}$; since $R_{\rm ideal} T_2 \sim c_{\rm s}^2$, and since $a_{\rm SB} T_2^4 \sim \rho v_\phi^2$ and $c_{\rm s}^2 \ll v_\phi^2$ if the torus is to be IR-supported and not gas-supported, we have $T_2/T_1 \sim c_{\rm s}^2/v_\phi^2 \ll 1$.

Several comments are in order. First, the replacement preserves pressure, not energy or momentum, because we are interested in how the torus is supported. Second, the replacement does not promise exact force balance in the inertial frame; in fact, considering that the gas pressure tensor in the fluid frame is isotropic while the IR pressure tensor in the same frame is ellipsoidal, there is no trivial transformation from one kind of pressure to another that would secure force balance everywhere. Third, the assumption that IR radiation pressure acts like a gas pressure is valid only in optically thick regions, so we are not justified to perform the replacement within the central hole; nevertheless, since the gas there is optically thin to the central source, the steady-state temperature profile quickly establishes itself no matter what the initial temperature is. Fourth, the magnetic field is untouched by the replacement; as we shall see in §4.2.3, this leads to small-scale pressure imbalance at the beginning. A smoother transition could be achieved in future work if pressure replacement happens over finite time with gradually increasing $c_{\rm s}/v_\phi$.

At the beginning of the stage, the radial Thomson and IR optical depths along the mid-plane are ≈ 1.59 and ≈ 23.1; the mass in the quarter-circle simulation domain (§4.1.3) is $\approx 8.83 \times \frac{1}{2}\pi\rho_0 r_0^3$, compared to $\approx 2.10 \times \frac{1}{2}\pi\rho_0 r_0^3$ for the initial condition of the RHD torus (§3.3.3). We again reset t to zero. Now that the torus is IR-supported, we enable both IR and UV RT modules and study whether it can self-consistently stay so. The simulation is conducted in this stage to $t = 14\,t_0$. The final radial Thomson and IR optical depths along the mid-plane are ≈ 2.34 and ≈ 37.9; radiation-driven mass loss results in a final mass of $\approx 6.62 \times \frac{1}{2}\pi\rho_0 r_0^3$.

4.1.2 Scaling properties

Let us examine the scaling properties of Equations (2.1) to (2.4) in the three stages. In the MHD stage, the radiative source terms are zero; if we adopt a system of normalization in which $v_0^2 = GM/r_0$, it is clear that the dimensionless equations are independent of M. The UV-RMHD stage introduces the UV radiative source terms in their modified forms (§4.1.1.2). Since the normalization of $\mathbf{S}^{\rm m}_{\rm UV}$ is $\rho_0 \kappa_{\rm T} E_0 = \rho_0 v_0^2/r_0$ (§2.4.2), and the normalization of $S^{\rm e}_{\rm UV}$ is v_0 times that, the dimensionless equations remain independent of M. This means we are not committed to a particular value of M in either stage, and we may simply scale our results as needed to match any M. In addition, there is effectively one velocity scale because $c_{\rm s}^2 \sim p_0/\rho_0 = v_0^2$ in geometrically thick tori.

The situation is very different in the IR-RMHD stage. The normalization of $\mathbf{S}^{\mathrm{m}}_{\mathrm{IR,UV}}$ is still $\rho_0 v_0^2/r_0$, but $\mathbf{S}^{\mathrm{m}}_{\mathrm{IR,UV}}$ has additional terms beyond zeroth order in v_0/c; worse still, the normalization of $S^{\mathrm{e}}_{\mathrm{IR,UV}}$ is now c/v_0 times that of $\mathbf{S}^{\mathrm{m}}_{\mathrm{IR,UV}}$. The introduction of a fixed velocity scale c therefore breaks scalability in all equations except Equation (2.1) and the leading order of Equation (2.2); put differently, the absence of c/v_0 in the dimensionless equations in the MHD and UV-RMHD stages is precisely the reason for their perfect scalability. Because $v_0^4 = GM\kappa_{\mathrm{T}} a_{\mathrm{SB}} T_{\mathrm{ds}}^4$, a choice of v_0/c is equivalent to a choice of M, which we already made in §2.4.1. A side remark is that a fixed dust sublimation temperature produces yet another independent velocity scale in the IR-RMHD stage, namely, $c_{\mathrm{s}}^2 \sim R_{\mathrm{ideal}} T_{\mathrm{ds}}$.

4.1.3 Simulation parameters and domain

The simulation domain spans $[0.3\,r_0, 9.9\,r_0] \times [-\frac{1}{4}\pi, \frac{1}{4}\pi] \times [-5\,r_0, 5\,r_0]$ in (R, ϕ, z) in all stages. A large radial extent is needed to capture the extended flow after the radial expansion of the torus in the MHD stage; the geometrical thickness of the torus demands a similarly large vertical extent. We pick the number of grid cells to be $480 \times 60 \times 500$ in (R, ϕ, z), large enough to resolve both MRI-driven turbulence (e.g., Hawley et al. 2013) and the UV absorption layer at the inner surface. The number of grid rays per cell is 168.

To facilitate comparison with our previous RHD simulations (Chapter 3), we choose $L_{\mathrm{UV}}/L_{\mathrm{E}} = 0.1$ for both UV-RMHD and IR-RMHD stages.

4.2 Results

We now present our observations on the UV-RMHD and IR-RMHD stages.

4.2.1 Overview of UV-RMHD stage

All runs in the UV-RMHD stage except run A are qualitatively similar. Here we highlight several features that facilitate comparison with the IR-RMHD stage, and we use an early snapshot of run G, displayed in the top row of Figure 4.2, to guide our discussion.

The torus quickly settles into the "steady" state defined in §4.1.1.3. Because rotation alone provides insufficient support against gravity, gas falls radially inward, converges toward the inner edge, and forms a lump, which is the structure at $R \lesssim r_0$ and $|z| \lesssim 0.3\,r_0$. UV radiation opens up the central hole as expected, but only weakly; all runs considered, the UV half–opening angle, or the angle between the axis and the $\tau_{\mathrm{UV}} = 1$ surface, finds equilibrium somewhere between ~ 0.24 rad and ~ 0.38 rad.

Wind launching by UV radiation from the inner edge is bursty. When a clump of gas is shot out from the inner edge, the upper part travels outward along the $\tau_{\mathrm{UV}} = 1$ surface, as expected for a gas packet accelerated

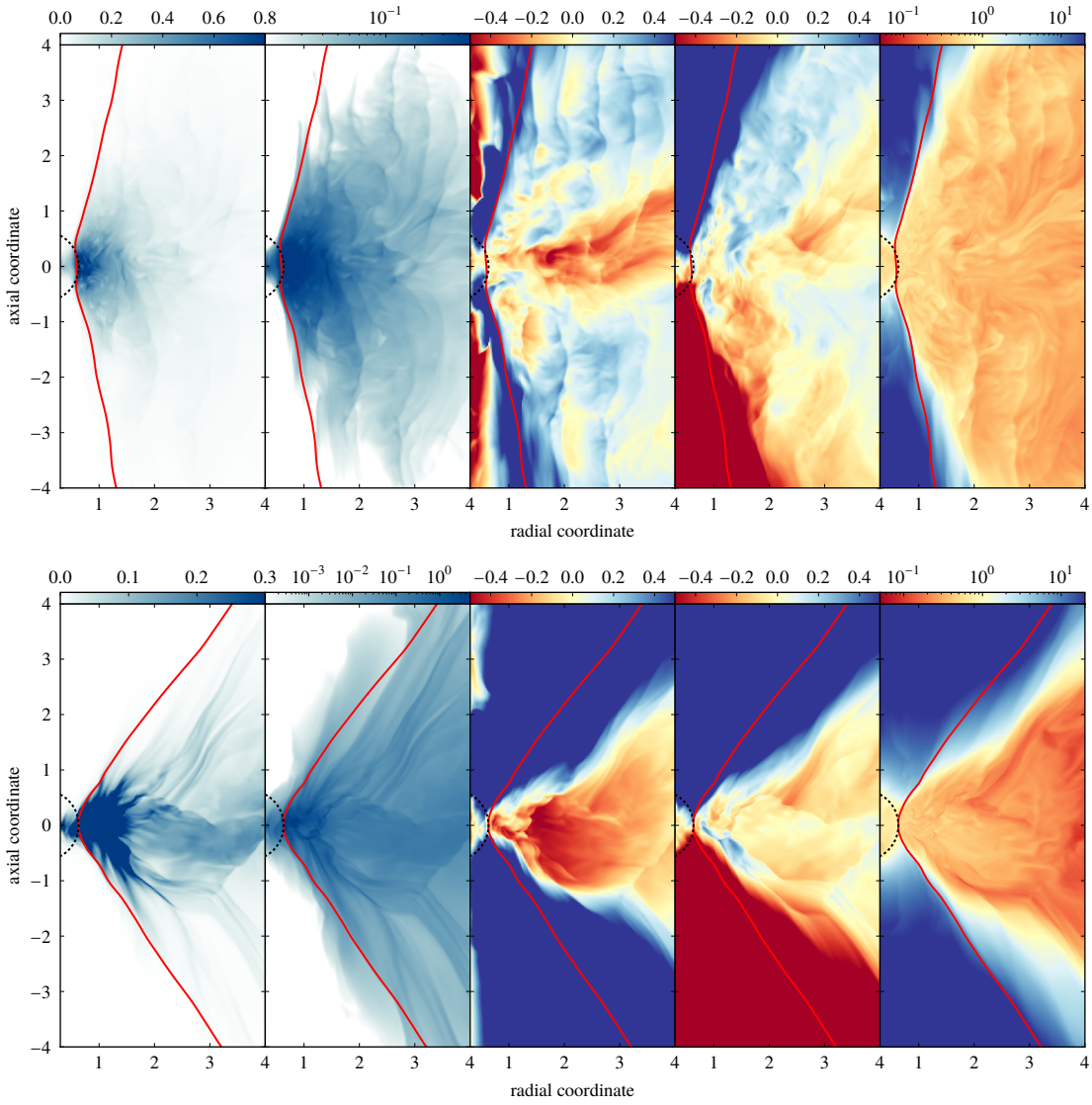

Figure 4.2. Zoom-in of the poloidal plane along $\phi = 0$. The dust sublimation surface $r = r_{\rm ds}$ (§3.1.4) is the dotted black contour around the origin, and the red contour traces the surface on which $\tau_{\rm UV} = 1$. All quantities are normalized to fiducial units (§2.4.2). *Top row:* Run G in the UV-RMHD stage at $t = 40\,t_0$. *Bottom row:* IR-RMHD stage at $t = 14\,t_0$. *First and second columns:* Gas density is presented on linear and logarithmic scales respectively as blue intensities (see color bars along the top edge). *Third to fifth columns:* Colors represent v_R, v_z, and $(GM\rho/r)^{-1}(\frac{1}{2}\rho v^2 + p)$ respectively (see color bars along the top edge).

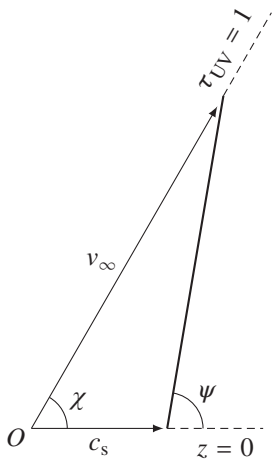

Figure 4.3. Schematic diagram of a vertical structure in poloidal section. A clump of gas is launched from the inner edge O; its upper and lower parts travel along the $\tau_{\rm UV} = 1$ surface and the mid-plane at speeds v_∞ and $c_{\rm s}$ respectively, forming the vertical structure marked by a thick line.

in a central hole that is optically thin to the UV. But the lower part is pushed horizontally outward beyond the $\tau_{\rm UV} = 1$ surface by centrifugal and UV radiative accelerations. The clump is stretched out, its upper and lower parts moving spherically and cylindrically radially outward respectively. The vertical structures at $|z|/R \gtrsim 0.5$ beyond the $\tau_{\rm UV} = 1$ surface are produced when an outgoing clump collides with the gas already present; these vertical structures are shocks and propagate outward at approximately sound speed. Vertical structures are found exclusively above a certain height because the lump stops outward motion at low latitudes.

The angle ψ between the vertical structures and the mid-plane is fixed by three parameters: the characteristic speed of the upper part, which is the wind terminal speed $v_\infty \sim (GM/r_{\rm ds})^{1/2}(L_{\rm UV}/L_{\rm E})^{1/2}(\bar{\kappa}_{\rm UV}/\kappa_{\rm T})^{1/2}$ (§3.2.4); the characteristic speed of the lower part, which is the sound speed $c_{\rm s} \sim (GM/r_{\rm ds})^{1/2}$ of the torus; and the angle that the $\tau_{\rm UV} = 1$ surface makes with the mid-plane, $\chi \sim 1.3\,{\rm rad}$. The description of vertical structures in the preceding paragraph inspires Figure 4.3; the angles in the figure are related by

$$\frac{v_\infty}{\sin(\pi - \psi)} \approx \frac{c_{\rm s}}{\sin(\psi - \chi)}. \tag{4.4}$$

For our parameters (§§2.3.6 and 4.1.3), we have $c_{\rm s}/v_\infty \approx 0.354$, so the solution to the equation is $\psi \approx 1.6\,{\rm rad}$. Vertical structures therefore deserve their name in our simulations, but they need not be vertical in simulations with different parameters.

Vertical structures are important because they represent a sizable portion of the outflow. The vertical structures have $v_r > 0$ even at $\tau_{\rm UV} \gg 1$; in fact, most of the mass outflow through the vertical boundaries in the "steady" state is at $\tau_{\rm UV} \gtrsim 1$. Furthermore, their immediate adjacency to infalling gas implies inflow and outflow could interact, or even regulate each other.

Figure 4.2 also shows $(GM\rho/r)^{-1}(\frac{1}{2}\rho v^2 + p)$, which is related to the Bernoulli constant; roughly speaking,

gas with this parameter below or above unity is gravitationally bound to or unbound from the system respectively. The vertical structures are bound, and UV radiation cannot unbind them since they are at $\tau_{\mathrm{UV}} \gtrsim 1$, so the outflow in the vertical structures is probably a failed wind.

4.2.2 Parameter study of reduction of angular momentum in UV-RMHD stage

The general behavior of the torus in the UV-RMHD stage was already described in §4.1.1.3: A "steady" state pertains to a torus with an inner edge near the dust sublimation surface, and the "steady" state expires when the inner edge detaches from the dust sublimation surface and moves radially outward. We define survival time as the length of the "steady" state, or more precisely, the time when the azimuthally averaged $\tau_{\mathrm{UV}} = 1$ surface intersects the mid-plane at $R = r_{\mathrm{ds}}$ for the last time; we use the last time because the position of the inner edge fluctuates at the beginning and its initial crossings of the dust sublimation surface are of little import.

We now return to the problem posed in §4.1.1.3 about how we can prolong survival by lowering $j(R)$. From the way we phrased the problem, it is unsurprising that survival time increases with b, as evidenced by the right panel of Figure 4.1. The exact form of $j(R)$ introduces some scatter, in that larger β may result in a longer survival time, but there is no strong indication of a preference for one form over another.

Because L_{UV} is constant across all runs, and because the UV covering fraction changes by at most a few percent over time and from run to run, the rate of UV momentum deposition also varies by a similar amount. We may therefore expect survival time to increase linearly with b, but that is not corroborated by the right panel of Figure 4.1. A plausible explanation is that the rate of work done by UV radiation is $\mathbf{v} \cdot (\rho \kappa_{\mathrm{UV}} \mathbf{F}_{\mathrm{UV}}/c)$, so halting infall in fact raises binding energy at a rate proportional to $-v_r$. A torus with lower $j(R)$ has decreased radial support and thus faster inflow, hence UV radiation is less effective in unbinding it.

The turnover at $b \gtrsim 0.9$ is because the angular momentum in runs H and K is so low that UV radiative acceleration cannot hinder gas contraction into the dust sublimation surface, and the position dependence of κ_{UV} means the gas faces little resistance as it rushes on through the inner-radial boundary. Whereas other runs lose mass in the "steady" state mostly through the vertical boundaries, runs H and K witness significant mass depletion across the inner-radial boundary at $t \lesssim 20\, t_0$. Although the infall would certainly be arrested as the gas meets the centrifugal barrier inside of our inner-radial boundary, and the resulting structure may very well have long survival times, it is much smaller than the dust sublimation surface and thus ineligible as a model for realistic tori. Consequently, runs of such high b are of no concern to us.

Of the remaining runs, run G stands out with the longest survival time; we therefore select its parameters for the additional run in the UV-RMHD stage that eventually goes on to the IR-RMHD stage. Incidentally, run G at $t = 0$ has approximately flat $j(R)$. Figure 4.4 shows that the profile stays flat in the mean throughout the

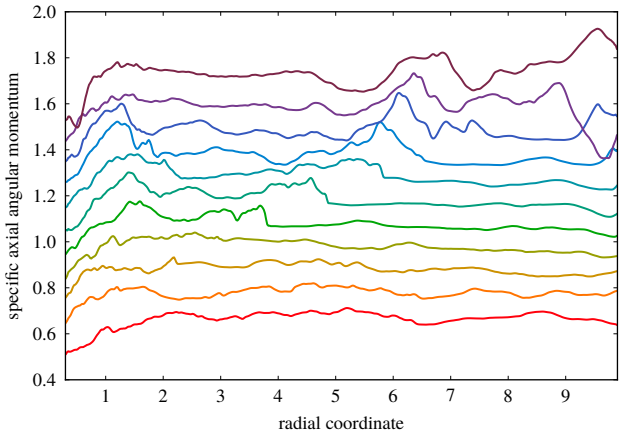

Figure 4.4. Plot of specific axial angular momentum, weighted by density and averaged azimuthally and vertically over $|z| \leq 0.5\,r_0$, against radial coordinate in run G in the UV-RMHD stage. The lines plot snapshots $5\,t_0$ apart, going from $t = 0$ at the bottom to $t = 50\,t_0$ at the top. Upward shifts of $0.1\,r_0 v_0$ per line are added for legibility. All quantities are normalized to fiducial units (§2.4.2).

UV-RMHD stage, but its increasing jaggedness implies that the torus is far from equilibrium. The last point simply reflects the short survival time compared to the angular momentum transport timescale.

The approaches taken in Chapter 3 and here are quite complementary. In the previous simulations, we fixed a sub-Keplerian $j(R)$ and found $L_{\rm UV}$ such that the torus is reasonably long-lived; our conclusion was that $L_{\rm UV}$ should be small to allow under-supported gas to flow toward the inner edge, but not so small that the gas collapses through the inner edge. In the current simulations, we decide on a constant $L_{\rm UV}$ and determine $j(R)$ that best promotes longevity of the torus. The lesson learned is that the torus can survive longer if $j(R)$ is reduced and gas feeds the inner edge, but there is a limit to how far we can go with this before the torus collapses to smaller than the dust sublimation radius.

4.2.3 Overview of IR-RMHD stage

When the IR RT module is enabled at the beginning the IR-RMHD stage, density immediately becomes more unevenly distributed; this is a direct consequence of our simulation strategy (§4.1.1). The torus in the MHD and UV-RMHD stages is characterized by density inhomogeneities with length scales much smaller than the torus itself: Cavities that have lower density and gas pressure but stronger magnetic field are in pressure equilibrium with surrounding walls that have higher density and gas pressure but weaker magnetic field. Before the IR-RMHD stage, gas pressure is exchanged for IR radiation pressure (§4.1.1.4). Both cavities and walls are optically thin to the IR due to their small size, so IR radiation can easily leak out from the walls into the cavities and form a smooth distribution. This happens over a timescale much shorter than the IR radiation diffusion timescale across the entire torus, which in turn is much smaller than the dynamical timescale. The initial pressure equilibrium is destroyed; the cavities, now overpressured, expand slightly and compress the en-

closing walls, making the latter resemble thin filaments in section. The density inhomogeneities are smoothed out when gas and magnetic field reach pressure equilibrium again, at $t \sim t_0$. With decreasing c_s/v_ϕ, more gas pressure is converted to IR radiation pressure, and the filaments become thinner; our simulation strategy is therefore limited to c_s/v_ϕ for which the filaments remain at least one cell thick.

The central hole opens up quite dramatically, in contrast to the UV-RMHD stage. The difference can be explained by considering radial force balance in the plane defined by, say, $z \sim 3\,r_0$, around where it intersects the $\tau_{UV} = 1$ surface; the locus of intersection varies with time, but is generally bounded within $0.5\,r_0 \lesssim R \lesssim r_0$. In the UV-RMHD stage, an approximate balance obtains at $R \lesssim 2\,r_0$ between radially outward centrifugal and UV radiative accelerations, inward gravitational acceleration, and largely inward gas pressure acceleration. Gravitational and UV radiative accelerations play minor roles here because their radial components, which are $\propto R/(R^2+z^2)^{3/2}$, peak at $|z|/R = \sqrt{2}$ for any given $|z|$, but $|z|/R \gg \sqrt{2}$ for the situation under discussion. Before the IR-RMHD stage, most of the gas pressure is swapped for IR radiation pressure. An inward acceleration is accordingly removed, but it is not replaced because IR radiative flux diffuses outward from $\tau_{UV} \lesssim 1$; centrifugal acceleration is no longer opposed, so the central hole widens. As the UV half–opening angle increases, the radial component of UV radiative acceleration at $\tau_{UV} \sim 1$ becomes stronger, hence UV radiation begins to participate in expanding the central hole as well.

Similar to the case of pure RHD (§3.2.1), we observe a strong chevron-shaped transient propagating radially outward from the inner surface as the central hole opens up. The transient can be regarded as dividing the torus into two parts: The gas outside has not fully responded to the change induced by turning on the IR RT module, whereas the gas inside has undergone at least partial relaxation.

The torus achieves a "steady" state at $t \gtrsim 6\,t_0$ that lasts until the end of the simulation; in contrast, the tori in previous simulations were shredded apart by UV radiation within two orbits at the inner edge (§3.2.1). The RHD and RMHD simulations have central sources with almost the same luminosity, and tori with inner edges at similar positions; consequently, the mass loss and kinetic energy change rates differ little between the two sets of simulations. The qualitative change in torus behavior is attributed to the current torus having $\gtrsim 4$ times the mass of previous ones (§4.1.1.4), as well as $\approx 3\,\%$ higher specific binding energy. If we assume the average mass loss rate in the "steady" state, we would expect this new torus to survive for ≈ 21 orbits.

The transient continues to move radially outward in the "steady" state; meanwhile, four structures with distinctive and persistent morphologies emerge in the region between the $\tau_{UV} = 1$ surface and the transient. The bottom row of Figure 4.2 portrays the torus at a time when the transient has left the plotted volume entirely; the structures are most recognizable in the first and second panels, but the other panels are also useful for demarcating one structure from another. We discussed one structure before in the context of RHD simulations, namely, the UV-launched wind at $\tau_{UV} \lesssim 1$. Three additional structures can be identified at $\tau_{UV} \gtrsim 1$ thanks

to the torus being in "steady" state: the very dense region enclosed by $0.6\,r_0 \lesssim R \lesssim 1.4\,r_0$ and $|z| \lesssim 0.3\,r_0$, which we call the head; the somewhat less dense region at $1.3\,r_0 \lesssim R \lesssim 4.2\,r_0$ and $-0.6\,r_0 \lesssim z \lesssim 0.4\,r_0$, which we call the body; and the structures parallel to the $\tau_{\rm UV} = 1$ surface at $\tau_{\rm UV} \gtrsim 1$ and $|z| \gtrsim 0.5\,r_0$, which we call the wings. The body does not lie entirely along the mid-plane because MHD turbulence breaks the symmetry about it. The head is denser than the lump in the UV-RMHD stage by a factor of ~ 2; although the head and the body are the densest parts of the torus, they take up $\lesssim 30\,\%$ of the total mass owing to their small volumes.

Figure 4.5 shows the flow pattern in the torus. Although the torus is asymmetric about the mid-plane throughout the simulation, it must on average be symmetric in the long run; therefore, we vertically symmetrize each quantity in the figure by averaging the quantity with its reflection about the mid-plane. We also smooth out fluctuations by averaging over the interval $6\,t_0 \le t \le 14\,t_0$ in which the torus is in "steady" state. Note that the region at $R \gtrsim 6\,r_0$ and $|z| \lesssim 3.5\,r_0$ should be disregarded because gas there has yet to reach equilibrium. The four structures named in the preceding paragraph are manifestly not hydrostatic; rather, gas from $3\,r_0 \lesssim R \lesssim 6\,r_0$ and $r_0 \lesssim |z| \lesssim 2\,r_0$ migrates to the body, then to the head, and finally to the wind or the wings; we shall examine this process more closely in §4.2.4, when we discuss forces. The structures are recognizable during the entire "steady" state because they retain qualitatively similar shapes even as gas passes through them.

Although the torus is already in "steady" state, the wind is still launched in bursts because density is not smoothly distributed at the inner edge of the head. This gives rise to the complex density structure at $\tau_{\rm UV} \lesssim 1$. Since the position of the $\tau_{\rm UV} = 1$ surface is easily influenced by the presence of trace amounts of dusty gas in the central hole, the "steady"-state UV half–opening angle fluctuates between ≈ 0.60 rad and ≈ 0.71 rad at $t \gtrsim 6\,t_0$. The average angle is tantalizingly close to $\arctan(1/\sqrt{2}) \approx 0.62$ rad. We speculate this is because the cylindrically radial component of UV radiative acceleration attains its maximum in any horizontal slice at $|z|/R = \sqrt{2}$. The $\tau_{\rm UV} = 1$ surface is not precisely conical, by which we mean there does not exist a spherically radial ray from the origin to which the poloidal section of the time- and azimuthally averaged $\tau_{\rm UV} = 1$ surface is asymptotic, despite its extremely straight appearance in Figure 4.2.

The inner surface is corrugated in the azimuthal direction, similar to pure RHD simulations (§3.2.2). While the radial span of the perturbation increased rapidly in our RHD simulations, it remains within $0.62\,r_0 \lesssim R \lesssim 0.75\,r_0$ in the "steady" state of the IR-RMHD stage of our RMHD simulations. This difference could be because the perturbation grows only after the "steady" state, when the inner edge separates from the dust sublimation surface and moves radially outward, but we do not simulate the torus for long enough in the IR-RMHD stage to witness this phase of torus evolution. However, we do follow tori in the UV-RMHD stage until the "steady" state unambiguously ends (§4.2.2), and in every run, the perturbation grows substantially only after outward recession has started. Based on this evidence, we hypothesize that if realistic tori could maintain a true steady

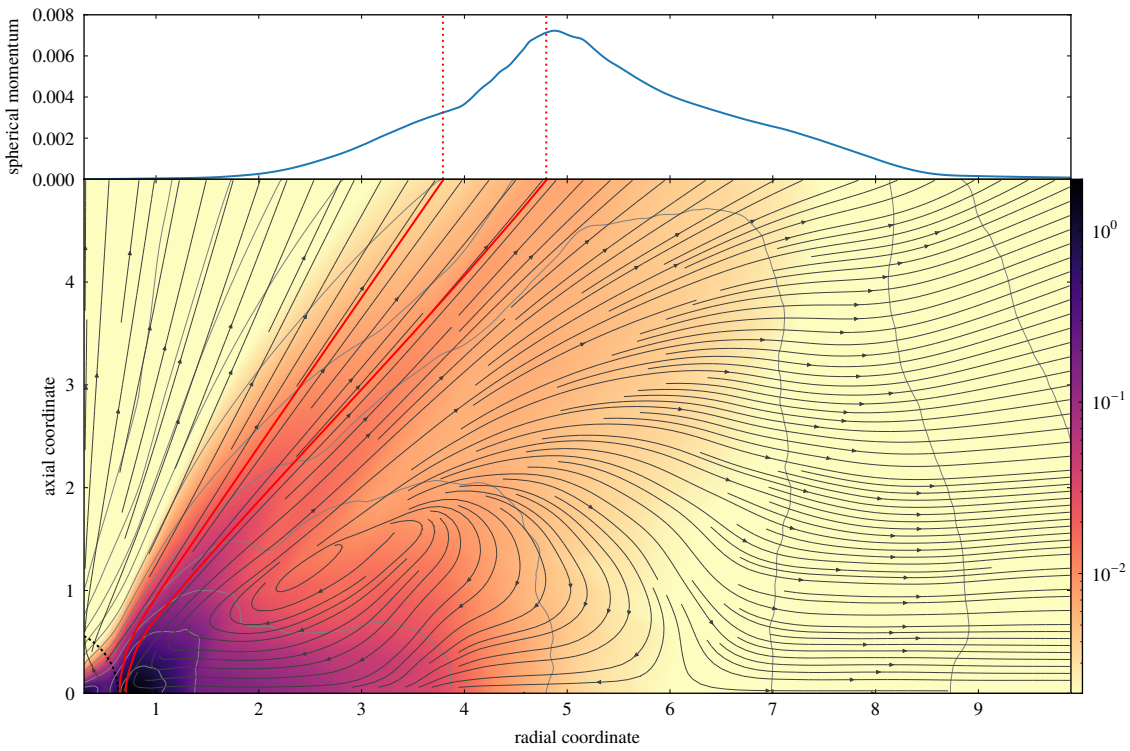

Figure 4.5. Gas flow in the time-averaged, azimuthally averaged, and vertically symmetrized poloidal plane in the "steady" state of the IR-RMHD stage. All quantities are normalized to fiducial units (§2.4.2). *Top panel:* Plot of $\hat{\mathbf{e}}_r \cdot (\rho \mathbf{v})$ along the upper-vertical boundary of the simulation domain. The left and right vertical dotted lines are drawn at $\tau_{\rm UV} = 1$ and $\tau_{\rm UV} = 4$. *Bottom panel:* Colors represent $\rho \|\mathbf{v}\|$, and dark gray streamlines follow gas velocity. The dust sublimation surface $r = r_{\rm ds}$ (§3.1.4) is the dotted black contour around the origin, red contours trace the surfaces on which $\tau_{\rm UV} = 1$ and $\tau_{\rm UV} = 4$, and light gray contours plot ρ / ρ_0 from 10^{-5} to 1 in logarithmic steps of $10^{0.5}$.

state as a result of mass resupply (§4.1.1.3), its inner edge may stay close to the dust sublimation surface and hence not have strong perturbations.

4.2.4 Support and gas dynamics in IR-RMHD stage

The advective, centrifugal, gravitational, gas, magnetic, IR, and UV forces are

$$\mathbf{f}_{\rm adv} \equiv -\rho\,(\mathbf{v}\cdot\nabla)\mathbf{v}, \tag{4.5a}$$

$$\mathbf{f}_{\rm cent} \equiv \frac{\rho v_\phi^2}{R}\,\hat{\mathbf{e}}_R, \tag{4.5b}$$

$$\mathbf{f}_{\rm grav} \equiv -\frac{GM\rho}{r^2}\,\hat{\mathbf{e}}_r, \tag{4.5c}$$

$$\mathbf{f}_{\rm gas} \equiv -\nabla p, \tag{4.5d}$$

$$\mathbf{f}_{\rm mag} \equiv -\mathbf{B}\times(\nabla\times\mathbf{B}), \tag{4.5e}$$

$$\mathbf{f}_{\rm IR} \equiv \frac{\rho\kappa_{\rm IR}}{c}\mathbf{F}_{\rm IR}, \tag{4.5f}$$

$$\mathbf{f}_{\rm UV} \equiv \frac{\rho\kappa_{\rm UV}}{c}\mathbf{F}_{\rm UV}. \tag{4.5g}$$

Note that the centrifugal force is part of the advective force. In the poloidal plane, $\mathbf{f}_{\rm adv}-\mathbf{f}_{\rm cent}$ can be understood in two equivalent ways: either as the rate of change of local momentum due to advection, or as the force $\mathbf{f}_{\rm ram}$ arising from ram pressure. The individual forces combine to form the Eulerian and "Lagrangian" non-gravitational forces:

$$\mathbf{f}_{\rm E} \equiv \mathbf{f}_{\rm adv}+\mathbf{f}_{\rm gas}+\mathbf{f}_{\rm mag}+\mathbf{f}_{\rm IR}+\mathbf{f}_{\rm UV}, \tag{4.5h}$$

$$\mathbf{f}_{\rm L} \equiv \mathbf{f}_{\rm cent}+\mathbf{f}_{\rm gas}+\mathbf{f}_{\rm mag}+\mathbf{f}_{\rm IR}+\mathbf{f}_{\rm UV}. \tag{4.5i}$$

The Eulerian non-gravitational force is easy to grasp: If $\mathbf{f}_{\rm E}+\mathbf{f}_{\rm grav}=\mathbf{0}$, then the flow is time-steady, but gas may still accelerate along streamlines. To interpret the "Lagrangian" non-gravitational force, we consider the force equation for a gas packet:

$$\rho\frac{d\mathbf{v}}{dt} = \mathbf{f}_{\rm grav}+\mathbf{f}_{\rm gas}+\mathbf{f}_{\rm mag}+\mathbf{f}_{\rm IR}+\mathbf{f}_{\rm UV}. \tag{4.6}$$

Since the R- and z-components of the left-hand side are $\rho[dv_R/dt - v_\phi(d\phi/dt)]$ and $\rho(dv_z/dt)$ respectively, the same components of $\mathbf{f}_{\rm L}+\mathbf{f}_{\rm grav}$ are $\rho(dv_R/dt)$ and $\rho(dv_z/dt)$. The "Lagrangian" non-gravitational force therefore tells us how the gas packet moves in the poloidal plane; the special case $\mathbf{f}_{\rm L}+\mathbf{f}_{\rm grav}=\mathbf{0}$ means that the gas packet does not move poloidally.

Figure 4.6 compares the radial and vertical components of non-gravitational forces in the IR-RMHD stage with those of the gravitational force. Gravity is closely matched both radially and vertically by $\mathbf{f}_{\rm E}$ in a sizable region that encompasses the body and the densest parts of the head. This implies the velocity field in the region changes little over time, so structures in the region have time-steady morphologies, which is what we claimed in §4.2.3. All forces contribute to create the approximate equality between $\mathbf{f}_{\rm E}$ and gravity, and the

relative significance of each force varies by position. The body is propped up in the vertical direction by both gas and IR radiation pressures; the same can be said of the lower parts of the wings directly above the body, in the triangular region bounded by $2\,r_0 \lesssim R \lesssim 3\,r_0$, $|z| \gtrsim 0.5\,r_0$, and $|z|/R \lesssim 0.7$. The head is vertically supported by gas pressure, and it appears taller than the body because IR and UV radiation are constantly pushing the inner edge up into a wind. IR radiation is also the primary driver of outflow in the wings at high latitudes. These are exactly the same conclusions drawn in the pure RHD case (§3.2.1).

It is instructive to trace the trajectory of gas originating from between the $\tau_{\rm UV} = 1$ surface and the transient as it goes through the structures; for this purpose, we pick $R = 4\,r_0$ and $z = 1.5\,r_0$ as our starting point. Gas motion at the starting point is determined by the balance of centrifugal, gas pressure, and IR radiative accelerations against gravity. Our scheme of converting gas pressure to IR radiation pressure before the IR-RMHD stage generates almost zero poloidal IR radiative flux at $t = 0$ (§4.1.1.4); this is soon corrected as IR radiation escapes. However, by the time IR radiative flux reaches steady state at $t \sim 5\,t_0$, its magnitude at $\tau_{\rm UV} \gtrsim 1$ is smaller than just after the beginning of the stage. Gas and IR radiation combined therefore furnish less radial and vertical support against gravity in the IR-RMHD stage than gas alone did in the UV-RMHD stage; indeed, $\mathbf{f}_{\rm L}$ at the starting point in Figure 4.6 is weaker than gravity both radially and vertically.

Gas was already radially infalling in the UV-RMHD stage due to reduced $j(R)$. Because support in the IR-RMHD stage is weaker than in the UV-RMHD stage, gas at the starting point collapses both radially and vertically, as demonstrated by the bottom row of Figure 4.2, and by Figure 4.5. This gas arrives at the upper surface of the body; Figure 4.2 shows a shock removing its vertical component of velocity, which is consistent with $\mathbf{f}_{\rm L}$ in Figure 4.6 pointing strongly upward throughout the body.

According to Figures 4.2 and 4.5, gas in the body moves radially inward with $-v_R \gg |v_z|$. The forces producing this flow can be found in Figure 4.6. In the radial direction, $\mathbf{f}_{\rm L}$ only partially supports the body against gravity, so gas accelerates radially as it falls inward through the body. In the vertical direction, gas piles onto the body in the manner described in the previous paragraph. The fact that $(\mathrm{sign}\,z)\,\hat{\mathbf{e}}_z \cdot (\mathbf{f}_{\rm E} - \mathbf{f}_{\rm L}) = (\mathrm{sign}\,z)\,\hat{\mathbf{e}}_z \cdot \mathbf{f}_{\rm ram} < 0$ means that advection brings gas with downward momentum to the body, or that vertically collapsing gas exerts downward ram pressure on the body. Ram pressure squeezes the body vertically, making the vertical extent of the body smaller than its sound speed would otherwise suggest.

Let us quantify the vertical forces in the body. If the total downward force on the body is unity, then the downward forces $\mathbf{f}_{\rm grav}$ and $\mathbf{f}_{\rm adv}$ have magnitudes ≈ 0.86 and ≈ 0.14, while the upward forces $\mathbf{f}_{\rm gas}$, $\mathbf{f}_{\rm mag}$, and $\mathbf{f}_{\rm IR}$ have magnitudes ≈ 0.58, ≈ 0.12, and ≈ 0.29 respectively. Clearly $\mathbf{f}_{\rm E} + \mathbf{f}_{\rm grav} \approx \mathbf{0}$, so gas motion over the entire body is time-steady and nearly horizontal. Moreover, gas pressure is chiefly responsible for counteracting downward forces in the body.

Gas ceases its horizontal drift through the body when it penetrates the irregular surface that separates the

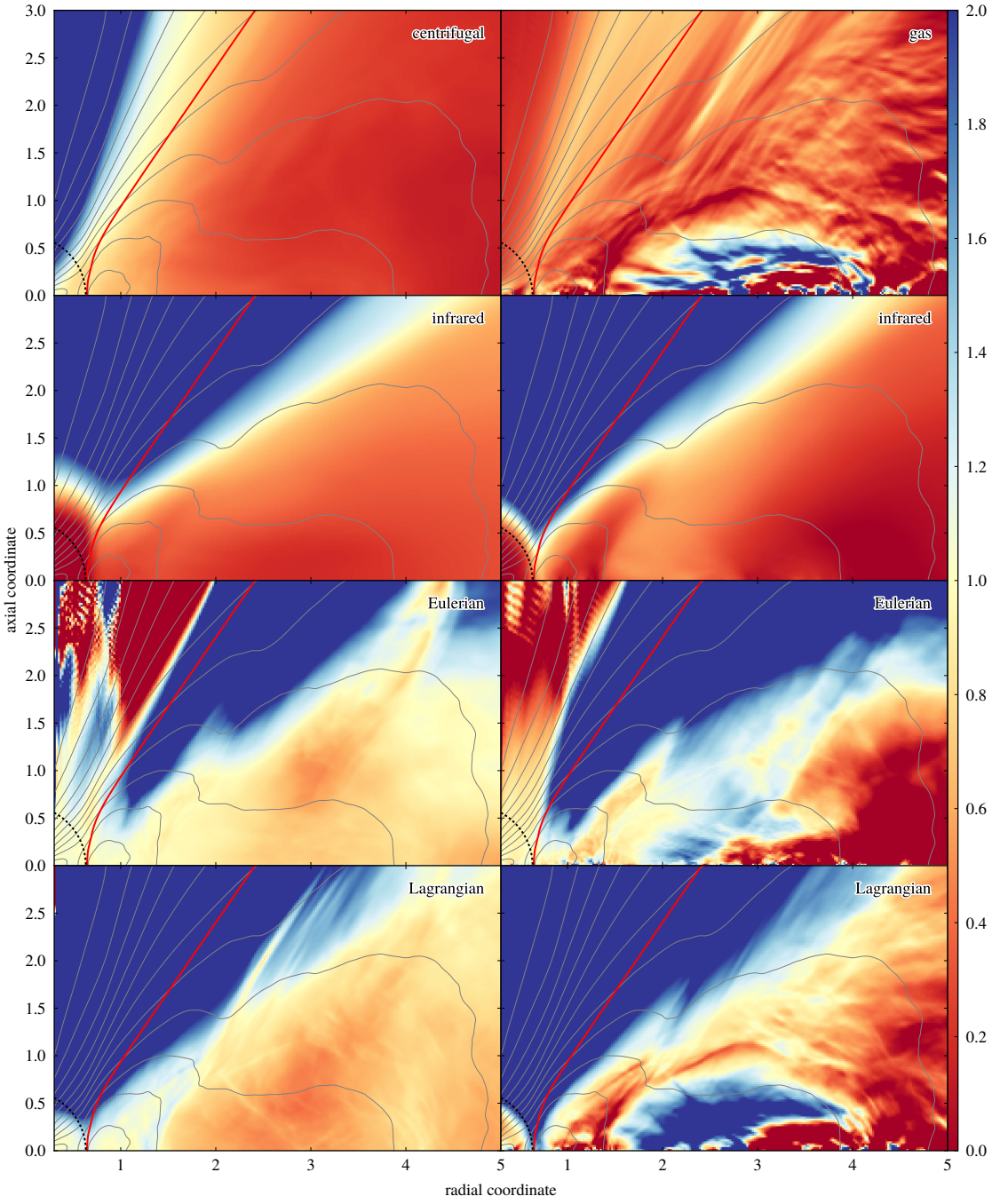

Figure 4.6. Ratios of force components to gravity in the zoom-in of the time-averaged, azimuthally averaged, and vertically symmetrized poloidal plane in the "steady" state of the IR-RMHD stage. Colors represent $\hat{\mathbf{n}} \cdot \mathbf{f} / (-\hat{\mathbf{n}} \cdot \mathbf{f}_{\rm grav})$, where $\hat{\mathbf{n}} \equiv \hat{\mathbf{e}}_R$ and $\hat{\mathbf{n}} \equiv \hat{\mathbf{e}}_z$ in the left and right columns; blue and red mean $\mathbf{f}$ provides support stronger and weaker than gravity respectively. The label in the top-right corner of each panel indicates the value of $\mathbf{f}$, as defined in Equation (4.5). The dust sublimation surface $r = r_{\rm ds}$ (§3.1.4) is the dotted black contour around the origin, the red contour traces the surface on which $\tau_{\rm UV} = 1$, and gray contours plot ρ / ρ_0 from 10^{-5} to 1 in logarithmic steps of $10^{0.5}$. All quantities are normalized to fiducial units (§2.4.2).

head from the body. We witness in Figure 4.2 that another shock strips the gas of its remaining horizontal component of velocity. Compared to the body, flow in the head has much smaller speeds. Figure 4.5 reveals that gas on the whole is still moving radially inward to the inner edge; as soon as it gets there, it is propelled outward by UV radiation.

By tracing the streamlines in Figure 4.5 from where they make a sharp turn near the inner edge, we learn that while part of the gas leaving the inner edge becomes the wind at $\tau_{\rm UV} \lesssim 1$, part of it recedes to $\tau_{\rm UV} \gtrsim 1$ and blends into the wings. Wings are the direct analogues of vertical structures in the UV-RMHD stage (§4.2.1). The two features are located in practically the same place, and everything that applies to vertical structures carries over to wings. In particular, wings host a sizable outflow: The "steady"-state mass, momentum, and kinetic energy loss rates at $\tau_{\rm UV} > 1$ are respectively ~ 6.1, ~ 1.8, and ~ 0.85 times those at $\tau_{\rm UV} < 1$.

Two distinctions must be made, however. First, while the UV-RMHD stage had $c_{\rm s}^2 \sim GM/r_{\rm ds}$, the IR-RMHD stage has $c_{\rm s}^2 \sim R_{\rm ideal} T_{\rm ds} \ll GM/r_{\rm ds}$, and it is obvious from Figure 4.3 that reducing $c_{\rm s}$ brings ψ closer to χ. In fact, if $c_{\rm s}/v_\infty \lesssim 0.1$, as in our simulation, then Equation (4.4) yields $\psi - \chi \approx (c_{\rm s}/v_\infty) \sin\chi$, hence wings are not vertical, but almost parallel to the inner surface. Second, IR radiative acceleration, which was entirely absent in the UV-RMHD stage, is critical for powering the outflow in the wings in the IR-RMHD stage. We can arrive at this conclusion in two ways. The upper parts of the wings at $\tau_{\rm UV} \gtrsim 1$ and $|z|/R \gtrsim 0.7$ experience substantial IR radiative acceleration, as seen in Figure 4.6, and they have v_r much higher than in vertical structures, as seen in the third and fourth columns of Figure 4.2. In addition, the top panel of Figure 4.5 plots the spherically radial component of gas momentum along the vertical boundaries. The curve peaks at $\tau_{\rm UV} \approx 4.87$, which is close to $\tau_{\rm UV} = \kappa_{\rm UV}/\kappa_{\rm IR} = 4$, the surface of unit IR optical depth from the origin; this suggests IR radiation from the central hole is heavily involved in driving the outflow.

Judging from the fifth column of Figure 4.2, vertical structures are gravitationally bound, whereas the upper parts of the wings appear to be unbound. Given our limited simulation domain, we cannot say definitively if the outflow in the wings would reach galactic scales; one possible scenario in which the outflow fails to leave the vicinity of the torus is as follows. If the infalling part of the torus has a flaring shape, as it ostensibly does in Figure 4.2, and if gas velocity in the wings does not make a large enough angle with the mid-plane, then the outflow may eventually run into the inflow. The outflow may lose energy in shocks, become bound, and merge with the inflow, thus creating a circulation of gas in the torus.

Lastly, the curve in the top panel of Figure 4.5 has no perceptible discontinuity at $\tau_{\rm UV} \sim 1$, which means IR and UV radiation cooperate to power a continuous outflow across a large solid angle, from the wind at $\tau_{\rm UV} \lesssim 1$ to the wings at $\tau_{\rm UV} \gtrsim 1$.

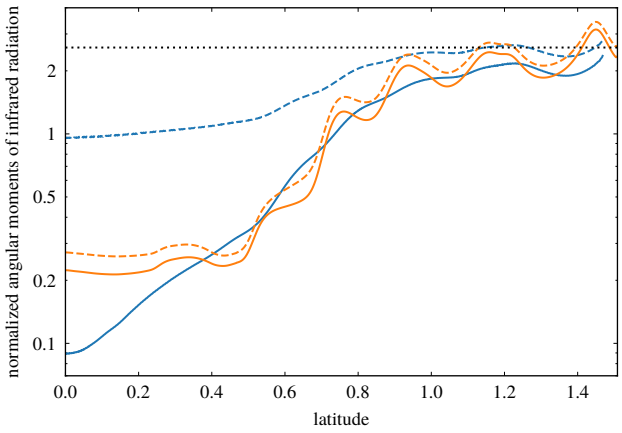

Figure 4.7. Plot of time-averaged, azimuthally averaged, and vertically symmetrized normalized angular moments of IR radiation against latitude in the "steady" state of the IR-RMHD stage. The solid and dashed curves of each color are for $[L_{\rm UV}/(4\pi r^2)]^{-1}\,\hat{\mathbf{e}}_r \cdot \mathbf{F}_{\rm IR}$ and $[L_{\rm UV}/(4\pi r^2)]^{-1}\,(cE_{\rm IR})$ respectively. Blue curves are at $r = 3\,r_0$; orange curves are at the outer-radial and vertical boundaries of the simulation domain. The horizontal dotted line is drawn at $C_{\rm IR}/(1 - C_{\rm IR})$.

4.2.5 IR radiation and temperature in IR-RMHD stage

We define the normalized IR radiative flux and radiation energy density as $[L_{\rm UV}/(4\pi r^2)]^{-1}\,\hat{\mathbf{e}}_r \cdot \mathbf{F}_{\rm IR}$ and $[L_{\rm UV}/(4\pi r^2)]^{-1}\,(cE_{\rm IR})$ respectively; the former quantity is unity if all UV radiation were converted to the IR, and if IR radiative flux were spherically symmetric. Figure 4.7 displays the quantities in the IR-RMHD stage on two surfaces. The blue curves are for a sphere of radius $r = 3\,r_0$, which cuts through the body; the orange curves are for the boundaries of the simulation domain. The wiggles are the consequence of the IR RT module directing radiation into preferred directions in optically thin regions (§2.1), hence they are not physical.

Let us consider the normalized IR radiative flux along sightlines emanating from the origin. On the one hand, sightlines close to the mid-plane penetrate the dense head and body closer in, and tenuous gas further out; as a result, the normalized IR radiative flux varies by a factor of ~ 2 along a sightline, which is reflected by the spread between the solid curves in Figure 4.7 at low latitudes. At large distances, far away from the head and the body, the normalized IR radiative flux on each sightline stabilizes to a constant value as indicated by the solid orange curve. On the other hand, sightlines close to the axis pass through tenuous gas in the wings or the central hole. Fluctuations in the normalized IR radiative flux arise from the aforementioned numerical artifacts and do not die out with distance; they explain the wiggles of the solid orange curve about its mean, which we can tell is merely $\lesssim 20\,\%$ at high latitudes. The normalized IR radiative flux along the boundaries is therefore a good approximation of its value at infinity in the "steady" state. The normalized IR radiative flux rises with latitude on both surfaces considered, approaching $\sim C_{\rm IR}/(1 - C_{\rm IR})$ near the axis; this is exactly the same effect of the torus concentrating IR radiation into the central hole as in pure RHD (§3.2.3).

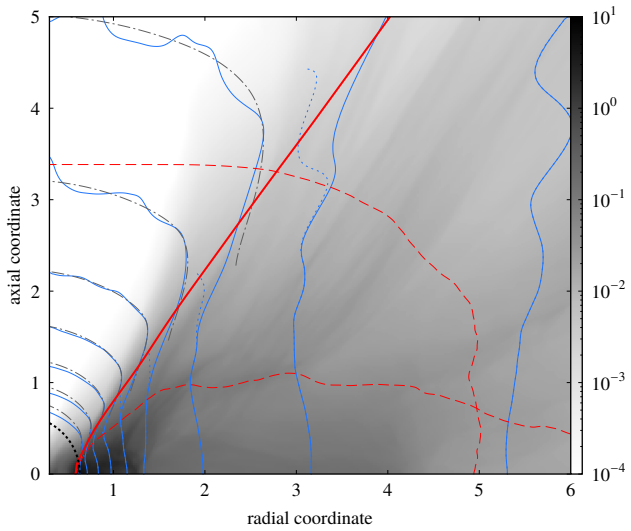

Figure 4.8. Zoom-in of the azimuthally averaged and vertically symmetrized poloidal plane in the IR-RMHD stage at time $t = 14\,t_0$. Solid and dotted blue contours show gas and IR temperatures; dash-dotted gray contours show the modeled temperature given by Equation (4.8). Temperatures on these contours go down from $T_{\rm ds}$ in steps of $0.1\,T_{\rm ds}$ as one moves away from the origin. Only parts of the IR and modeled temperature contours are drawn to reduce clutter. The top and bottom dashed red contours are the edge-on and face-on IR photospheres (§4.3.1). Gas density is presented on a logarithmic scale as gray intensities (see color bar along the right edge), the dust sublimation surface $r = r_{\rm ds}$ (§3.1.4) is the dotted black contour around the origin, and the solid red contour traces the surface on which $\tau_{\rm UV} = 1$. All quantities are normalized to fiducial units (§2.4.2).

The ratio of IR radiative flux to IR radiation energy density, $0 \leq \hat{\mathbf{e}}_r \cdot \mathbf{F}_{\rm IR} / (cE_{\rm IR}) \leq 1$, or the ratio of solid to dashed curve in Figure 4.7, measures how anisotropic IR radiation is locally. At small distances, an increase in latitude means a transition from the dense head and body into the tenuous wings and central hole; this drop in density and optical thickness is accompanied by a rise in IR radiation anisotropy. IR radiation energy density therefore increases with latitude as IR radiative flux does, but less steeply. In a genuine steady state, the dense body should extend all the way to the outer-radial boundary of the simulation domain, so anisotropy should be observed at the boundaries too; the fact it is not has to do with the torus being only in an approximate "steady" state, and the body being limited in radial extent.

Understanding the angular distribution of IR radiation energy density is crucial because, as Figure 4.8 demonstrates, gas and IR temperatures are mostly equal at $\tau_{\rm UV} \gtrsim 1$. Since IR radiation energy density rises with latitude, temperature contours are not spherical, but flare radially outward at high latitudes. The dashed orange curve in Figure 4.7 has greater variation over latitude than the dashed blue curve; accordingly, temperature contours in Figure 4.8 flare more strongly at greater distances. In our simulation, temperature contours are remarkably vertical from the mid-plane almost up to the $\tau_{\rm UV} = 1$ surface.

Temperature in the central hole has a spherically symmetric distribution, with deviations only at the angles into which the IR RT module tends to concentrate IR radiation (§2.1). The temperature T can be modeled by

considering the balance of energy emitted and absorbed by a dust grain of radius a:

$$4\pi a^2 \kappa_{\rm IR} \frac{c a_{\rm SB}}{4} T^4 = \pi a^2 \kappa_{\rm UV} \frac{L_{\rm UV}}{4\pi r^2} e^{-\tau_{\rm UV}} + \pi a^2 \kappa_{\rm IR} F_{\rm IR}. \tag{4.7}$$

Following §3.3.1, the IR radiative flux is $F_{\rm IR} \approx C_{\rm UV}/(1 - C_{\rm IR}) \times L_{\rm UV}/(4\pi r^2)$. The UV absorption term contains the UV radiative flux corrected for extinction; such correction is unnecessary for the IR because $\tau_{\rm UV} \lesssim 1$ automatically implies $\tau_{\rm IR} \ll 1$, where $\tau_{\rm IR}$ is the optical depth from the central source. Rearranging, we get

$$a_{\rm SB} T^4 \approx \frac{L_{\rm UV}}{4\pi r^2 c} \left(\frac{\kappa_{\rm UV}}{\kappa_{\rm IR}} e^{-\tau_{\rm UV}} + \frac{C_{\rm UV}}{1 - C_{\rm IR}} \right). \tag{4.8}$$

Using the operational definition of $C_{\rm IR}$ and the simplification $C_{\rm UV} \approx C_{\rm IR}$ from §3.3.1, we plot the modeled temperature in Figure 4.8; the model is excellent at $\tau_{\rm UV} \lesssim 1$. Equations (4.3) and (4.8) agree if $\tau_{\rm UV} \ll 1$ and $F_{\rm IR} = 0$, hence the opacity temperature in the UV-RMHD stage is consistent with the actual temperature in the IR-RMHD stage.

4.2.6 Magnetic field in IR-RMHD stage

Figure 4.9 graphs gas-only plasma beta $\beta_{\rm g} \equiv p/(\frac{1}{2}B^2)$ and total plasma beta $\beta_{\rm t} \equiv (p + \frac{1}{3}E_{\rm IR})/(\frac{1}{2}B^2)$ at $t = 0$ and $t = 14\,t_0$ in the IR-RMHD stage. The range of $\beta_{\rm g}$ varies little across space and time. The same can be said of $\beta_{\rm t}$, except that its value at $t = 14\,t_0$ is much higher in the central hole and the upper parts of the wings than the rest of the simulation domain. This is because $E_{\rm IR}$ is a few times higher in the central hole than other parts of the torus, while p is several orders of magnitudes lower; it then follows from the definitions of the plasma betas that $\beta_{\rm t} \gg \beta_{\rm g}$. The constancy of $\beta_{\rm g}$ and $\beta_{\rm t}$ over time means that the complex gas motion in the IR-RMHD stage does not perceptibly modify the MHD saturation state, at least not within our finite simulation time. The distributions of $\beta_{\rm g}$ and $\beta_{\rm t}$ are also virtually identical apart from the overall normalization, and apart from the central hole. Moreover, Figure 4.9 suggests that only the wings, where outflow drags out field lines, have large-scale order in the magnetic field, but even there the field does not point uniformly inward or outward, and neighboring regions can have fields in opposite directions.

We define the density-weighted plasma betas and alpha parameter as

$$\langle \beta_{\rm g} \rangle \equiv \frac{\int dV\, \rho p}{\int dV\, \rho\, (\frac{1}{2}B^2)}, \tag{4.9a}$$

$$\langle \beta_{\rm t} \rangle \equiv \frac{\int dV\, \rho\, (p + \frac{1}{3}E_{\rm IR})}{\int dV\, \rho\, (\frac{1}{2}B^2)}, \tag{4.9b}$$

$$\langle \alpha \rangle \equiv \frac{\int dV\, \rho\, (\rho v_R \Delta v_\phi - B_R B_\phi)}{\int dV\, \rho\, (p + \frac{1}{3}E_{\rm IR})}, \tag{4.9c}$$

where Δv_ϕ is the perturbation of v_ϕ about its azimuthal average. We see $\langle \beta_{\rm g} \rangle$ rise steadily from $\langle \beta_{\rm g} \rangle \sim 4.2$ to $\langle \beta_{\rm g} \rangle \sim 4.6$ over $0 \lesssim t \lesssim 10\,t_0$ and more rapidly to $\langle \beta_{\rm g} \rangle \sim 7.5$ at $t = 14\,t_0$, while $\langle \beta_{\rm t} \rangle$ drops suddenly from

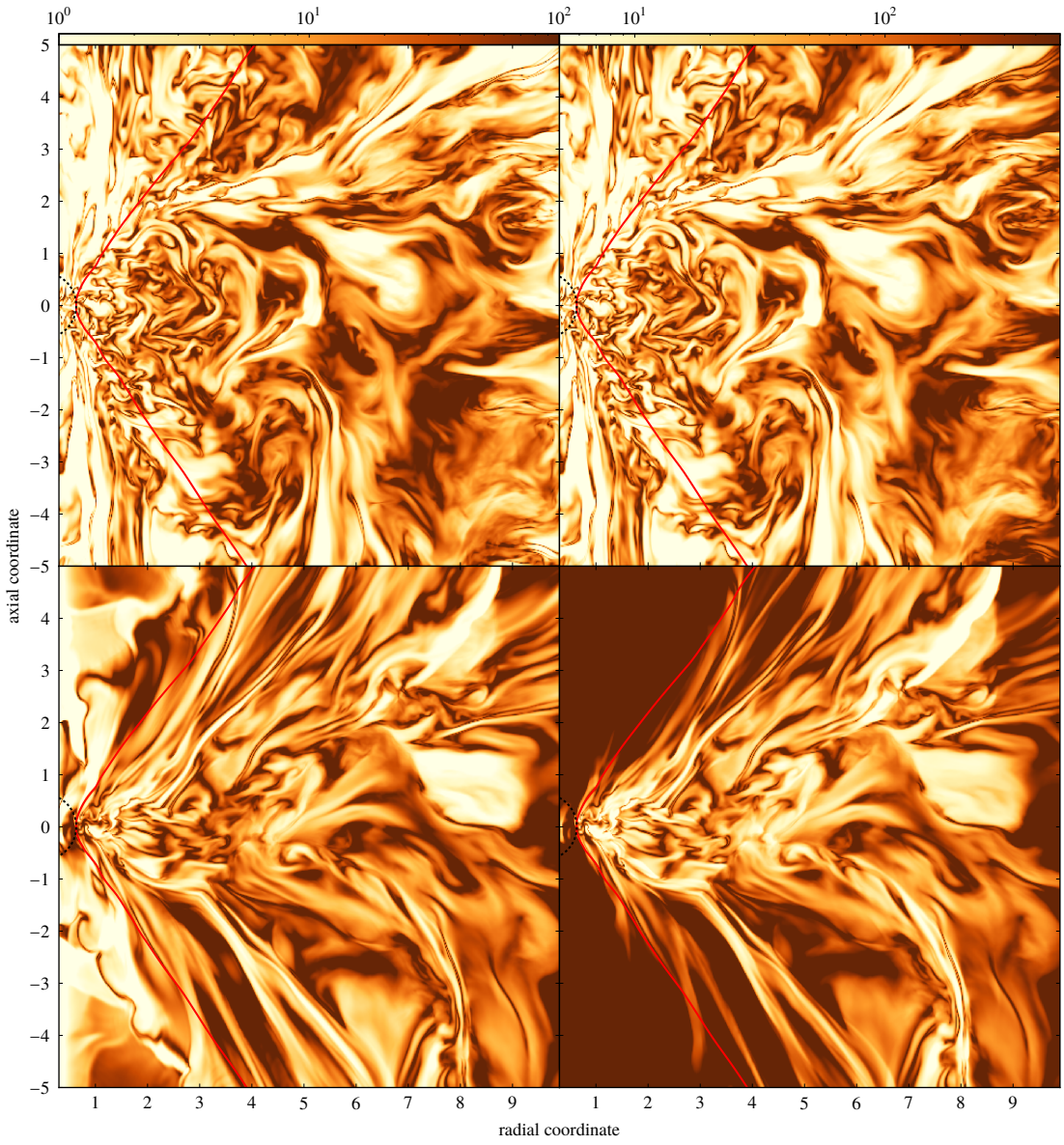

Figure 4.9. Plasma betas in the poloidal plane along $\phi = 0$ in the IR-RMHD stage. Colors in the left and right columns represent gas-only and total plasma beta respectively (§4.2.6; see color bars along the top edge). The top and bottom rows are at $t = 0$ and $t = 14\,t_0$. The dust sublimation surface $r = r_{\rm ds}$ (§3.1.4) is the dotted black contour around the origin, and the red contour traces the surface on which $\tau_{\rm UV} = 1$. All quantities are normalized to fiducial units (§2.4.2).

$\langle \beta_t \rangle \sim 27$ to $\langle \beta_t \rangle \sim 19$ over $0 \lesssim t \lesssim 2\,t_0$ and holds still at $\langle \beta_t \rangle \sim 16$ thereafter. In addition, $\langle \alpha \rangle$ climbs from $\langle \alpha \rangle \sim 0.019$ to $\langle \alpha \rangle \sim 0.044$ over $0 \leq t \leq 14\,t_0$. MHD turbulence is likely at saturation in the IR-RMHD stage since all three parameters lie within their expected ranges.

4.3 Discussion

We derive several important observational predictions for our torus, and we consider how our simulation results would extrapolate to realistic values of simulation parameters.

4.3.1 Observed temperature profiles in IR-RMHD stage

Interferometric observations of AGN tori are analyzed by fitting ellipsoidal blackbodies of various sizes and temperatures to the visibilities; the result can be interpreted as a crude temperature profile (e.g., Tristram et al. 2007). To facilitate comparison of our torus in the IR-RMHD stage with observations, it would be useful to locate its IR photospheres as seen by observers both face-on and edge-on, and to determine the observed temperature profiles.

The IR photosphere is determined using the same opacity prescription as used in the simulation (§2.3.6), that is to say, a single opacity $\kappa_{\rm IR}$ applies to the entire IR, and $\kappa_{\rm IR}/\kappa_{\rm T} = 20$ wherever $T \lesssim T_{\rm ds}$ (§2.3.6). This is of course overly simplistic: While $\kappa_{\rm IR}/\kappa_{\rm T} = 20$ is roughly true for NIR, opacity is lower at longer wavelengths. The following remarks should therefore be taken as a zeroth-order prediction of the observed temperature profile.

The bottom dashed red contour in Figure 4.8 shows the face-on IR photosphere of our torus, that is, where the IR optical depth as measured vertically from the upper-vertical boundary equals unity. The face-on IR photosphere is roughly the surface that separates the head and the body below from the wings above, hence it is essentially horizontal; in contrast, temperature contours at $\tau_{\rm UV} \gtrsim 1$ are close to vertical in our simulation (§4.2.5). Consequently, a face-on observer sees a radial temperature gradient $T \propto R^{-0.73}$, with $T \approx T_{\rm ds}$ at the dust sublimation radius. Note that our definition of the face-on IR photosphere depends on our choice of simulation domain. Figure 4.8 encompasses the full vertical extent of our simulation domain; judging from the figure, if we were to enlarge the simulation domain vertically, parts of the face-on IR photosphere at $R \lesssim 4\,r_0$ would barely change because sightlines from the upper-vertical boundary would simply encounter additional amounts of tenuous gas at $\tau_{\rm UV} \lesssim 1$, but parts at $R \gtrsim 4\,r_0$ would shift upward noticeably because sightlines would cut through more of the dense gas at $\tau_{\rm UV} \gtrsim 1$. This vertical displacement of the edge-on IR photosphere should not qualitatively change the observed temperature gradient since temperature contours are vertical (§4.2.5).

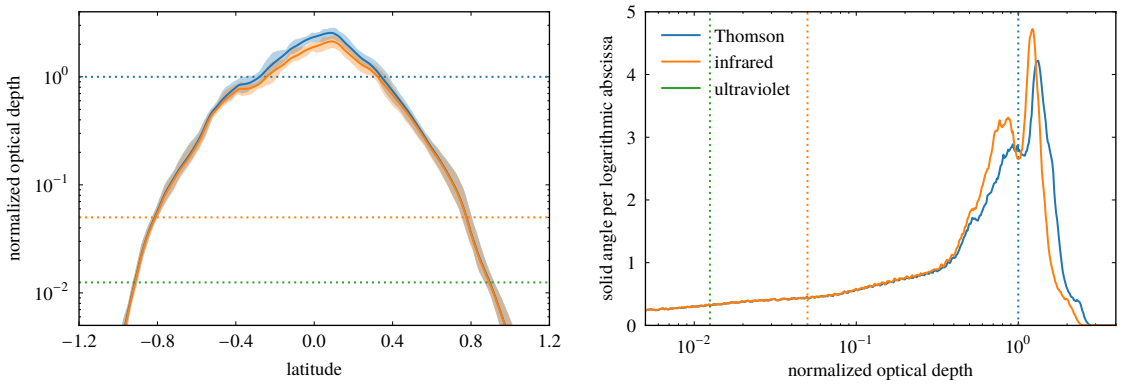

Figure 4.10. *Left panel:* Plot of normalized optical depths (§4.3.2) along sightlines of varying latitudes in the IR-RMHD stage at $t = 14\,t_0$. The thick curve is the azimuthal average, and the shaded area is the range covered by all azimuthal angles. *Right panel:* Histogram of the solid angle around the origin occupied by gas columns with normalized optical depths in each logarithmic bin in the "steady" state of the IR-RMHD stage. *Both panels:* Curves for IR and UV are identical. Dotted lines indicate optical depth of unity at each frequency.

The top dashed red contour shows the edge-on IR photosphere, that is, where the IR optical depth as measured horizontally from the outer-radial boundary equals unity. The edge-on IR photosphere is quite cylindrical, rising vertically from $R \sim 5\,r_0$ and then making a turn to horizontal at $2\,r_0 \lesssim |z| \lesssim 3.5\,r_0$; this means that, above a certain altitude, the observer can suddenly peer much deeper into the torus and see the hotter gas in the central hole. If we were to expand the simulation domain radially, the edge-on IR photosphere would move radially outward for reasons similar to the above, but the exact displacement depends sensitively on the unknown gas distribution outside the simulation domain. Nevertheless, since $\kappa_{\rm IR}$ is constant at $r \gtrsim r_{\rm ds}$ and density generally falls off with height, the tangent $|dz/dR|$ to the edge-on IR photosphere can only decrease as a result of an increase in the radial extent of the simulation domain, so our comment about the abrupt rise in temperature is robust.

4.3.2 X-ray, IR, and UV obscuration in IR-RMHD stage

The left panel of Figure 4.10 plots Thomson, IR, and UV optical depths as a function of inclination for one snapshot in the IR-RMHD stage; to fit the curves into the same scale, each optical depth is normalized by unity, $\bar{\kappa}_{\rm IR}/\kappa_{\rm T} = 20$, and $\bar{\kappa}_{\rm UV}/\kappa_{\rm T} = 80$ respectively (§2.3.6). In addition, because $\kappa_{\rm IR}/\kappa_{\rm UV} = \bar{\kappa}_{\rm IR}/\bar{\kappa}_{\rm UV} =$ constant (§2.3.6), UV curves are indistinguishable from IR curves and hence suppressed. Curves at all three frequencies almost coincide, with small discrepancies only at low latitudes. This is because $\kappa_{\rm IR,UV}$ are constant practically everywhere except for trace amounts of gas at $r \lesssim r_{\rm ds}$; this gas is geometrically thin, so it merely affects sightlines close to the mid-plane. The graph also makes it clear that optical depth in our torus is largely independent of azimuth.

The right panel plots $d\Omega/d\log_{10}\tau$, the solid-angle coverage around the origin as a function of logarithmic

normalized optical depths, during the "steady" state of the IR-RMHD stage. The coarse shape of the histogram, particularly the presence of two peaks, can be recovered simply by treating the shaded region in the left panel as a two-dimensional distribution and marginalizing the distribution over latitude. A more physical interpretation of the origin of the peaks is that sightlines through both head and body contribute to the right peak, while those through the head alone contribute to the left peak.

X-ray observations of obscured AGNs indicate gas columns of $N_{\rm H} \gtrsim 10^{22}\,{\rm cm}^{-2}$ or $\tau_{\rm T} \geq 0.01$, whereas obscuration in the IR and UV requires $\tau_{\rm IR} \gtrsim 1$ and $\tau_{\rm UV} \gtrsim 1$ respectively. The histogram informs us that the X-ray, IR, and UV covering fractions are ≈ 0.80, ≈ 0.72 and ≈ 0.79. These numbers are close to one another, and also to the observed fraction of type-2 AGNs (e.g., Lawrence & Elvis 2010). Such broad coverage of the central source is achieved by combining the head, the body, the wings, and the wind. In contrast, X-rays at $\sim 7\,{\rm keV}$ to $\sim 100\,{\rm keV}$ are blocked along Compton-thick sightlines with $N_{\rm H} \gtrsim 10^{24}\,{\rm cm}^{-2}$ or $\tau_{\rm T} \geq 1$. Only sightlines traversing both head and body have such high optical depths; they are concentrated near the mid-plane and take up ≈ 0.27 of the solid angle. Note that these covering fractions are strictly valid just for our torus, which has a radial Thomson optical depth of ~ 2 along the mid-plane (§4.1.1.4).

Lastly, we look at the density profiles that give rise to obscuration. Figure 4.11 graphs density in a snapshot along sightlines to the central source. On the one hand, sightlines at latitudes $\lesssim 0.4\,{\rm rad}$ pass through the dense head and body. These sightlines also intersect the transient; because gas radially outward of the transient is not part of the "steady" state, we truncate their corresponding curves at the transient. Density decreases outward on a sightline, but not smoothly; the fluctuation about the local mean is $\lesssim 50\,\%$. Density is also remarkably similar from one sightline to another in the region between $\tau_{\rm UV} \gtrsim 1$ and $r \lesssim 1.5\,r_0$, which corresponds to the head. On the other hand, sightlines at latitudes between $\sim 0.4\,{\rm rad}$ and $\sim 0.9\,{\rm rad}$ lie in the region between the inner surface and the transient, and they encounter the dense head and the tenuous wings. Density fluctuations are greater along sightlines at higher latitudes, up to a factor of a few. Local maxima in density are not due to cubic (Stalevski et al. 2012) or spherical (Hönig et al. 2006; Schartmann et al. 2008; Heymann & Siebenmorgen 2012; Roth et al. 2012) clumps, or to isolated clumps (Nenkova et al. 2002, 2008a) at all, as is typically assumed in phenomenological torus RT models, but to density ridges in the wings; since the wings are parallel to the inner surface (§4.2.4), the spacing between the maxima rises with sightline latitude.

4.3.3 Extrapolating to realistic AGN tori

Our simulation cannot use parameters that apply directly to realistic AGNs due to numerical reasons; instead, we must adopt a smaller central mass M (§2.4.1), or equivalently, a higher $c_{\rm s}/v_\phi$, as well as a lower UV opacity

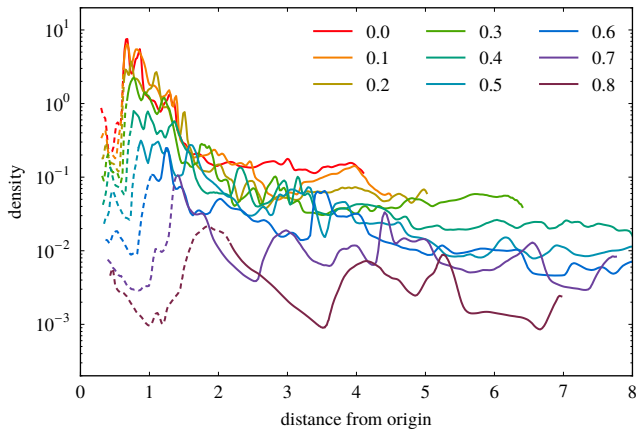

Figure 4.11. Plot of gas density in the IR-RMHD stage at $t = 14\,t_0$ along sightlines to the central source at fixed azimuth $\phi = 0$ and varying latitudes as indicated in the legend. The dashed and solid portions of each curve are at $\tau_{\rm UV} < 1$ and $\tau_{\rm UV} > 1$ respectively. All quantities are normalized to fiducial units (§2.4.2).

$\kappa_{\rm UV}$ (§2.3.6). It is imperative that we understand how our results may change when these two parameters are set to their realistic values.

Moreover, our simulations consider just a few values for the Thomson optical depth $\tau_{\rm T}$, and completely ignore photoionization and volumetric Compton heating. In view of the scarcity of data points furnished by our simulations, we can only hypothesize about the effects of varying $\tau_{\rm T}$ and including additional physics.

4.3.3.1 Mass loss rate and wind terminal speed

Mass, momentum, and kinetic energy loss rates are important observables of our simulation. We devised scaling relations that allowed us to extrapolate loss rate measurements to realistic AGNs in §§3.2.4 and 3.3.3; in this language, the average "steady"-state mass loss rate in the IR-RMHD stage through the vertical boundaries in the wind and the wings, when scaled to realistic values of M and $\kappa_{\rm UV}$, is

$$\sim 0.3 \left(\frac{M}{10^7\,M_\odot}\right)^{3/4} \left(\frac{L_{\rm UV}/L_{\rm E}}{0.1}\right)^{3/4} \left(\frac{\kappa_{\rm IR}/\kappa_{\rm T}}{20}\right)^{-1/4} \left(\frac{\kappa_{\rm UV}/\kappa_{\rm T}}{2000}\right)^{-1/4} M_\odot\,{\rm yr}^{-1}; \tag{4.10}$$

here $R_{\rm in} = r_{\rm ds}$ is assumed. Comparing mass to momentum and kinetic energy loss rates yields a typical wind terminal speed of

$$\sim 3000 \left(\frac{M}{10^7\,M_\odot}\right)^{1/4} \left(\frac{L_{\rm UV}/L_{\rm E}}{0.1}\right)^{1/4} \left(\frac{\kappa_{\rm IR}/\kappa_{\rm T}}{20}\right)^{1/4} \left(\frac{\kappa_{\rm UV}/\kappa_{\rm T}}{2000}\right)^{1/4} {\rm km\,s}^{-1}. \tag{4.11}$$

Both values are similar to previous results (§3.3.3), and their variation over time is merely $\sim 10\,\%$. Considering that only part of the outflow is gravitationally unbound, and part of it may collide with a geometrically thick inflow (§4.2.4), the mass loss rate and wind terminal speed at infinity could be smaller than indicated.

4.3.3.2 Morphology

The "steady"-state morphology of the torus at $\tau_{\rm UV} \gtrsim 1$ does not depend strongly on $\kappa_{\rm UV}$, but it does depend on $c_{\rm s}/v_\phi$. It is conceivable that the structures identified in §4.2.3 would remain when $c_{\rm s}/v_\phi$ falls, but their dimensions would not be the same. The body relies heavily on gas pressure for vertical support (§4.2.4), so its vertical extent would likely decrease with $c_{\rm s}/v_\phi$. The head is supported by a combination of forces, including IR and UV radiation pressure (§4.2.4), so its height should scale more slowly with $c_{\rm s}/v_\phi$. Because distributions of gas and IR radiation influence each other, there may not be a strict proportionality between $c_{\rm s}/v_\phi$ and the aspect ratio of either head or body. In contrast, wings are excited by gas launched along the inner surface by UV radiation and receive much support from IR radiation (§4.2.4); therefore, we believe their geometry is not sensitive to $c_{\rm s}/v_\phi$.

We can only conjecture on how the torus may respond if we modify the density and $\tau_{\rm T}$ of the initial condition. Both the rate of momentum delivery to the torus by UV radiation, and v_∞ of the outflow as given by Equation (4.10), depend solely on $L_{\rm UV}$; this means the characteristic density of the outflow, and hence its obscuration properties, should be the same regardless of $\tau_{\rm T}$. It is difficult to establish with certainty the effect of $\tau_{\rm T}$ on the body, but a self-consistent and plausible scenario is as follows: Upon an increase in $\tau_{\rm T}$, the body becomes denser, geometrically thinner, and less permeable to the IR radiation that ultimately determines the amount of gas and IR radiative support it receives; upon a decrease in $\tau_{\rm T}$, the opposite happens.

4.3.3.3 Temperature

Temperature contours in our simulation (§4.2.5) are quite vertical far above head and body, suggesting that temperature distribution in our simulation is not completely dictated by the two structures. If torus temperature balance is controlled not by internal dissipation at the mid-plane, but by external illumination, then it stands to reason that time-averaged temperature contours near the mid-plane should not be far from vertical, no matter what $c_{\rm s}/v_\phi$ is. The fact that verticality extends far beyond the mid-plane in our simulation should not be interpreted as a general feature at any $c_{\rm s}/v_\phi$, but as a suggestion that the shape of temperature contours enjoys relative independence from that of the head and the body.

We could ask how the observed face-on and edge-on temperature profiles (§4.3.1) change as a function of $c_{\rm s}/v_\phi$. The face-on IR photosphere follows the outline of the head and the body. With smaller $c_{\rm s}/v_\phi$, both structures would be flatter; by virtue of the verticality of temperature contours near the mid-plane, a radially outward temperature gradient should always be observed, although the magnitude of the gradient could be different. As for the temperature profile of the edge-on IR photosphere, the jump at large altitudes is a consequence of density in the wings diminishing with height; as long as wings remain geometrically thick,

the jump should remain.

4.3.3.4 Obscuration

The obscuration properties of the torus are a direct consequence of its density distribution. The X-ray, IR, and UV covering fractions should not vary strongly with c_s/v_ϕ or τ_T; this is because the primary obscurers are the wings and the wind (§4.3.2), which should remain geometrically thick at lower c_s/v_ϕ and equally dense at any τ_T (§4.3.3.2). However, the Compton-thick fraction would decline with smaller c_s/v_ϕ because the obscurers here are the head and the body, both of which would be thinner at reduced c_s/v_ϕ.

Another important aspect of AGN obscuration is the distribution of observed column densities. Stated in terms of simulation variables, the observed $d\Omega/d\log_{10}\tau$ is generally flat for $\tau_T \gtrsim 0.01$, with a slight rise toward higher τ_T (e.g., Gilli et al. 2007, and references therein). Our torus already has flat $d\Omega/d\log_{10}\tau$ for $\tau \lesssim 0.4$ (§4.3.2), and we get an even better agreement with observations if we consider how $d\Omega/d\log_{10}\tau$ would change under smaller c_s/v_ϕ or different τ_T.

With lower c_s/v_ϕ, gas would concentrate toward the mid-plane, and both head and body would take up a smaller solid angle; as a consequence, the slender peaks in the right panel of Figure 4.10, which reflect the densest parts of the torus, would move to the right, and the area under them would diminish. Presumably there would still be the same gentle roll-off to a plateau on the left side, but the plateau would be higher because the total area under the histogram is conserved. The histogram would therefore become flatter, which means $d\Omega/d\log_{10}\tau$ would be practically constant over a large range of $\log_{10}\tau$.

Alternatively, realistic tori might have a wide range of τ_T extending up to a few. Since our torus has $\tau_T \sim 2$ (§4.1.1.4), we are mostly interested in reducing τ_T, which, for exactly the opposite reason as in the preceding paragraph, would shift the peaks to the left. When $d\Omega/d\log_{10}\tau$ histograms for different AGNs are stacked, offset peaks would add up to form a flatter distribution; in other words, the near constancy of $d\Omega/d\log_{10}\tau$ over $\log_{10}\tau$ is a natural consequence of realistic AGNs having a broad distribution of τ_T.

4.3.3.5 Additional physics

Reinstituting physical effects left out of the simulation could induce further changes. Our simulation is best at treating IR RT at $\tau_{IR} \gtrsim 1$, or where the column density from the central source is $\gtrsim 8 \times 10^{22}\,\mathrm{cm}^{-2}$; it is not as reliable inside the central hole since we omit UV and X-ray photoionization. The primary effect of photoionization is to raise the temperature of the central hole (Krolik & Begelman 1986; Krolik & Kriss 2001). The increased gas pressure inside the central hole can compress the torus; hotter gas can also destroy dust grains through sputtering (Draine & Salpeter 1979; Tielens et al. 1994), thus reducing the effectiveness of wind driving through radiation pressure on dust. Meanwhile, photoionization can impart momentum to the

wind through lines. Gas redistribution inside the central hole due to these effects alters the soft X-ray, IR, and UV covering fractions, as well as $d\Omega/d\log_{10}\tau$. In particular, warm absorbers are observed to have column densities within the narrow range of $\sim 10^{21}$ cm^{-2} to $\sim 10^{22}$ cm^{-2} (e.g., Blustin et al. 2005), which is equivalent to $7\times10^{-4} \lesssim \tau_{\rm T} \lesssim 7\times10^{-3}$, but $d\Omega/d\log_{10}\tau$ in our simulation shows no enhancement within that range (§4.3.2).

We ignore volumetric Compton heating in our simulations, but X-rays at luminosities a few times weaker than the UV can produce sufficient IR radiation deep inside the torus to induce important changes to the distributions of density and specific angular momentum, particularly near the mid-plane (Shi & Krolik 2008). As a matter of fact, since the mid-plane is optically thick in the IR but only marginally so to X-rays, X-rays could be the deciding factor in how concentrated the torus is around the mid-plane. A positive feedback loop could exist, wherein Compton heating deposits the energy requisite to seed a vertical IR radiative flux, which then lowers the density near the mid-plane and allows IR radiation from the inner edge to enter the torus and support it (see also Roth et al. 2012). Compton heating most certainly will change gas and IR temperatures at $\tau_{\rm UV} \gtrsim 1$, but the arguments regarding the observed temperature gradients presented above should still hold qualitatively.

4.3.4 Comparison with other torus models

This is not the first attempt at understanding torus dynamics; in fact, several previous efforts have been made to see whether outflows could account for torus phenomenology. We situate our work relative to theirs by summarizing the contrasts.

Königl & Kartje (1994) proposed that obscuration in AGNs could be provided by a magnetocentrifugal wind, which, intuitively speaking, is a centrifugally driven outflow guided by open magnetic field lines. Their model presupposes a razor-thin accretion disk as the mass source for the wind; our simulation simply allows a given amount of gas to evolve without prescribing how mass resupply occurs. Their model also requires the specification of several parameters for the wind, among which are the launch radius from the accretion disk, the spherically radial density profile, and the conserved mass flux and angular momentum along the streamline, whereas our simulation only fixes the initial angular momentum profile (§4.1.1.3). Most importantly, their model posits the existence of a large-scale, dynamically dominant magnetic field; in contrast, our simulation reveals that radiation alone can lift gas from the inner edge into a high-latitude outflow (§4.2.4). Despite our torus being magnetized, this outflow is not a magnetocentrifugal wind since closed loops of sub-thermal magnetic field are passively drawn out by the outflow (§4.2.6).

Königl & Kartje (1994) acknowledged the importance of IR and UV radiation pressure on dust, but Everett

(2005) was the first to study how an AGN-like spectrum photoionizes a magnetocentrifugal wind and deposits momentum through atomic absorption. He put shielding gas of arbitrary column density into the model to prevent overionization of the wind, but omitted dust, which could also influence photoionization by removing UV radiation. Keating et al. (2012) expanded the work of Everett (2005) by adding dust opacity and momentum transfer from dust absorption. Neither model considers pressure on dust from reprocessed IR radiation, which transmits momentum and energy deposited by UV radiation throughout the torus, and which our simulation identifies as critical for maintaining an outflow at $\tau_{\rm UV} \gtrsim 1$ (§4.2.4).

Elitzur & Shlosman (2006; see also Kartje et al. 1999) examined another variation on the magnetocentrifugal wind, one in which dusty gas is clumped; the authors assumed clumps are individual entities and touched on how they may be magnetically confined. Our simulation sheds light on both issues. The first and second panels of the bottom row of Figure 4.2 depict the inhomogeneous density distribution in the wings and the wind, which obscure at high latitudes (§4.3.2). We find wedges of various densities in the wind, density ridges in the wings, and even a hook-shaped feature near the top of the second panel. Our simulation therefore underlines the point that the common picture of spherical, well-separated clumps must not be taken too seriously. Furthermore, density perturbations in our torus are not static or stationary structures confined externally by gas or magnetic pressure, or internally by self-gravity; they are imprinted in the wind by bursty wind launching (§4.2.3), and in the wings by bursts of newly launched, faster gas shocking with slower gas further out (§4.2.1). Density perturbations are ephemeral; only by virtue of their frequent recurrence in the same place with the same morphologies do they become distinguishing features of the torus. This challenges the notion that a clumpy torus must consist of properly confined clumps that persist for multiple orbits.

Wada (2012; 2015; see also Schartmann et al. 2014; Wada et al. 2016) explored the idea of a gas fountain powered by the central source through UV radiative acceleration, X-ray photoionization heating, and Compton heating; the neglect of heating by UV radiation from the central source in these simulations precludes the treatment of thermal IR radiation. When gas in these simulations moves out of the central hole, it receives reduced radiative acceleration and falls back to the mid-plane; this could be because these simulations ignore IR radiation, which spreads momentum and energy throughout the torus and drives an outflow at $\tau_{\rm UV} \gtrsim 1$. Note that Wada et al. (2016) combined turbulence generated by supernovae (Wada & Norman 2002) with driving by the central source, but stars cannot make gas geometrically thick on parsec scales (Krolik & Begelman 1988).

Dorodnitsyn & Kallman conducted a series of simulations to investigate whether IR radiation pressure on dust can create a geometrically thick torus. Our simulation best resembles those by Dorodnitsyn et al. (2012): Their simulations have IR radiation driving a wide-angle outflow, while ours have IR and UV working in concert to achieve the same effect. However, there are also important differences between the two sets

of simulations. Their simulations postulate a razor-thin accretion disk as a mass source for the outflow, the characterization of which introduces additional free parameters that are not self-consistently determined by the simulation; we avoid this by putting all the mass in the simulation domain right at the start and letting it develop structures on its own. The outflow in their simulations originates from across the entire accretion disk because their mid-plane boundary condition assures so; in our simulation, where no such boundary condition is assumed, gas is launched into the outflow exclusively at the torus inner edge. Finally, the IR-driven outflow in their simulations is a failed wind that apparently falls back to the mid-plane. Our simulation with both IR and UV radiation tells a different story: The UV-driven outflow at $\tau_{\rm UV} \lesssim 1$ is gravitationally unbound, and at least part of the IR-driven outflow at $\tau_{\rm UV} \gtrsim 1$ is unbound.

The later simulations by Dorodnitsyn & Kallman (2012) and Dorodnitsyn et al. (2016) consider how the central source deposits momentum through UV radiation, and momentum and energy through X-rays; they diverge markedly from the simulations by Dorodnitsyn et al. (2012) and from ours. In both their simulations and ours, IR radiation is created when the central source heats dust; the difference is that in our simulation, heating through UV radiation is concentrated at the inner edge (§3.2.3), whereas in their simulations, heating is more widespread because it is due to X-rays, not UV radiation. In their simulations, UV radiation transfers momentum solely through lines; this implies that the authors were looking at a different situation from ours, namely, one with a dust-free central hole. Now the timescale for dust destruction by sputtering at gas temperature $\sim 10^5$ K is $\sim 100\,[n_{\rm H}/(10^6\,{\rm cm}^{-3})]^{-1}\,[a/(0.1\,\mu{\rm m})]$ yr, where $n_{\rm H}$ and a are the number density of hydrogen atoms and the radius of dust grains respectively (Draine & Salpeter 1979; Tielens et al. 1994), and it decreases sharply at higher temperatures until $\sim 10^7$ K to $\sim 10^{7.5}$ K. This is not very different from the time it takes for the UV-driven wind to escape from the inner edge to infinity: Assuming the inner edge is at $R = R_{\rm in}$ and the wind terminal speed v_∞ is given by Equation (3.15), the time is

$$\frac{R_{\rm in}}{v_\infty} \sim 55 \left(\frac{M}{10^7\,M_\odot}\right)^{1/4} \left(\frac{L_{\rm UV}/L_{\rm E}}{0.1}\right)^{1/4} \left(\frac{\kappa_{\rm IR}/\kappa_{\rm T}}{20}\right)^{-3/4} \left(\frac{\kappa_{\rm UV}/\kappa_{\rm T}}{2000}\right)^{1/4} \left(\frac{R_{\rm in}}{r_{\rm ds}}\right)^{3/2} {\rm yr}. \tag{4.12}$$

Therefore, whether dust is present in the central hole depends sensitively on how quickly cold gas evaporated from the inner surface heats up to the Compton temperature. Lastly, photoionization heating in their simulations produces a hot atmosphere that envelopes and vertically compresses their tori; therefore, IR radiation can only push an outflow along, not far above, the mid-plane. Although our simulation does not explicitly constrain pressure from photoionized gas in the central hole, we can estimate its effect by computing the ionization parameter $\Xi \equiv L_{\rm ion}/(4\pi r^2 c p_{\rm tot})$, where $L_{\rm ion}$ and $p_{\rm tot}$ are the ionizing luminosity and total pressure respectively (Krolik et al. 1981); AGN photoionization calculations indicate that Ξ locks in at ~ 10 if, as here, a cool gas reservoir is present (Krolik & Kriss 2001). If we take $L_{\rm UV} \sim L_{\rm ion}$, we find that Ξ in the head, body, wings, and wind are ~ 1, ~ 2, ~ 2.5, and ~ 1.2 respectively. Unlike in their simulations, our torus has too high

pressure to be confined by photoionized gas; rather, its geometrical thickness is limited primarily by gravity.

Taken together, we find that our simulation is superior to previous tori models in that it invokes far fewer assumptions. Unlike the magnetocentrifugal wind, our simulation does not presume a mass loading mechanism; its chief free parameter is $L_{\rm UV}/L_{\rm E}$. With the bare minimum of physics, to wit, momentum and energy coupling between gas, IR radiation, and UV radiation, our simulation demonstrates that radiation on its own can propel an outflow far above the mid-plane; a strong magnetic field steering gas to high latitudes, as in the case of a magnetocentrifugal wind, is unnecessary. Moreover, our simulation distinguishes itself from gas fountain models by showing that IR radiation is pivotal in delivering momentum and energy, thereby driving an outflow, at $\tau_{\rm UV} \gtrsim 1$. Photoionization heating in the central hole and Compton heating deep inside the torus are higher-order corrections to the overall torus geometry.

Our simulation also highlights a couple little-appreciated aspects of tori. Widespread adoption of clumpiness in RT models is not matched by an equal level of sophistication in characterizing individual clumps: Clumps are almost invariably taken to be spherical, discrete, and confined by pressure or self-gravity. Our simulation offers the alternative viewpoint that fleeting, irregular density perturbations can arise simply from cool gas being accelerated to high speeds by radiation pressure, then shocking with slower gas. In terms of global torus dynamics, our simulation suggests that hydrostatic IR-supported tori, such as envisioned by Krolik (2007), may not remain so when the conversion of UV radiation to the IR is treated self-consistently; instead, what transpires is a flow along the mid-plane to the inner edge, and from there on into the outflow. Our simulation recognizes two quantities, the mass resupply rate and the angular momentum profile, as defining quantities of the flow; these quantities have never been explicitly considered by previous dynamical torus models (but see Roth et al. 2012; Schartmann et al. 2014).

4.4 Summary

We have performed three-dimensional, time-dependent RMHD simulations of AGN tori featuring quality RT and simultaneous evolution of gas and radiation. For the first time, our torus achieves a "steady" state lasting for more than an orbit at the inner edge, and potentially for much longer. This "steady" state is characterized by the torus having constant overall morphology (§4.2.3). It is obtained by reducing the angular momentum profile before the simulation starts, which has the dual effect of raising the total binding energy and bringing gas with high binding energy toward the inner edge (§4.1.1.3).

The existence of a "steady" state is significant: While tori in previous simulations could not endure UV irradiation for more than two orbits at the inner edge (§3.2.1), the current simulation demonstrates that a torus with the right parameters can indeed remain in a steady state for multiple orbits (§4.2.2). Granted that our

torus cannot formally reach equilibrium owing to our choice of $\kappa_{\rm UV}$ (§3.3.3) and to computational cost, we can already learn much from its approximate "steady" state that would conceivably carry over to the true steady state. Moreover, the ability to study the torus in a quasi-stationary state boosts our confidence in separating the "steady" state from transitory behavior.

We perceive four persistent structures in the torus, namely, head, body, wings, and wind (§4.2.3). Vertical support against gravity is dominated by gas pressure in the head and the body, IR radiation pressure in the wings, and UV radiation pressure in the wind (§4.2.4). By inspecting the forces driving the flow, we realize that these structures are not hydrostatic. Instead, gas falls toward the inner edge due to insufficient support against gravity, and flies outward from the inner edge due to UV radiative acceleration (§4.2.4); the structures represent parts of this journey common to most gas.

The study of forces allows us to clarify the subtle role IR radiation plays in torus dynamics. It opens up the central hole (§4.2.3), partially supports the body and the lower parts of the wings in the vertical direction (§4.2.4), and drives an outflow in the wings at $\tau_{\rm UV} \gtrsim 1$ where UV radiative acceleration fails (§4.2.4).

It is reassuring to see that most statements pertaining to RHD tori are valid here as well: The torus focuses IR radiation toward the axis (§4.2.5), and the outflow has a mass loss rate and wind terminal speed consistent with observations (§4.3.3.1). The strong resemblance between RHD and RMHD tori also suggests that although magnetic field in our simulation can create small-scale inhomogeneities (§4.2.3), its effect on larger scales is essentially nil within two orbits at the inner edge. This contrasts with realistic tori, in which magnetic stresses could redistribute angular momentum over many orbits and thereby set the steady-state angular momentum profile.

Observational predictions can be more easily made for a torus in "steady" state. When seen face-on, the temperature profile of our torus should follow the radially outward temperature gradient of the body; this gradient is $T \propto R^{-0.73}$ for our torus. When seen edge-on, a jump in temperature should be seen at high altitudes (§4.3.1). The tenuous wings and wind block soft X-rays, IR radiation, and UV radiation from the central source, while the denser head and body also stop hard X-rays. The X-ray, IR, and UV covering fractions are all $\approx \frac{3}{4}$, which is close to the observed fraction of type-2 AGNs (§4.3.2). Furthermore, if we assume AGNs have a finite range of mid-plane column densities, then our torus also naturally explains why the distribution of observed AGN gas columns over logarithmic column density is flat (§4.3.3.4).

The only freedom we have in constructing our torus is the initial angular momentum profile; yet, with practically no fine tuning of parameters, we arrive at a torus whose obscuration properties agree fairly well with observations. A wide-angle torus outflow driven by a combination of IR and UV radiation is therefore an attractive model for geometrically thick obscuration in AGNs.

CHAPTER 5

CONCLUSIONS

> Humans may crave absolute certainty; they may aspire to it; they may pretend, as partisans of certain religions do, to have attained it. But the history of science—by far the most successful claim to knowledge accessible to humans—teaches that the most we can hope for is successive improvement in our understanding, learning from our mistakes, an asymptotic approach to the Universe, but with the proviso that absolute certainty will always elude us.
> We will always be mired in error. The most each generation can hope for is to reduce the error bars a little, and to add to the body of data to which error bars apply. The error bar is a pervasive, visible self-assessment of the reliability of our knowledge.
>
> Carl Sagan, *The Demon-Haunted World: Science as a Candle in the Dark*

It is time to reflect on the preceding chapters and extract from our RHD (Chapter 3) and RMHD (Chapter 4) simulations physical insights that may be valid for various kinds of radiation-supported tori. We also contemplate what the next steps in torus simulations may be.

5.1 Lessons from RHD and RMHD simulations

Our experience with simulations taught us that simulations are never just about solving differential equations with computers. More often than not, simulations have to be performed with less than ideal parameters and resolutions, and numerical algorithms are prone to introduce artifacts. Faced with such noisy data, we must call upon our judgement to separate out the parts that hint at true phenomena, those amenable to explanation by simple physical principles. This exercise requires a lot of experience, a touch of insight, and patience to spare.

5.1.1 Structure and dynamics of tori under irradiation

The torus in our RHD and RMHD simulations possesses a number of features that stand prominently above the simulation noise, which we recapitulate below.

Our simulations consider the interaction among gas, IR radiation, and UV radiation. This is absolutely the minimal amount of physics needed to investigate the response of a dusty torus to UV irradiation; other processes, such as photoionization heating and Compton heating, merely perturb these first-order results (§4.3.4). Among torus simulations, ours are the first to employ a genuine RT module for IR radiation, one that solves the time-dependent RT equation on a large number of grid rays without resorting to approximate closure schemes (§2.1). Our simulations also pioneer the self-consistent treatment of the conversion of UV radiation to the IR, instead of relying on arbitrary radiative boundary conditions as a source for IR radiation (Chapter 2).

The torus develops structures that are surprisingly robust to our choice of parameters and initial conditions. The initial conditions of our RHD and RMHD simulations are set up in two unrelated ways (§§3.1.1 and 4.1.1.1), and they differ in the mid-plane angular momentum profile $j(R)$ (§§3.1.1, 4.1.1.1 and 4.1.1.3) as well as the mid-plane Thomson optical depth $\tau_{\rm T}$ (§§3.1.1 and 4.1.1.4). Yet if we look closely at Figure 3.1 for our RHD simulations, we find temporary structures that resemble the head, body, wings, and wind identified in our RMHD simulations (§4.2.3). Such striking similarities arising from different setups is a hint that they are no mere numerical happenstance; indeed, the four structures may have counterparts in realistic tori.

Analogous structures appear in the two sets of simulations because they have qualitatively the same force distributions (§§3.2.1 and 4.2.4) and hence gas flow patterns. The prevalent flow can be broken up into three legs: Gas from large distances falls radially inward and vertically toward the mid-plane until it reaches the body; it travels radially inward and horizontally through the body to the head; finally, it is launched from the inner edge of the head into the wind or the wings (§§3.2.1 and 4.2.4). The structures are not hydrostatic, but regions with distinctive shapes and velocities that most gas passes through. With the right parameters, such as in our RMHD simulations, the structures can even be long-lived (§4.2.2).

Radiation drives a geometrically thick outflow in our simulations in spite of the geometrical thinness of the head and the body (§§3.2.4 and 4.2.4). The outflow is initially launched from the inner edge by UV radiation (§§3.2.1 and 4.2.3). Part of it continues on as a wind in the central hole at $\tau_{\rm UV} \lesssim 1$, where $\tau_{\rm UV}$ is the UV optical depth from the central source; part of it is pushed by radiative and centrifugal accelerations to the wings at $\tau_{\rm UV} \gtrsim 1$, and further accelerated by IR radiation diffusing outward from the central hole (§4.2.4). IR and UV radiation work hand in hand to deliver a wide-angle outflow with no discontinuity in momentum flux across $\tau_{\rm UV} = 1$ (§4.2.4). Whether this outflow reaches galactic scales depends on the distribution of gas on larger scales, on which our simulations cannot comment (§4.2.4).

The torus in our simulations traps IR radiation in the central hole. Since the mid-plane is the most optically thick, IR radiation preferentially escapes the central hole at high latitudes (§§3.2.3 and 4.2.5); consequently, the IR radiative flux in the axial direction is boosted by a factor of $\sim C_{\rm IR}/(1-C_{\rm IR})$, with $C_{\rm IR}$ being the IR covering fraction (§3.3.1). The concentration of IR radiative flux toward high latitudes means the outflow in the wings are faster than if IR radiative flux were spherically symmetric.

One reason why we distinguish between the structures is because of their different obscuration properties. In the "steady"-state of the IR-RMHD stage of our RMHD simulations, the tenuous wings and wind at high latitudes obscures the central source in soft X-rays, the IR, and the UV, while the dense head and body along the mid-plane blocks hard X-rays as well (§4.3.2). The soft X-ray, IR, and UV covering fractions are all $\approx \frac{3}{4}$, while each decade of column density occupies roughly the same solid angle around the central source (§4.3.2). Both results are in excellent agreement with observations.

Our results must be extrapolated before they can be applied to realistic tori because our simulations adopt values of central mass M (§2.4.1) and UV opacity $\kappa_{\rm UV}$ (§2.3.6) much smaller than realistic. With higher M, the gas-supported head and body would become thinner, while the IR supported wings and UV-supported wind would retain their geometrical thickness (§4.3.3.2). The outflow in the wings and the wind are also robust with respect to an increase in M because they are powered by radiation, not by gas (§§3.2.1, 4.2.3 and 4.2.4). With higher $\kappa_{\rm UV}$, the wind is faster but limited to a thinner layer along the inner surface (§3.3.3).

The fiducial terminal speed and mass loss rate of the wind, scaled to realistic values of M and $\kappa_{\rm UV}$, are $\sim 5000\,[M/(10^7\,M_\odot)]^{1/4}[L_{\rm UV}/(0.1\,L_{\rm E})]^{1/4}\,{\rm km\,s^{-1}}$ and $\sim 0.1\,[M/(10^7\,M_\odot)]^{3/4}[L_{\rm UV}/(0.1\,L_{\rm E})]^{3/4}\,M_\odot\,{\rm yr^{-1}}$ (§3.3.3); here $L_{\rm UV}$ and $L_{\rm E}$ are the UV and Eddington luminosities of the central source respectively. If we combine the outflows through the wings and the wind in the "steady" state of the IR-RMHD stage of our RMHD simulations, we find that the mass loss rate is a factor of ~ 3 greater than its fiducial value, while the wind terminal speed is the same factor smaller (§4.3.3.1); therefore, both quantities in our RMHD simulations match observations quite nicely (§3.3.3).

We took little liberty in parameter selection. All torus models must involve some choice of M and $L_{\rm UV}/L_{\rm E}$, as well as a gas density scale, which is parametrized by $\tau_{\rm T}$. Our values of $L_{\rm UV}/L_{\rm E}$ (§§3.1.4 and 4.1.3) and $\tau_{\rm T}$ (§§3.1.4, 4.1.1.3 and 4.1.1.4) are based on observations. Our small M prevents numerical artifacts (§2.4.1), and has the additional benefit of allowing the all-important gas dynamics in the vicinity of the inner edge to be resolved; in contrast, the mid-plane structures in most other simulations are a couple cells thick (Wada 2012, 2015; Schartmann et al. 2014; Wada et al. 2016; Namekata & Umemura 2016). The only true arbitrariness in our RMHD simulations is $j(R)$; here, our simulations demonstrate that "steady" state can be secured by modifying the initial $j(R)$ (§4.2.2).

We conducted our simulations with few preconceived notions about torus dynamics. Unlike in the case of

the magnetocentrifugal wind (Königl & Kartje 1994), or the previous RMHD torus simulations (Dorodnitsyn et al. 2011, 2012; Dorodnitsyn & Kallman 2012), nowhere in the setting up of our simulations did we anticipate an outflow, nor do we allow for artificial mass resupply. The torus nevertheless reorganizes itself into an inflow–outflow as described above (§§3.2.1 and 4.2.4); the outflow, in particular, is directed toward high latitudes and has obscuration properties similar to realistic tori (§4.3.2). The spontaneous appearance of a wide-angle, obscuring outflow propelled by IR and UV radiation suggests that this could be the explanation of geometrically thick obscuration in AGNs.

5.1.2 Physics of tori under irradiation

Simulations cover a very limited subset of the parameter space, so it is imperative that we deduce physical principles from them that generalizes to a broader range of circumstances.

It is easy to see why an inflow–outflow should be expected for a long-lived torus. If a torus is supported in the mean against gravity, then in general there are regions that are over-supported, and there are regions that are under-supported; the hydrostatic case where every region is marginally supported is the exception rather than the rule. Suppose further that support is mainly furnished by rotation and by radiation from a central source; since density and hence optical depth typically decline with latitude, radiation pressure should be stronger at higher latitudes, so the inner surface should be over-supported (§3.2.1), while the mid-plane should accordingly be under-supported. The result is an inflow along the mid-plane feeding into an outflow along the inner surface.

Mass loss is a direct consequence of parts of the steady-state torus receiving much more momentum from radiation than other parts. Mass loss limits the lifetime of an isolated torus by directly removing its gas; in doing so, it also reduces the mid-plane optical depth of the torus, making it easier for IR radiation to expel the torus as a whole along the mid-plane (§3.2.1). For these reasons, none of our RHD simulations has a torus remaining within the simulation domain for a long time (§3.2.1). A torus can only be long-lived if there is a constant stream of gas from galactic scales to the inner edge (§3.3.4). Mass resupply is therefore an essential ingredient of a steady-state torus, yet previous dynamical torus models have either left out the relevant discussion (e.g., Wada 2012; Dorodnitsyn et al. 2016; Namekata & Umemura 2016; but see Schartmann et al. 2014), or imposed as a boundary condition an accretion disk that serves as a mass source for the outflow without self-consistently solving for the properties of the accretion disk under irradiation (e.g., Königl & Kartje 1994; Dorodnitsyn et al. 2012). Our simulations are therefore the first to put the issue in the limelight.

Another essential property of the torus is its mid-plane angular momentum profile $j(R)$. In the simplest case of a hydrostatic, geometrically thick torus supported against gravity by an isotropic pressure, the torus

must have a sub-Keplerian $j(R)$ regardless of the nature of the pressure. In the case of an inflow–outflow illuminated by a central source, the argument is more complicated. The same logic as in the hydrostatic case applies with a caveat: The mid-plane inflow may be supported by an isotropic pressure, but the high-latitude outflow certainly is not (§4.2.5), so only the geometrical thickness of the former is pertinent. Moreover, since radiation deposits radially outward momentum on the torus, the torus should have lower $j(R)$ in order to stay in steady state (§4.1.1.3). Dorodnitsyn et al. (2011) remarked that rotation can be non-Keplerian if there are forces besides gravity, and Dorodnitsyn et al. (2016) chose an arbitrary $j(R)$ in their initial condition, but the rest of the torus dynamics literature assumes that rotation is identically Keplerian. This work is the first to recognize that a steady state demands sub-Keplerian rotation, and that its R-dependence is critical to dynamics. We do not know what physical processes determine steady-state $j(R)$ in realistic tori; since magnetic fields are present on torus length scales (Lopez-Rodriguez et al. 2015), magnetic stresses could redistribute angular momentum throughout the torus until steady-state $j(R)$ obtains.

UV and IR radiation do positive work on the outflows in the wind (§4.1.1.3) and the wings respectively; this lowers the binding energy of the torus in our simulations, leading to its ultimate demise as radiation shoves the torus radially outward in collective motion (§4.2.2). Binding energy is an important and thus far overlooked aspect of torus dynamics, but it is unclear how we can translate what we learn from our simulations to realistic tori. There may be a mechanical energy balance in realistic steady-state tori: Radiation adds energy to the system, while outflows and stresses remove it. Stresses could be internal to the inflow and transport energy outward along the mid-plane. The outflow could either directly advect energy away, or stresses in the magnetized outflow could take sap energy from the system (Blandford & Payne 1982; Königl & Kartje 1994).

Gas in our simulations is sent into the obscuring outflow only from the inner edge; therefore, conditions at the inner edge determines to a large extent the initial launch angle of the gas, and hence the latitude span of the outflow and the covering fraction of the torus. This has implications for both simulations and realistic tori. In terms of simulations, high enough spatial resolution to resolve the small-scale inner edge is imperative for getting the correct large-scale outflow behavior. Furthermore, since all that matters for the outflow is the inner edge, we may arrive at an outflow with similar properties had we started with a geometrically thin initial condition. In terms of realistic tori, an outflow of the kind we described, if it exists, would be insensitive to the mechanism by which gas feeds onto the torus as long as there is an inner edge for gas to be blown off from.

5.1.3 Variation of torus parameters

The three chief parameters characterizing an isolated, irradiated torus are the Eddington ratio $L_{\rm UV}/L_{\rm E}$ of the central source, the mid-plane Thomson optical depth $\tau_{\rm T}$, and the mid-plane angular momentum profile $j(R)$

(see also §3.3.2). Roughly speaking, the goal of torus simulations is to find some surface of stationary in this parameter space, the surface on which tori neither shrinks immediately to small scales, nor disperses quickly under radiative acceleration, but survives for a long time near the dust sublimation surface.

Our RHD simulations vary $L_{\rm UV}/L_{\rm E}$, and the UV-RMHD stage of our RMHD simulations varies $j(R)$. We find locally optimal values for both parameters: In the RHD simulations where $j(R) \propto R^{1/2}$ and $\tau_{\rm T} \approx 1.11$, the inner edge stays near the dust sublimation surface for the longest for $L_{\rm UV}/L_{\rm E} = 0.11$ (§3.2.1); in the UV-RMHD stage of the RMHD simulations where $L_{\rm UV}/L_{\rm E} = 0.1$ and $\langle\tau_{\rm T}\rangle = 1$, the survival time is the longest for $j(R) \propto R^0$ (§4.2.2). The general trend for either parameter is obvious: too high, and the torus is easily blown away by radiation; too low, and the torus collapses promptly, possibly forming some stable structure whose size is too small to be of interest to us (§§3.2.1 and 4.2.2).

The dependence of the radial motion of the torus on $L_{\rm UV}/L_{\rm E}$ and $j(R)$ suggests a revision to the way we think about geometrically thick tori. Whenever we discuss vertical support in tori, we often focus on how gas is hoisted above the mid-plane; however, if radiation can always create a wide-angle outflow, then the attention on vertical motion may be misplaced, and we should rather study what radial motion results from a particular choice of $L_{\rm UV}/L_{\rm E}$ and $j(R)$, and whether this radial motion would keep the inner edge near the dust sublimation radius.

We can regard $\tau_{\rm T}$ as a proxy for torus mass. At fixed $L_{\rm UV}/L_{\rm E}$ and $j(R)$, we suspect there is an optimal value for $\tau_{\rm T}$: Below this value, increasing $\tau_{\rm T}$ would allow the torus to withstand mass loss and survive longer; above this value, the torus would be too massive to be supported at constant $L_{\rm UV}/L_{\rm E}$, so it would swiftly fall through the dust sublimation surface. We only have concrete evidence for the first half of this assertion from the UV-RMHD stage of our RMHD simulations, in which two simulations with the same $L_{\rm UV}/L_{\rm E}$ and $j(R)$ are initialized with $\langle\tau_{\rm T}\rangle = 1$ and $\langle\tau_{\rm T}\rangle = 2$ respectively (§4.1.1.3).

5.1.4 Implications for realistic tori

We conduct torus simulations in order to learn about what physical processes sculpt realistic tori. We have already mentioned how our simulations bear on the anisotropy of IR radiation, obscuration properties, and outflow kinematics of realistic AGNs in §5.1.1; here we explore a few areas that go beyond what is directly simulated and thus is more speculative in nature.

Because density distribution is uneven at the inner edge where the wind is launched, the upper parts of the $\tau_{\rm UV} = 1$ surface in our simulations swings back and forth in latitude; as a result, in the "steady" state of the IR-RMHD stage of our RMHD simulations, $\approx 7\%$ of the solid angle around the central source transitions repeatedly between optically thin and thick in the UV (§4.2.3). This brings to mind the case of changing-look

quasars, whose optical classification switches between type-1 and type-2 over $\sim 10\,\mathrm{yr}$ (e.g., Shappee et al. 2014; LaMassa et al. 2015), or with frequency $\nu \approx (0.002 P_{\mathrm{orb}})^{-1}$, where

$$P_{\mathrm{orb}} \equiv 2\pi \left(\frac{GM}{r_{\mathrm{ds}}^3}\right)^{-1/2} \approx 4900 \left(\frac{M}{10^7\,M_\odot}\right)^{1/4} \left(\frac{L_{\mathrm{UV}}/L_{\mathrm{E}}}{0.1}\right)^{3/4} \left(\frac{\kappa_{\mathrm{UV}}/\kappa_{\mathrm{IR}}}{100}\right)^{3/4} \mathrm{yr} \tag{5.1}$$

is the orbital period at the dust sublimation radius. If the opening angle of a pure RHD torus fluctuates, it should do so on the dynamical timescale, which is the timescale on which gravity and radiation drive the system; in contrast, there could be multiple timescales for opening-angle fluctuations in an RMHD torus, ranging from the turbulent dissipation timescale to the dynamical timescale. It is also possible that different timescales govern the opening and closing of the central hole: The timescale of a decrease in opening angle could be controlled by how rapidly density varies at the inner edge, which determines how often a burst of dusty gas is launched into the central hole; the timescale of an increase in opening angle could depend on how quickly said gas stretches out until it becomes optically thin, and how quickly it moves horizontally outward due to centrifugal, gas pressure, or IR radiative accelerations. All these timescales are difficult to estimate from first principles. To investigate the timescale of opening-angle fluctuations in our RMHD simulations, we construct periodograms for latitude fluctuations of the $\tau_{\mathrm{UV}} = 1$ surface at fixed azimuths in the "steady" state of the IR-RMHD stage. We find that the frequency dependence of fluctuation power is closely approximated by $P \propto \nu^{-2.8}$ between $\nu \approx (0.8 P_{\mathrm{orb}})^{-1}$ and $\nu \approx (0.035 P_{\mathrm{orb}})^{-1}$; in other words, we cannot detect a characteristic timescale within the frequency range our simulation can reliably probe. Note that our simulation does not run long enough for us to comment on variations at frequency $\nu \sim P_{\mathrm{orb}}^{-1}$. Furthermore, the steepness of the power law means that our simulation produces little power at the observed $\sim 10\,\mathrm{yr}$ timescale of changing-look quasars, but it could be that a change in optical type occurs only during a small portion of a much longer cycle of opening-angle fluctuations, when the $\tau_{\mathrm{UV}} = 1$ surface happens to cross our sightline.

Let us consider the accretion rate onto the SMBH needed to drive our outflow. An accretion rate of $\dot{M}$ generates a luminosity of $\sim \dot{M}c^2$; if we assume the momentum of this radiation is passed on fully to the outflow, and if the outflow has terminal speed equal to the orbital velocity v_ϕ at its launch point, then the mass outflow rate is simply $\sim \dot{M}c^2/(cv_\phi) = (c/v_\phi)\dot{M}$. Since $v_\phi \ll c$ at the torus inner edge, a small amount of accretion from the torus to the SMBH suffices to propel a massive outflow. A more careful calculation would incorporate the accretion efficiency, the UV covering fraction, and the number of times IR radiation bouncing around the central hole transfers momentum to the gas (§3.2.3), but our qualitative argument still stands. Even this small amount of accretion is not seen in our simulations. In the IR-RMHD stage of our RMHD simulations, the vast majority of the inflowing gas is blasted into the outflow at the inner edge. The IR-RMHD stage begins with some gas inside the dust sublimation surface left over from the earlier stages; as time goes on, this gas is either launched into the outflow or accreted through the inner-radial boundary, and since this gas is not

replenished, accretion peters out. The lack of accretion is a consequence of our simplifying assumptions that the central source radiates isotropically (§2.3.5), and that the region interior to the dust sublimation surface is totally transparent. The situation could be very different in realistic tori, with multiple agents influencing the accretion rate from the inner edge. Balsara & Krolik (1993) showed that the Eddington ratio of the central source regulates the fraction of gas captured from the tori, but their simulations ignore rotation. Other primary factors are the presence of stresses capable of redistributing angular momentum and the thermodynamics of the accreting gas; corrections can arise from the anisotropy of radiation from the accretion disk (e.g., Netzer 1987), the alignment of the accretion disk with the torus, and the opacity between the SMBH and the inner edge.

It bears reiterating that our simulations only focus on one mechanism of outflow driving, namely, IR and UV radiative pressure. Other mechanisms certainly exist, a popular one being the thermally driven wind (Begelman et al. 1983) launched from the inner surface of the torus (Krolik & Begelman 1986; Balsara & Krolik 1993; Krolik & Kriss 2001; Blustin et al. 2005). The radiation-driven outflow and thermally driven wind are quite different: the former is cold but the latter is at the Compton temperature (Krolik et al. 1981); the former contains obscuring dust but the latter does not. Nevertheless, since the two outflows have similar kinematic properties (§3.3.3), they are equally important in the torus context. We envision the NLR region in realistic tori to be the photoionized, dust-free central hole along the axis, which the thermally driven wind more or less evenly fills out; density in the central hole is low both because UV radiation expels the gas, and because the centrifugal barrier prevents gas from getting too close to the axis. The central hole is ensconced by a thick wall of dusty outflow that spans a wide range of latitude from $\tau_{\rm UV} \sim 1$ to $\tau_{\rm IR}$ of a few, as it does in our simulations. Note that similar pictures for the torus have been proposed before. Braatz et al. (1993) interpreted the extended axial MIR emission in NGC 1068 as NLR dust heated directly by the central source. Hönig et al. (2012) presented a model in which dust clumps line the conical edge of the NLR; they argued that if emitters were arranged in a hollow cone, then limb brightening would naturally explain the apparent association of the MIR emission in Circinus with the boundary of the axial outflow region. Our torus resembles this latter model quite well, with the main difference being that our dusty outflow is not just along the inner surface, but has a latitude spread.

5.2 Future directions

Our simulations are of course not the final word on geometrically thick tori; here we present a list of ideas, in decreasing order of practicality, on how we may proceed.

We now have a "steady"-state RMHD torus model, whose X-ray, IR, and UV covering fractions as well as

distribution of column densities over solid angle generally agree with observations (§4.3.2). It is worthwhile to perform multi-frequency RT transfer on a snapshot of the simulation and derive more accurate and detailed observational predictions. We could measure X-ray, IR, and UV optical depths as functions of latitude and azimuth, which yield the covering fractions at these frequencies. For an arbitrary observer, we could also compute SEDs over the plane of the sky and derive the observed IR temperature gradient of the torus. We may want to crop the simulation domain to, say, a sphere of radius $r = 3\,r_0$, before performing RT; this is to prevent RT from being biased by the "steady"-state body not reaching the outer-radial boundary of the simulation domain (§4.2.5).

Carrying $c_s^2 \sim GM/r$ from the MHD stage over to the UV-RMHD stage may not be the best choice because higher c_s prevents the central hole from opening (§4.2.3) and gas from collapsing into the head and the body (§4.2.4), both essential features of the IR-RMHD stage. It could be enlightening to run a simulation in which $c_s^2 \sim k_B T_{ds} \ll GM/R_{in}$ already in the UV-RMHD stage; this way, gas would evolve in the UV-RMHD stage toward the configuration it eventually assumes in the IR-RMHD stage. As the simulation graduates to the IR-RMHD stage, instead of replacing gas pressure by IR radiation pressure, we simply put in IR radiation as appropriate for the gas temperature in each cell. The sudden addition of IR radiation pressure may excite a weaker transient than those arising from the widening of the central hole, and from the radial and vertical collapse into the head and the body.

The logical next step in our iterative approach to torus simulations (§1.2) would be to include photoionization by UV radiation in the central hole, as well as photoionization heating and Compton heating by X-rays throughout the simulation domain. On the physical side, additional sources of momentum and internal energy could affect the temperatures and shapes of the central hole (§2.2) and the torus (§4.3.3.5); this would affect the covering fraction and observed IR temperature of the torus. On the technical side, implementing these effects in our simulations amounts to a trivial extension of our time-independent long-characteristics UV RT module (§2.3.5).

Our simulations treat IR radiation as a single frequency group whose opacity κ_{IR} is constant below dust sublimation, but in reality, IR opacity drops by a factor of a few as temperature falls from T_{ds} to $0.1\,T_{ds}$. Temperature in our simulations ranges from $\sim 1.5\,T_{ds}$ around the origin to $\sim 0.1\,T_{ds}$ along the outer-radial boundary, so the drop in opacity with temperature could have observable dynamical consequences for the torus, in terms of reduced support in the outer parts of the torus and limited acceleration of the outflow in the wings. The observed IR temperature could also be different because the observer can see deeper into the torus at lower frequencies (§4.3.1). On these grounds, we may be interested in experimenting with the temperature dependence of κ_{IR} below dust sublimation.

5.3 Final remarks

We made significant progress in understanding the dynamics of AGN tori using RHD and RMHD simulations with genuine RT. The torus in our simulations concentrates IR radiation toward the axis. The torus is not hydrostatic, but consists of a dense mid-plane inflow and a tenuous high-latitude outflow. The geometrically thin inflow is described by its mass resupply rate and angular momentum profile. The geometrically thick, radiation-driven outflow agrees with observed outflow kinematics and can explain the observed AGN obscuration statistics. These results are all the more remarkable considering that they are obtained with little fine-tuning.

Much remains to be done before we arrive at a comprehensive torus model. At each step of the iterative process, we must use our physical insight to pick the most pertinent effects to include in the simulations and distill general principles from the simulations. Blindly mixing in all physics and hoping for the best leads us nowhere.

Bibliography

Alfvén, H. 1942, Natur, 150, 405

Amanatides, J., & Woo, A. 1987, in Eurographics '87, ed. G. Maréchal (New York: North-Holland), 3

Anderson, K. S., & Kraft, R. P. 1969, ApJ, 158, 859

Antonucci, R. R. J., & Miller, J. S. 1985, ApJ, 297, 621

Antonucci, R. 1993, ARA&A, 31, 473

—. 2002, in ASP Conference Proceedings, IAU Colloquium 184: AGN Surveys, ed. R. F. Green, E. Ye. Khachikian, & D. B. Sanders, Vol. 284 (San Francisco, CA: Astronomical Society of the Pacific), 147, arXiv: astro-ph/0110343

Antonucci, R., Hurt, T., & Miller, J. 1994, ApJ, 430, 210

Asmus, D., Hönig, S. F., & Gandhi, P. 2016, ApJ, 822, 109

Asmus, D., Hönig, S. F., Gandhi, P., Smette, A., & Duschl, W. J. 2014, MNRAS, 439, 1648

Bahcall, J. N., Bergeron, J., Boksenberg, A., et al. 1993, ApJS, 87, 1

Balbus, S. A., & Hawley, J. F. 1991, ApJ, 376, 214

—. 1998, RvMP, 70, 1

Baldassare, V. F., Reines, A. E., Gallo, E., & Greene, J. E. 2015, ApJL, 809, L14

Balsara, D. S., & Krolik, J. H. 1993, ApJ, 402, 109

Barthel, P. D. 1989, ApJ, 336, 606

Barvainis, R. 1987, ApJ, 320, 537

Beckert, T., Driebe, T., Hönig, S. F., & Weigelt, G. 2008, A&A, 486, L17

Begelman, M. C., McKee, C. F., & Shields, G. A. 1983, ApJ, 271, 70

Bentz, M. C., Denney, K. D., Grier, C. J., et al. 2013, ApJ, 767, 149

Blaes, O. M., & Balbus, S. A. 1994, ApJ, 421, 163

Blandford, R. D., & Payne, D. G. 1982, MNRAS, 199, 883

Blustin, A. J., Page, M. J., Fuerst, S. V., Branduardi-Raymont, G., & Ashton, C. E. 2005, A&A, 431, 111

Bock, J. J., Neugebauer, G., Matthews, K., et al. 2000, AJ, 120, 2904

Böhringer, H., Voges, W., Fabian, A. C., Edge, A. C., & Neumann, D. M. 1993, MNRAS, 264, L25

Braatz, J. A., Wilson, A. S., Gezari, D. Y., Varosi, F., & Beichman, C. A. 1993, ApJL, 409, L5

Brandt, W. N., Laor, A., & Wills, B. J. 2000, ApJ, 528, 637

Burlon, D., Ajello, M., Greiner, J., et al. 2011, ApJ, 728, 58

Burtscher, L., Jaffe, W., Raban, D., et al. 2009, ApJL, 705, L53

Burtscher, L., Meisenheimer, K., Tristram, K. R. W., et al. 2013, A&A, 558, 149

Cameron, M., Storey, J. W. V., Rotaciuc, V., et al. 1993, ApJ, 419, 136

Chan, C.-H., & Krolik, J. H. 2016, ApJ, 825, 67

Chang, C. T. 1959, PhFl, 2, 656

Cid Fernandes, R., Heckman, T., Schmitt, H., González Delgado, R. M., & Storchi-Bergmann, T. 2001, ApJ, 558, 81

Clavel, J., Wamsteker, W., & Glass, I. S. 1989, ApJ, 337, 236

Crenshaw, D. M., & Kraemer, S. B. 2012, ApJ, 753, 75

Crenshaw, D. M., Kraemer, S. B., Boggess, A., et al. 1999, ApJ, 516, 750

Davies, R. I., Burtscher, L., Rosario, D., et al. 2015, ApJ, 806, 127

Davies, R. I., Müller Sánchez, F., Genzel, R., et al. 2007, ApJ, 671, 1388

Davis, S. W., Stone, J. M., & Jiang, Y.-F. 2012, ApJS, 199, 9

Dorodnitsyn, A., Bisnovatyi-Kogan, G. S., & Kallman, T. 2011, ApJ, 741, 29

Dorodnitsyn, A., & Kallman, T. 2012, ApJ, 761, 70

Dorodnitsyn, A., Kallman, T., & Bisnovatyi-Kogan, G. S. 2012, ApJ, 747, 8

Dorodnitsyn, A., Kallman, T., & Proga, D. 2016, ApJ, 819, 115

Draine, B. T., & Salpeter, E. E. 1979, ApJ, 231, 77

Draine, B. T. 2011, Physics of the Interstellar and Intergalactic Medium (Princeton, NJ: Princeton University Press)

Elitzur, M., & Ho, L. C. 2009, ApJL, 701, L91

Elitzur, M., Ho, L. C., & Trump, J. R. 2014, MNRAS, 438, 3340

Elitzur, M., & Shlosman, I. 2006, ApJL, 648, L101

Elvis, M. 2000, ApJ, 545, 63

Elvis, M., Wilkes, B. J., McDowell, J. C., et al. 1994, ApJS, 95, 1

Everett, J. E. 2005, ApJ, 631, 689

Fathi, K., Lundgren, A. A., Kohno, K., et al. 2013, ApJL, 770, L27

Fitch, W. S., Pacholczyk, A. G., & Weymann, R. J. 1967, ApJL, 150, L67

Gammie, C. F. 1996, ApJ, 457, 355

Ganguly, R., & Brotherton, M. S. 2008, ApJ, 672, 102

Garabedian, P. R. 1957, RSPSA, 241, 423

Gebhardt, K., Bender, R., Bower, G., et al. 2000, ApJL, 539, L13

Georgantopoulos, I. 2013, International Journal of Modern Physics Conference Series, 23, 1

Ghisellini, G., Foschini, L., Volonteri, M., et al. 2009, MNRAS, 399, L24

Gilli, R., Comastri, A., & Hasinger, G. 2007, A&A, 463, 79

Gnedin, N. Y. 2016, arXiv: 1607.07869

Gnedin, N. Y., & Abel, T. 2001, NewA, 6, 437

Goldreich, P., Goodman, J., & Narayan, R. 1986, MNRAS, 221, 339

González Delgado, R. M., Heckman, T., & Leitherer, C. 2001, ApJ, 546, 845

Goodrich, R. W. 1989, ApJ, 340, 190

Goulding, A. D., & Alexander, D. M. 2009, MNRAS, 398, 1165

Goulding, A. D., Alexander, D. M., Bauer, F. E., et al. 2012, ApJ, 755, 5

Greenhill, L. J., Gwinn, C. R., Antonucci, R., & Barvainis, R. 1996, ApJL, 472, L21

Haardt, F., & Maraschi, L. 1991, ApJL, 380, L51

Halpern, J. P. 1984, ApJ, 281, 90

Hasinger, G. 2008, A&A, 490, 905

Hawley, J. F., & Balbus, S. A. 1991, ApJ, 376, 223

Hawley, J. F., & Krolik, J. H. 2001, ApJ, 548, 348

Hawley, J. F., Richers, S. A., Guan, X., & Krolik, J. H. 2013, ApJ, 772, 102

Heckman, T. M., González-Delgado, R., Leitherer, C., et al. 1997, ApJ, 482, 114

Heymann, F., & Siebenmorgen, R. 2012, ApJ, 751, 27

Hönig, S. F., Beckert, T., Ohnaka, K., & Weigelt, G. 2006, A&A, 452, 459

Hönig, S. F., Kishimoto, M., Antonucci, R., et al. 2012, ApJ, 755, 149

Hönig, S. F., Kishimoto, M., Gandhi, P., et al. 2010, A&A, 515, 23

Hönig, S. F., Kishimoto, M., Tristram, K. R. W., et al. 2013, ApJ, 771, 87

Hopkins, P. F., Hayward, C. C., Narayanan, D., & Hernquist, L. 2012, MNRAS, 420, 320

Hopkins, P. F., Torrey, P., Faucher-Giguère, C.-A., Quataert, E., & Murray, N. 2016, MNRAS, 458, 816

Hueyotl-Zahuantitla, F., Palouš, J., Wünsch, R., Tenorio-Tagle, G., & Silich, S. 2013, ApJ, 766, 92

Jacquet, E., & Krumholz, M. R. 2011, ApJ, 730, 116

Jaffe, W., Meisenheimer, K., Röttgering, H. J. A., et al. 2004, Natur, 429, 47

Jiang, Y.-F., Davis, S. W., & Stone, J. M. 2013a, ApJ, 763, 102

Jiang, Y.-F., Stone, J. M., & Davis, S. W. 2012, ApJS, 199, 14

—. 2013b, ApJ, 767, 148

—. 2014, ApJS, 213, 7

Kaastra, J. S., Mewe, R., Liedahl, D. A., Komossa, S., & Brinkman, A. C. 2000, A&A, 354, L83

Kalberla, P. M. W., Burton, W. B., Hartmann, D., et al. 2005, A&A, 440, 775

Kartje, J. F., Königl, A., & Elitzur, M. 1999, ApJ, 513, 180

Kaspi, S., Brandt, W. N., Netzer, H., et al. 2000, ApJL, 535, L17

Keating, S. K., Everett, J. E., Gallagher, S. C., & Deo, R. P. 2012, ApJ, 749, 32

Khachikian, Eh. E., & Weedman, D. W. 1971, Afz, 7, 389

Kishimoto, M., Hönig, S. F., Antonucci, R., et al. 2009, A&A, 507, L57

Kishimoto, M., Hönig, S. F., Antonucci, R., et al. 2011a, A&A, 527, 121

Kishimoto, M., Hönig, S. F., Antonucci, R., et al. 2011b, A&A, 536, 78

Kishimoto, M., Hönig, S. F., Antonucci, R., et al. 2013, ApJL, 775, L36

Königl, A., & Kartje, J. F. 1994, ApJ, 434, 446

Kormendy, J., & Richstone, D. 1995, ARA&A, 33, 581

Koss, M. J., Assef, R., Baloković, M., et al. 2016, ApJ, 825, 85

Krolik, J. H. 1977, PhFl, 20, 364

Krolik, J. H., & Begelman, M. C. 1986, ApJL, 308, L55

Krolik, J. H., McKee, C. F., & Tarter, C. B. 1981, ApJ, 249, 422

Krolik, J. H., & Voit, G. M. 1998, ApJL, 497, L5

Krolik, J. H. 2007, ApJ, 661, 52

Krolik, J. H., & Begelman, M. C. 1988, ApJ, 329, 702

Krolik, J. H., & Kriss, G. A. 2001, ApJ, 561, 684

LaMassa, S. M., Cales, S., Moran, E. C., et al. 2015, ApJ, 800, 144

Laor, A. 2003, ApJ, 590, 86

Lawrence, A. 1991, MNRAS, 252, 586

Lawrence, A., & Elvis, M. 2010, ApJ, 714, 561

LeVeque, R. J. 1998, in Saas-Fee Advanced Courses, Computational Methods for Astrophysical Fluid Flow, ed. O. Steiner, & A. Gautschy, Vol. 27 (Berlin: Springer), 1

—. 2002, Finite Volume Methods for Hyperbolic Problems, Vol. 31, Cambridge Texts in Applied Mathematics (Cambridge: Cambridge University Press)

Levermore, C. D., & Pomraning, G. C. 1981, ApJ, 248, 321

Liang, E. P. T. 1979, ApJL, 231, L111

Liu, G., Zakamska, N. L., Greene, J. E., Nesvadba, N. P. H., & Liu, X. 2013, MNRAS, 436, 2576

López-Gonzaga, N., Burtscher, L., Tristram, K. R. W., Meisenheimer, K., & Schartmann, M. 2016, A&A, 591, A47

Lopez-Rodriguez, E., Packham, C., Jones, T. J., et al. 2015, MNRAS, 452, 1902

Lovelace, R. V. E., Romanova, M. M., & Biermann, P. L. 1998, A&A, 338, 856

Lowrie, R. B., Morel, J. E., & Hittinger, J. A. 1999, ApJ, 521, 432

Lynden-Bell, D. 1969, Natur, 223, 690

Lynden-Bell, D., & Pringle, J. E. 1974, MNRAS, 168, 603

Lynds, C. R. 1967, ApJ, 147, 396

MacAlpine, G. M. 1985, in Astrophysics of Active Galaxies and Quasi-Stellar Objects, ed. J. S. Miller (Mill Valley, CA: University Science Books), 259

Magorrian, J., Tremaine, S., Richstone, D., et al. 1998, AJ, 115, 2285

Maiolino, R., Marconi, A., & Oliva, E. 2001, A&A, 365, 37

Maiolino, R., & Rieke, G. H. 1995, ApJ, 454, 95

Malkan, M. A., Gorjian, V., & Tam, R. 1998, ApJS, 117, 25

Mason, K. O., Puchnarewicz, E. M., & Jones, L. R. 1996, MNRAS, 283, L26

Mathews, W. G., & Blumenthal, G. R. 1977, ApJ, 214, 10

Mathur, S., Wilkes, B., Elvis, M., & Fiore, F. 1994, ApJ, 434, 493

Matthews, T. A., & Sandage, A. R. 1963, ApJ, 138, 30

Meisenheimer, K., Tristram, K. R. W., Jaffe, W., et al. 2007, A&A, 471, 453

Merloni, A., Bongiorno, A., Brusa, M., et al. 2014, MNRAS, 437, 3550

Mihalas, D., & Klein, R. I. 1982, JCoPh, 46, 97

Mihalas, D., & Weibel-Mihalas, B. 1984, Foundations of radiation hydrodynamics (New York: Oxford University Press)

Miller, J. S., & Goodrich, R. W. 1990, ApJ, 355, 456

Miyoshi, M., Moran, J., Herrnstein, J., et al. 1995, Natur, 373, 127

Moran, E. C., Barth, A. J., Kay, L. E., & Filippenko, A. V. 2000, ApJL, 540, L73

Namekata, D., & Umemura, M. 2016, MNRAS, 460, 980

Nenkova, M., Ivezić, Ž., & Elitzur, M. 2002, ApJL, 570, L9

Nenkova, M., Sirocky, M. M., Ivezić, Ž., & Elitzur, M. 2008a, ApJ, 685, 147

Nenkova, M., Sirocky, M. M., Nikutta, R., Ivezić, Ž., & Elitzur, M. 2008b, ApJ, 685, 160

Netzer, H. 1990, in Saas-Fee Advanced Courses, Active Galactic Nuclei, ed. T. J.-L. Courvoisier, & M. Mayor, Vol. 20 (Berlin: Springer), 57

Netzer, H. 1987, MNRAS, 225, 55

Neufeld, D. A., & Maloney, P. R. 1995, ApJL, 447, L17

Nicastro, F. 2000, ApJL, 530, L65

Oh, K., Yi, S. K., Schawinski, K., et al. 2015, ApJS, 219, 1

Ohsuga, K., & Umemura, M. 2001, A&A, 371, 890

Ohsuga, K., & Umemura, M. 1999, ApJL, 521, L13

Osterbrock, D. E., & Koski, A. T. 1976, MNRAS, 176, 61P

Packham, C., Radomski, J. T., Roche, P. F., et al. 2005, ApJL, 618, L17

Peterson, B. M., Ferrarese, L., Gilbert, K. M., et al. 2004, ApJ, 613, 682

Phinney, E. S. 1989, in NATO Advanced Science Institutes Series C: Mathematical and Physical Science, Theory of Accretion Disks, ed. F. Meyer, W. J. Duschl, J. Frank, & E. Meyer-Hofmeister, Vol. 290 (Dordrecht: Kluwer), 457

Pier, E. A., & Krolik, J. H. 1992a, ApJ, 401, 99

—. 1992b, ApJL, 399, L23

—. 1993, ApJ, 418, 673

Pogge, R. W. 1989, ApJ, 345, 730

Pogge, R. W., & De Robertis, M. M. 1993, ApJ, 404, 563

Poncelet, A., Perrin, G., & Sol, H. 2006, A&A, 450, 483

Pott, J.-U., Malkan, M. A., Elitzur, M., et al. 2010, ApJ, 715, 736

Pounds, K. A., Reeves, J. N., King, A. R., et al. 2003, MNRAS, 345, 705

Prieto, M. A., Mezcua, M., Fernández-Ontiveros, J. A., & Schartmann, M. 2014, MNRAS, 442, 2145

Proga, D., Stone, J. M., & Kallman, T. R. 2000, ApJ, 543, 686

Raban, D., Jaffe, W., Röttgering, H., Meisenheimer, K., & Tristram, K. R. W. 2009, MNRAS, 394, 1325

Radomski, J. T., Piña, R. K., Packham, C., Telesco, C. M., & Tadhunter, C. N. 2002, ApJ, 566, 675

Radomski, J. T., Piña, R. K., Packham, C., et al. 2003, ApJ, 587, 117

Ramos Almeida, C., Martínez González, M. J., Asensio Ramos, A., et al. 2016, MNRAS, 461, 1387

Rayleigh, L. 1883, Proceedings of the London Mathematical Society, 14, 170

Rees, M. J., Silk, J. I., Werner, M. W., & Wickramasinghe, N. C. 1969, Natur, 223, 788

Reunanen, J., Prieto, M. A., & Siebenmorgen, R. 2010, MNRAS, 402, 879

Reynolds, C. S. 1997, MNRAS, 286, 513

Ricci, C., Ueda, Y., Koss, M. J., et al. 2015, ApJL, 815, L13

Rieke, G. H., & Lebofsky, M. J. 1981, ApJ, 250, 87

Risaliti, G., Maiolino, R., & Salvati, M. 1999, ApJ, 522, 157

Roth, N., Kasen, D., Hopkins, P. F., & Quataert, E. 2012, ApJ, 759, 36

Sanders, D. B., Phinney, E. S., Neugebauer, G., Soifer, B. T., & Matthews, K. 1989, ApJ, 347, 29

Sanders, D. B., Soifer, B. T., Elias, J. H., et al. 1988, ApJ, 325, 74

Schartmann, M., Meisenheimer, K., Camenzind, M., et al. 2008, A&A, 482, 67

Schartmann, M., Meisenheimer, K., Klahr, H., et al. 2009, MNRAS, 393, 759

Schartmann, M., Wada, K., Prieto, M. A., Burkert, A., & Tristram, K. R. W. 2014, MNRAS, 445, 3878

Semenov, D., Henning, Th., Helling, Ch., Ilgner, M., & Sedlmayr, E. 2003, A&A, 410, 611

Shakura, N. I., & Sunyaev, R. A. 1973, A&A, 24, 337

Shappee, B. J., Prieto, J. L., Grupe, D., et al. 2014, ApJ, 788, 48

Shi, J., & Krolik, J. H. 2008, ApJ, 679, 1018

Shi, Y., Rieke, G. H., Smith, P., et al. 2010, ApJ, 714, 115

Skinner, M. A., & Ostriker, E. C. 2013, ApJS, 206, 21

Stalevski, M., Fritz, J., Baes, M., Nakos, T., & Popović, L. Č. 2012, MNRAS, 420, 2756

Stone, J. M., Gardiner, T. A., Teuben, P., Hawley, J. F., & Simon, J. B. 2008, ApJS, 178, 137

Swain, M., Vasisht, G., Akeson, R., et al. 2003, ApJL, 596, L163

Takeuchi, S., Ohsuga, K., & Mineshige, S. 2013, PASJ, 65, 88

—. 2014, PASJ, 66, 48

Taylor, G. 1950, RSPSA, 201, 192

Thompson, T. A., Quataert, E., & Murray, N. 2005, ApJ, 630, 167

Tielens, A. G. G. M., McKee, C. F., Seab, C. G., & Hollenbach, D. J. 1994, ApJ, 431, 321

Tombesi, F., Cappi, M., Reeves, J. N., et al. 2010, A&A, 521, 57

Tombesi, F., Cappi, M., Reeves, J. N., et al. 2013, MNRAS, 430, 1102

Toro, E. F. 2009, Riemann Solvers and Numerical Methods for Fluid Dynamics: A Practical Introduction (3rd ed.; Dordrecht: Springer), DOI: 10.1007/b79761

Tran, H. D. 2001, ApJL, 554, L19

Treister, E., Krolik, J. H., & Dullemond, C. 2008, ApJ, 679, 140

Tresch-Fienberg, R., Fazio, G. G., Gezari, D. Y., et al. 1987, ApJ, 312, 542

Tristram, K. R. W., Burtscher, L., Jaffe, W., et al. 2014, A&A, 563, 82

Tristram, K. R. W., Meisenheimer, K., Jaffe, W., et al. 2007, A&A, 474, 837

Tristram, K. R. W., Raban, D., Meisenheimer, K., et al. 2009, A&A, 502, 67

Tristram, K. R. W., Schartmann, M., Burtscher, L., et al. 2012, JPhCS, 372, 12035

Trump, J. R., Impey, C. D., Kelly, B. C., et al. 2011, ApJ, 733, 60

Trump, J. R., Sun, M., Zeimann, G. R., et al. 2015, ApJ, 811, 26

Ueda, Y., Akiyama, M., Ohta, K., & Miyaji, T. 2003, ApJ, 598, 886

Ulvestad, J. S., & Wilson, A. S. 1984, ApJ, 285, 439

Urry, C. M., & Padovani, P. 1995, PASP, 107, 803

Véron-Cetty, M.-P., & Véron, P. 2010, A&A, 518, 10

Wada, K. 2012, ApJ, 758, 66

—. 2015, ApJ, 812, 82

Wada, K., & Norman, C. A. 2002, ApJL, 566, L21

Wada, K., Schartmann, M., & Meijerink, R. 2016, arXiv: 1608.06995

Weymann, R. J., Morris, S. L., Foltz, C. B., & Hewett, P. C. 1991, ApJ, 373, 23

Wilson, A. S. 1996, VA, 40, 63

Wittkowski, M., Kervella, P., Arsenault, R., et al. 2004, A&A, 418, L39

Woo, J.-H., & Urry, C. M. 2002, ApJ, 579, 530

Zakamska, N. L., & Greene, J. E. 2014, MNRAS, 442, 784

Zakamska, N. L., Hamann, F., Pâris, I., et al. 2016, MNRAS, 459, 3144

Zakamska, N. L., Schmidt, G. D., Smith, P. S., et al. 2005, AJ, 129, 1212

Zakamska, N. L., Strauss, M. A., Krolik, J. H., et al. 2006, AJ, 132, 1496

Zamorani, G., Henry, J. P., Maccacaro, T., et al. 1981, ApJ, 245, 357

Zhang, S. N., Ji, L., Marshall, H. L., et al. 2011, MNRAS, 410, 2274

Curriculum Vitæ

Chi-Ho Chan was born on August 18, 1987 in Hong Kong to working-class parents. He received his primary education at Kwai Ming Wu Memorial School of the Precious Blood and La Salle Primary School; after that, he attended secondary school at La Salle College. With his distinguished results in the Hong Kong Certification of Education Examination, he was admitted to the Chinese University of Hong Kong under the Early Admission Scheme to pursue a course of study in theoretical physics with minors in the German language and in business administration. He was nominated to the Dean's Honours List of the Faculty of Science for two consecutive years, and he obtained his Bachelor of Science with Honours (second class, upper division) in 2009. Shortly after, he began his graduate studies in astrophysics at the Johns Hopkins University under the instruction of Professor Julian H. Krolik. He was awarded the Eun-Jung Rhee Teaching Award for his contribution toward the course Special Relativity and Waves.

Chan is a computational astrophysicist by profession, with expertise in radiative magnetohydrodynamics simulations and active galactic nuclei. He is also interested in computer science, programming, mathematics, languages, and typography.